

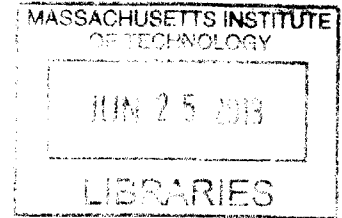
# Physico-Chemical Hydrodynamics of Droplets on Textured Surfaces with Engineered Micro/Nanostructures

by

Kyoo Chul Park

B.S., Mechanical and Aerospace Engineering  
Seoul National University, 2008  
M.S., Mechanical Engineering  
Massachusetts Institute of Technology, 2010

**ARCHIVES**



Submitted to the Department of Mechanical Engineering  
in partial fulfillment of the requirements for the degree of  
Doctor of Philosophy in Mechanical Engineering


at the

MASSACHUSETTS INSTITUTE OF TECHNOLOGY

June 2013

© Massachusetts Institute of Technology, 2013. All rights reserved.

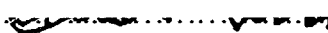
Signature of Author.....

  
Kyoo Chul Park  
Department of Mechanical Engineering  
May 21, 2013

Certified by.....

  
Gareth H. McKinley  
Professor, Mechanical Engineering  
Thesis Supervisor

Accepted by.....

  
David E. Hardt  
Professor, Mechanical Engineering  
Chairman, Department Committee on Graduate Students



# **Physico-Chemical Hydrodynamics of Droplets on Textured Surfaces with Engineered Micro/Nanostructures**

by

Kyoo Chul Park

Submitted to the Department of Mechanical Engineering on May 21, 2013  
in partial fulfillment of the requirements for the degree of  
Doctor of Philosophy in Mechanical Engineering

## **ABSTRACT**

Understanding physico-chemical hydrodynamics of droplets on textured surfaces is of fundamental and practical significance for designing a diverse range of engineered surfaces such as low-reflective, self-cleaning or anti-fogging glass, easy-cleaning robust inkjet printer heads, or efficient fog-harvesting surfaces. Developing such functional surfaces requires interdisciplinary considerations that have not been broadly explored and which integrate principles from capillarity, optics, nanofabrication, hydrodynamics of complex fluids, and even aerodynamics. The primary contribution of this thesis is to integrate consideration of wetting phenomena coupled with reflection of light, mechanical failure of slender structures, energy dissipation in non-Newtonian fluids, and aerodynamics of airborne droplets impacting onto permeable structures. Based on this integrative understanding, we construct design frameworks for both quantifying the performance of the desired functionalities for each application and for developing optimal functional surfaces.

The first part of this thesis is focused on the development of superhydrophobic and superphotophilic surfaces that can be used for improving light-harvesting efficiency of photovoltaic cells. A design framework that combines wetting phenomena and adiabatic refractive index-matching together with a novel nanofabrication method is introduced to select slender tapered nanostructures that fulfill the multiple functionalities. The resulting nanocone-textured glass substrate exhibits highly robust superhydrophobicity and omnidirectional broadband anti-reflectivity as well as self-cleaning or anti-fogging property when conformally coated with a suitable chemical layer.

Extending the nonwettability of textured surfaces to low surface tension oils is more difficult because oleophobic surfaces require a re-entrant topography. Deep reactive ion etching is used to fabricate square arrays of silicon nanopillars with wavy sidewalls that help support the superoleophobic state. The effect of the re-entrant nanotexture on the apparent contact angle, contact angle hysteresis, and sliding angle of water and hexadecane droplets is studied. We discuss numerical predictions for the critical pressure differences that cause failure of the Cassie-Baxter state that characterizes the super-repellent state for water and hexadecane droplets on the textured surfaces. In addition, dimensionless design parameters for quantifying the resistance to bending or buckling of the slender nanostructures are derived to design robust superoleophobic inkjet printer heads.

Because of the natural repellency of many leaf surfaces to water, non-Newtonian fluids such as dilute polymer solutions are widely used to maximize the deposition rate of aqueous droplets sprayed onto textured liquid-repellent target surfaces. The drop impact dynamics of complex liquids on such surfaces is studied to develop a systematic understanding of the coupled effects of fluid viscoelasticity and the resulting dynamic wetting characteristics. We use hydrophobically-coated flat glass substrates, microtextured pillar surfaces, and nanocone surfaces as well as natural lotus leaves in conjunction with impacting droplets of dilute polyethylene oxide solutions to construct a drop impact dynamics diagram that can be used for understanding deposition of complex fluids on a wide range of hydrophobic textured surfaces.

Lastly, the fundamental principles underlying the collection of fog droplets impacting permeable and textured structures such as woven meshes are studied. A design map predicting the theoretical collection efficiency is constructed based on two important dimensionless ratios that characterize the mesh geometry and the impacting droplet stream. Two physical limitations associated with clogging and re-entrainment are identified and potential solutions utilizing surface wettability are discussed. We use a family of physico-chemically patterned meshes with a directed stream of fog droplets to simulate a natural foggy environment and demonstrate a five-fold enhancement in the fog-collecting efficiency of a conventional polyolefin mesh. The design rules developed in this thesis can be applied to select a mesh surface with optimal topography and wetting characteristics to harvest enhanced water fluxes over a wide range of natural convected fog environments.

In summary, by developing an integrative understanding of the physico-chemical hydrodynamics of droplets on textured substrates, we have been able to realize a number of novel functionalities using textured surfaces and have constructed design frameworks that can be applied for optimizing the performance of each multi-functional surface. For future work, initial steps for commercializing several of these multi-functional surfaces developed in this thesis are briefly discussed.

Thesis Supervisor: Gareth H. McKinley  
Title: Professor of Mechanical Engineering

## ACKNOWLEDGEMENTS

I would like to thank my thesis advisor Professor Gareth H. McKinley. I have enjoyed exploring numerous exciting research topics thanks to his intellectual interests and open mind, as well as generous patience and strong leadership. I have learned many important things to become a professional researcher, including how to catch essential points of interesting ideas, how to define and construct research problems, how to design simple experiments to exam hypotheses, how to organize storylines, and how to write or present effectively. I would also like to greatly thank Professor Robert E. Cohen for his enthusiastic encouragement and critical advice about my thesis. Both professors have been good academic parents for me.

I also thank Professor Cullen R. Buie and Professor George Barbastathis. Professor Buie has given me helpful and essential comments on my thesis as a thesis committee member. He has also led me with his great leadership when I was a teaching assistant for advanced fluid mechanics. I feel grateful to Professor Barbastathis for his excellent optics lecture that led me to the productive collaboration with him, as well as for helpful advice and warm encouragement.

I gratefully mention my supervisors during my summer internship period and other professors at MIT. Dr. Kock-Yee Law and Dr. Hong Zhao were very good supervisors to me and provided a valuable opportunity to experience practical research in industry. I enjoyed exciting teamwork at the Xerox research center including some nanofabrication at Cornell University. Professor Daniel Blankschtein was an excellent instructor who led me to the fundamental science of surfactants and interfacial phenomena. Thanks to his three organized and clear lectures at MIT, I could expand my research experience. I also appreciate Professor Michael F. Rubner for allowing me to use his laboratory equipment and for giving a number of critical comments at the group meetings.

I would also like to thank my collaborators and friends at MIT. In particular, I thank Hyungrul J. Choi for his excellent contribution and hard work in our collaboration. I have been happy because we could have many honorable moments together as results of this productive collaboration. Professor Wonjae Choi, Professor Vivek Sharma, Hyomin Lee, and Yong-Cheol Shin, without your leading and supporting me mentally, I would not be able to get through my graduate student life. I appreciate your useful suggestions about various research problems as well as daily life topics. I also thank Dr. Shreerang S. Chhatre, Dr. Adam J. Meuler, Siddarth Srinivasan, Justin Kleingartner, Dr. Christopher Dimitriou, Thomas Ober, Ahmed Helal, Bavand Keshavarz, Aditya Jaishankar, Professor Chih-Hao Chang, and Jeong-Gil Kim for your helpful discussions. I gratefully acknowledge the support of other collaborators and friends in the research groups in MIT, Xerox research center and Chile.

Lastly, I would like to give my great thanks and love to my wife and daughter. Jinyoung Park has been a very nice partner in my journey toward PhD degree. Evelyn Nayeon Park has been the source of my energy by showing me her lovely smiles. I also thank firm supports from my parents and brother in South Korea.

This thesis was financially supported in part by Samsung Scholarship and Xerox-MIT fellowship as well as was also partially funded by the MIT MISTI-Chile program and the Xerox Foundation through Xerox University Affairs Committee (UAC) grant.

# TABLE OF CONTENTS

<b>1. Introduction.....</b>	<b>23</b>
1.1 Introductory Remarks.....	24
1.2 Interfacial Tension of Materials and Equilibrium Contact Angle.....	26
1.3 Effect of Surface Texture on Wetting Phenomena .....	28
1.4 Re-entrant Structure for Superoleophobicity and Transition from Metastable Cassie-Baxter State to Wenzel State.....	32
1.5 Mechanical Durability of Textured Surfaces.....	35
1.6 Reflection at Optical Interfaces.....	36
1.7 Thesis Objectives and Outline .....	38
References.....	43
<b>2. Design of Silica Nanocone Structures for Transparent Superhydrophobic and Supertransmissive Surfaces .....</b>	<b>47</b>
2.1 Introduction and Theory.....	48
2.1.1 Analysis of Natural and Artificial Textured Surfaces.....	48
2.1.2 Analysis of Cone Structure as a Self-stabilizing Topography and Optical Bandpass Filter.....	52
2.1.3 Critical stresses leading to fracture by bending or buckling of slender nanotexture. ....	55
2.2 Experimental Methods.....	61
2.2.1 Fabrication of Tapered Nanocone Surfaces .....	61
2.2.2 Vapor-phase Low Surface Energy Coating.....	64
2.2.3 Contact Angle Measurements .....	64
2.2.4 Optical Transmission Measurements .....	65
2.3 Results and Discussion .....	65
2.3.1 Superhydrophobicity/superhydrophilicity of Nanocone Structure.....	65
2.3.2 Broadband Omnidirectional Transmission and Solar Irradiance .....	69
2.3.3 Self-cleaning and Anti-fogging Effect .....	73
2.4 Conclusion .....	75
Appendix A Dimensionless measure of robustness $T^*(z/H)$ of the Cassie-Baxter state against an applied pressure difference across the water-air interfaces. ....	76
Appendix B A computational model to calculate the meniscus location of water-air interfaces contacting the nanotaper structures under various imposed pressure differences.....	80

Appendix C Dimensionless measure of optical transmission bandwidth for the characterization of antireflective tapered nanocone surfaces. ....	82
Appendix D Measurements of broadband and omnidirectional optical transmission of the double-sided nanotaper surfaces. ....	87
References.....	90
<b>3. Effect of Surface Texturing on Superoleophobicity, Contact Angle Hysteresis, and “Robustness” .....</b>	<b>95</b>
<b>3.1 Introduction and Theory.....</b>	<b>96</b>
3.1.1 General Introduction.....	96
3.1.2 Surface Evolver Simulation of the Three-phase Contact Line on the Superoleophobic Pillar Surface.....	98
3.1.3 Critical Bending and Buckling Loads of Cylindrical Pillar Structures.....	100
<b>3.2 Experimental Methods .....</b>	<b>102</b>
3.2.1 Materials and Surface Texture Fabrication .....	102
3.2.2 Surface Modification.....	103
3.2.3 Measurements.....	103
3.2.4 Modeling of Surface Wettability .....	103
<b>3.3 Results and Discussion .....</b>	<b>104</b>
3.3.1 Effect of Pillar Spacing on Surface Properties.....	104
3.3.2 Effect of Pillar Diameter .....	111
3.3.3 Effect of Pillar Height .....	113
3.3.4 Effect of Pillar Overhang Thickness.....	114
3.3.5 Surface Robustness.....	117
<b>3.4 Conclusion .....</b>	<b>121</b>
Appendix A Effect of Pillar Height on the Surface Properties.....	124
Appendix B Static Contact Angle Data for Pillar Array FOTS Surfaces with Varying Overhang Thickness .....	125
References.....	126
<b>4. Drop Impact Dynamics of Dilute Polymer Solutions on Textured Hydrophobic Surfaces.....</b>	<b>129</b>
<b>4.1 Introduction and Theory.....</b>	<b>130</b>
4.1.1 Deposition of Impacting Droplets and Dilute Polymer Aqueous Solutions .....	130
4.1.2 Drop Impact Dynamics of Water on Superhydrophobic Surfaces.....	131



4.1.3 Shear and Extensional Rheology of Dilute PEO Solutions.....	133
4.1.4 Drop Impact of Dilute Polymer Solutions on Smooth Hydrophobic Surfaces .....	135
<b>4.2 Experimental Methods .....</b>	<b>137</b>
4.2.1 Preparation of Hydrophobic Surfaces .....	137
4.2.2 Preparation of Dilute PEO Solutions.....	138
4.2.3 Characterization of Wetting Properties of Textured Surfaces.....	139
4.2.4 Characterization of Viscoelasticity of PEO Solutions .....	139
4.2.5 Visual Analysis of Drop Impact Dynamics.....	140
<b>4.3 Results and Discussion .....</b>	<b>140</b>
4.3.1 Effect of Textural Length Scale and Solid Area Fraction on Drop Impact Dynamics .....	140
4.3.2 Maximum Droplet Diameter in the Expansion Stage .....	142
4.3.3 Stress Growth by Stretch and Relaxation of Polymer Coils .....	144
4.3.4 Drop Impact Dynamics Diagram .....	147
<b>4.4 Conclusion .....</b>	<b>149</b>
<b>References.....</b>	<b>150</b>
<b>5. Fog Harvesting Mesh Surfaces .....</b>	<b>153</b>
<b>5.1 Introduction and Theory.....</b>	<b>154</b>
5.1.1 Fog as a promising water source in arid and mountainous regions.....	154
5.1.2 Aerodynamic Efficiency and Deposition Efficiency.....	156
<b>5.2 Materials and Methods.....</b>	<b>160</b>
5.2.1 Preparation of Mesh Surfaces.....	160
5.2.2 Coating Materials .....	160
5.2.3 Experimental Setup in a Humidity Control Chamber .....	162
<b>5.3 Results and Discussion .....</b>	<b>163</b>
5.3.1 Two Major Practical Problems of Fog-collection .....	163
5.3.2 Role of Surface Wettability.....	166
5.3.3 Combined Design Space and its Application as a Design Chart.....	169
<b>5.4 Conclusion .....</b>	<b>173</b>
<b>Appendix A Derivation of critical droplet radii <math>r_e</math> and <math>r_c</math> .....</b>	<b>174</b>
<b>Appendix B Time evolution of the performance of liquid-impregnated textured surfaces and schematic diagram of experimental setup for fog collection efficiency measurement .....</b>	<b>178</b>
<b>Appendix C Comparison of theoretical fog collection efficiencies for mesh surfaces.....</b>	<b>180</b>
<b>References.....</b>	<b>182</b>

**6. Thesis Summary and Future Work ..... 185**

**6.1 Thesis Summary..... 186**

**6.2 Future Work..... 189**

6.2.1 Inverted Nanocone Structure for Enhanced Mechanical Durability and Low Cost Fabrication of Multi-functional surfaces ..... 189

6.2.2 Initial Steps for Commercializing Fog Harvesting Surfaces in Chile ..... 191

6.2.3 Dactylovorous Surfaces ..... 192

**References..... 196**

## LIST OF FIGURES

**Figure 1-1** A schematic of the topographic complexity of various natural and artificial textured surfaces as a function of the dimensionless length scale  $L/\ell_{cap}$ , where  $\ell_{cap}$  is the capillary length ( $\ell_{cap} = (\gamma/\rho g)^{1/2}$ , where  $\gamma$  is the water-air interfacial tension,  $\rho$  is the density of water, and  $g$  is the standard gravity). The surfaces are: (a) gecko foot,<sup>45</sup> (b) wavy wall structure,<sup>41</sup> (c) microhoodoo,<sup>17</sup> (d) woven mesh with corpuscular nanotexture,<sup>46</sup> (e) nanocone,<sup>31</sup> (f) cicada wing,<sup>47</sup> (g) lotus leaf,<sup>48</sup> (h) spider web (Image courtesy William Lee), (i) *Calathea Zebrina* leaf,<sup>49</sup> (j) carbon nanotube,<sup>32</sup> (k) silicon nanostructure,<sup>7</sup> (l) micropillar, (m) slender leaves of trees (Image courtesy Robert Holmes). In particular, the nanocone, wavy wall structures, micropillars, and woven meshes are intensively investigated in this thesis..... 25

**Figure 1-2** Schematic sketch of side view of droplet (blue) on a chemically homogeneous flat surface (red), surrounded by vapor (or air)..... 26

**Figure 1-3** Water contact angles on different surface coatings. (a) Superwetting ( $\theta_E < 10^\circ$ ). (b) Hydrophilic ( $\theta_E < 90^\circ$ ). (c) Hydrophobic ( $90^\circ < \theta_E < 150^\circ$ ). (d) Superwater-repellent ( $\theta_E > 150^\circ$ )..... 27

**Figure 1-4** Schematic sketches of side view of (a) the fully-wetted Wenzel state and (b) the composite Cassie-Baxter state, with the comparison between the local equilibrium contact angle ( $\theta_E$ ) and the apparent contact angle on textured surfaces ( $\theta^*$ ).<sup>21, 23</sup> ..... 28

**Figure 1-5** (a-c) Advancing and receding contact angles and their locations in the schematic of free energy – apparent contact angle relation. (d) Advancing (hollow) and receding (solid) contact angles of water on rough wax surfaces, plotted versus the surface roughness.<sup>21</sup> ..... 30

**Figure 1-6** A schematic illustration of the various characteristic geometrical parameters used in the Cassie-Baxter relation (Eq. 1-4)..... 31

**Figure 1-7** (a) Water and (b) octane droplets on lotus leaf and schematic sketch (cross-sectional view) wetting of the two liquids on typical rough structures with a characteristic angle  $\psi$ .<sup>23</sup> ..... 32

**Figure 1-8** Re-entrant structures. (a) Schematic sketches of hoodoo structure and characteristic texture angle  $\psi$  at three different points. (b) Fabricated microhoodoo structure.<sup>17</sup> (c) Superoleophobicity of a microhoodoo surface (for octane,  $\gamma_{LV} = 21.6$  mN/m ).<sup>17</sup> ..... 33

**Figure 1-9** Two wetting transition modes. (a) Touch down transition when the apex of the meniscus touches the substrate. (b) Depinning transition when the angle the meniscus makes with the texture reaches the advancing contact angle.<sup>29</sup> ..... 34

**Figure 1-10** Two modes of distortion of slender beam that lead to the fracture. (a) Bending by shear load. (b) Buckling by normal load.<sup>42</sup> ..... 36

**Figure 1-11** Schematics of refracted and reflected waves (s-polarized or transverse electric (TE) light and p-polarized or transverse magnetic (TM) light) at an interface between air and glass plate (a) when an incident angle ( $\theta_i$ ) is smaller than Brewster's angle ( $\theta_B$ )<sup>43</sup> and (b) when an incident angle is equal to Brewster's angle ( $\theta_i = \theta_B$ ) (Copyright, Center for Occupational Research and Development). The oscillation of electric dipoles in the incident plane influences the reflected waves.<sup>43</sup> ..... 37

**Figure 1-12** Region of each thesis chapter in the dimensionless physico-chemical properties space composed of two important dimensionless numbers. Weber number ( $We = \rho U^2 D / \gamma$ ) characterizes inertial effect relative to capillary effect, where  $\rho$  is the density of liquid,  $U$  is the velocity of droplet,  $D$  is the diameter of droplet, and  $\gamma$  is the liquid-air interfacial tension. Deborah number ( $De = \lambda / t_R$ ) characterizes viscoelasticity, where  $\lambda$  is the relaxation time and  $t_R$  is the Rayleigh time. .... 38

**Figure 2-1** Plot of the number density ( $\eta$ ) of nanoscale features as a function of the aspect ratio ( $H/P$ ) for natural and artificial textured surfaces. The surfaces are: a) mosquito eye, b) cicada wing, c) silicon nanostructure, d) carbon nanotube, e) perfluoropolyether nanopillar (diameter at the base of pillars = 500 nm), f) nanonail, g) *Calathea Zebrina* leaf, h) lotus leaf, and i) microconical structure. Reprinted with permission from ref 23 (a, Copyright 2007 Wiley-VCH), ref 18 (b, Copyright 2008 IOP Publishing Ltd), ref 31 (c, Copyright 2007 Nature Publishing Group), ref 12 (d, Copyright 2003 ACS), ref 13 (f, Copyright 2008 ACS), ref 27 (g, Copyright 2009 Elsevier), ref 1 (h, Copyright Springer-Verlag 1997), and ref 49 (i, Copyright 2008 Wiley-VCH). To maximize transmission by minimizing reflection, a number density greater than the horizontal borderline (for circumventing interference effects of light) and an aspect ratio close to the vertical borderline (associated with the fracture by bending or buckling of high aspect ratio nanostructure (see 2.1.3)) are required. .... 49

**Figure 2-2** Design and development of optimal nanostructured multi-functional surfaces. (A) Schematic drawings of the three phase contact line on hydrophobically-modified and hydrophilic (as fabricated) nanotaper structures. The insets show corresponding goniometer images for  $5 \mu\ell$  droplets with apparent contact angles of  $\theta^* \approx 165^\circ$  and  $\theta^* \leq 5^\circ$  respectively. (B) Micrograph of the final developed nanotaper structure with numerical rendering of a cubic paraboloid. All scale bars represent 200 nm. (C) Blue-dyed water droplets sitting on a transparent nanotaper surface and on flat glass, each placed on top of printed black letters. The insets are top views of the same two surfaces. The very weak reflection and high contact angle of the tapered nanocone surface are in contrast to the intense reflection and low contact angle of water on flat glass..... 50

**Figure 2-3** (A) A schematic diagram (cross-sectional view) of the slender nanotaper structure. The light red shape represents approximation of the structure as a cubic paraboloid, whereas the black solid lines represent the sidewall of the truncated cone used for the analysis. (B) Lateral ( $F_l$ ) and axial forces ( $F_a$ ) acting on the tip of the nanotexture..... 56

**Figure 2-4** Stages of the fabrication process. (A) Deposition of multiple coating layers. (B) Development of photoresist pattern. (C-F) Subsequent etching steps of antireflective coating layer (C), cured HSQ layer (D), polysilicon layer (E), and fused silica wafer (F). All the white scale bars on the micrographs represent 200 nm. .... 63

**Figure 2-5** Extreme wetting properties of the nanocone structure. (A) Wetting diagram with experimental results obtained using droplets of water-ethanol mixtures with various compositions sitting on silane-treated flat ( $\theta_{adv}$ ) and tapered nanocone ( $\theta_{adv}^*$ ) surfaces. The inset represents a pure water droplet sitting on the silanized nanotaper surface (bottom left). (B) Environmental scanning electron microscope images of condensing water drops on the silanized nanocone surface showing spherical droplets resting on the tips of the nanotaper surface. (C) Calculation of the pressure difference  $\Delta P(z/H)$  that the water-air interface can resist at given penetration depths into the structure, based on the simple analytic scaling of the dimensionless robustness parameter ( $T^*$ , Eq. 2-1) (D) Sequential images of a water droplet impact on an oblique ( $30^\circ$  from the horizontal plane) nanotaper surface (taken through the use of a high speed camera;  $V_{imp} = 6.26$  m/s and  $We = 1785$ ). The last image on the bottom right side shows that no residual droplets remain on the nanotaper surface due to the

high robustness of the Cassie-Baxter state to the high dynamic pressure of the impacting drop. .... 66

**Figure 2-6** Enhanced broadband, omnidirectional optical transmission of the nanotaper structure. (A and B) Optical transmission for both transverse electric (TE) and transverse magnetic (TM) polarized light through the single and double-sided nanotaper surfaces (represented in red circle and blue triangle, respectively) is measured by changing the incident angle of a laser source. The theoretical model results calculated by using rigorous coupled wave analysis are also shown in solid lines (flat fused silica surface in black, single-sided nanotaper surface in red, and double-sided nanotaper surface in blue) for comparison. (C and D) Measured broadband transmission for TE-polarized and TM-polarized lights at the four different incident angles with a wide range of wavelength..... 71

**Figure 2-7** Averaged broadband transmission with two measurements on both TE and TM polarizations in Figure 2-6 C and D at the four different incident angles with a range of wavelength ( $300 \text{ nm} \leq \lambda \leq 1300 \text{ nm}$ ). The black line is the measured broadband transmission of the flat fused silica surface at normal incident angle. Spectral solar irradiation data (light blue) with respect to the same wavelength is shown in the inset for reference, and the dashed black line depicts the band gap of crystalline silicon, one of materials used for solar cells, which means that no light can be absorbed in photovoltaic devices for wavelengths greater than this value. .... 72

**Figure 2-8** Optical transmission measurements for quantifying the self-cleaning and anti-fogging properties of the nanocone surfaces. (A and B) Evolution of the transmission of 632.8 nm red laser through surface-contaminated tapered nanocone surface and flat glass surfaces, respectively. The transmission measurements were recorded while water droplets were released from a height of 10 mm (corresponding to impact velocity  $V = 0.44 \text{ m/s}$ ;  $We = 6.9$ ) from the inclined surfaces ( $30^\circ$ ) every five seconds. The apparent contact angles ( $\theta^* > 160^\circ$ ) as well as contact angle hysteresis ( $CAH < 3^\circ$ ) of our superhydrophobic nanotextured surface remained unaltered after more than 100 realizations of the self-cleaning tests that were carried out over a period of greater than 6 months.<sup>41</sup> (C) Image of printed letters viewed through fogged (nanocone (left) and flat glass (right) surfaces. (D) Change of transmission due to fogging and defogging on double-sided nanotaper (blue), single-sided nanotaper (red) and flat cleaned glass (black) surfaces. .... 74

<b>Figure 2-9</b> (A) SEM micrograph of slender tapered nanocone structure. (B) A schematic diagram of horizontally cross-sectioned nanotaper structure. ....	77
<b>Figure 2-10</b> (A-C) Side view, oblique view, and top view of the calculated equilibrium shape of the water-air interface with four neighboring nanotaper structures. Solid-liquid, solid-air, and liquid-air interfaces are represented by light purple, light red, and light blue colors, respectively. (D) A magnified side view of diagonal cross-section (A-A in C) shows the severely distorted shape of three phase contact line and the liquid-air interface.....	81
<b>Figure 2-11</b> Diagram of the structure geometry and incident light configuration. ....	82
<b>Figure 2-12</b> Normalized maximum and minimum operating wavelengths plotted against incident angle.....	84
<b>Figure 2-13</b> The normalized operating bandwidth ( $B^*$ ) vs. structure aspect ratio for different incident angles. For the structure to function at large angles, high aspect ratio structures are required. ....	85
<b>Figure 2-14</b> Reflection of antireflection nanostructure simulated using RCWA for a number of incident angles as functions of normalized structure height.....	86
<b>Figure 2-15</b> Transmission efficiency of the antireflective nanocone structure simulated using RCWA for a number of incident angles as functions of the wavelength of the incident illumination.....	86
<b>Figure 2-16</b> Measured optical transmission of the nanotaper structures and simulated transmission using RCWA for both transverse electric (TE) and transverse magnetic (TM) polarized lights as a function of the wavelength at 30° incident angle.....	88
<b>Figure 2-17</b> Measured optical transmission of the nanotaper structures and simulated transmission using RCWA for both TE and TM-polarized lights as a function of the wavelength at 45° incident angle.....	89
<b>Figure 2-18</b> Measured optical transmission of the nanotaper structures and simulated transmission using RCWA for both TE and TM-polarized lights as a function of the wavelength at 60° incident angle. ....	89
<b>Figure 3-1</b> SEM micrographs of ~3 $\mu\text{m}$ diameter pillar array surfaces coated with fluorooctyl trichlorosilane (FOTS) layer, with (a) 4.5 $\mu\text{m}$ , (b) 6 $\mu\text{m}$ , (c) 9 $\mu\text{m}$ , and (d) 12 $\mu\text{m}$ center-to-center spacing. (Insets: sessile drops of water and hexadecane on the pillar array surfaces)97	

<b>Figure 3-2</b> Equilibrium shapes of sagging liquid-air interface of hexadecane on the superoleophobic pillar array FOTS surface (blue: hexadecane, red: pillar) .....	99
<b>Figure 3-3</b> (a) $H^*$ failure (“touch-down” scenario) under pressure; and (b) $T^*$ failure (“depinning” scenario) under pressure. (blue: hexadecane, red: pillar) .....	99
<b>Figure 3-4</b> (a) Model textured surface used to model the deformation of the pillar array surface against external force $F_{\text{global}}$ ; (b) bending failure of a single pillar; and (c) buckling failure of a single pillar.....	100
<b>Figure 3-5</b> Plot of dynamic water contact angle data versus solid area fraction for 3 $\mu\text{m}$ pillar array FOTS surfaces ( $\blacklozenge$ , $\blacksquare$ and $\blacktriangle$ ). (Insert: dynamic water contact angle data from a 1 $\mu\text{m}$ pillar array (X) and a 5 $\mu\text{m}$ pillar array (O) FOTS surface) .....	105
<b>Figure 3-6</b> Plot of dynamic hexadecane contact angle data versus solid area fraction for 3 $\mu\text{m}$ pillar array FOTS surfaces ( $\blacklozenge$ , $\blacksquare$ and $\blacktriangle$ ). (Insert: dynamic hexadecane contact angle data from a 1 $\mu\text{m}$ pillar array (X) and a 5 $\mu\text{m}$ pillar array (O) FOTS surface) .....	107
<b>Figure 3-7</b> Plot of sliding angle versus solid area fraction for water and hexadecane on 3 $\mu\text{m}$ ( $\triangle$ , $\blacktriangle$ ), 1 $\mu\text{m}$ ( $\diamond$ , $\blacklozenge$ ); and 5 $\mu\text{m}$ ( $\circ$ , $\bullet$ ) pillar array FOTS surfaces (water: open symbols, hexadecane: solid symbols). .....	108
<b>Figure 3-8</b> Ideal and actual Cassie-Baxter state.....	109
<b>Figure 3-9</b> Surface Evolver modeling of the water/FOTS pillar array interface as a function of the thickness of the overhang structure (red: pillar, blue: water) .....	110
<b>Figure 3-10</b> Surface Evolver modeling of the hexadecane/FOTS pillar array interface as a function of the thickness of the overhang structure (red: pillar, blue: hexadecane).....	110
<b>Figure 3-11</b> SEM micrographs and water & hexadecane sessile drop data for (a) $\sim 5 \mu\text{m}$ (15 $\mu\text{m}$ pitch) and (b) $\sim 1 \mu\text{m}$ (3 $\mu\text{m}$ pitch) pillar array surfaces .....	111
<b>Figure 3-12</b> SEM micrographs and sessile drop data for straight wall pillar arrays with overhang thickness varying from 95 nm to 520 nm to 1030 nm.....	115
<b>Figure 3-13</b> Plots of (a) advancing and receding contact angle and (b) sliding angle as a function of the thickness of the overhang for straight wall pillar array FOTS surfaces with different overhang thickness.....	116
<b>Figure 3-14</b> Surface Evolver simulation: wetting of a pillar array FOTS surface with an overhang re-entrant structure by hexadecane .....	118



**Figure 3-15** Plot of breakthrough pressure as a function of (a) spacing parameter  $D^*$  and (b) static contact angle for pillar array surfaces with different pillar diameters at  $D^* = 4$ . ..... 119

**Figure 3-16** (top) SEM micrographs of 3  $\mu\text{m}$  pillar array surfaces with different height and (bottom) plots of static and dynamic contact angles of the 3  $\mu\text{m}$  pillar array surfaces as a function of pillar height. .... 124

**Figure 3-17** Plots of static contact angle as a function of thickness of the overhang for straight wall pillar array FOTS surfaces with different overhang thickness. .... 125

**Figure 4-1** Drop dynamics of water and PEO solution ( $M_W = 4 \times 10^6$  Daltons,  $c = 200$  ppm,  $De = 1.52$ ,  $D_0 = 2.29$  mm), impacting on two different textured hydrophobic surfaces. (a) Water droplet ( $We = 14.1$ ) on the microtextured surface (MP,  $W = 30$   $\mu\text{m}$ ,  $P = 60$   $\mu\text{m}$ ,  $H = 40$   $\mu\text{m}$ ,  $f_s = 0.25$ ) (b) PEO droplet ( $We = 14.1$ ) on the MP surface. (c) PEO droplet ( $We = 14.1$ ) impacting a nanotextured surface (NC,  $W = 8$  nm,  $P = 200$  nm,  $H = 1.1$   $\mu\text{m}$ ,  $f_s = 0.01$ ). (d) PEO droplet with a higher impact velocity ( $We = 55.6$ ) on the NC surface. Time interval of 2 ms separates successive frames in each row..... 141

**Figure 4-2** (a). Time evolution of dimensionless drop diameter at the contact line and Weissenberg number ( $Wi$ , retraction stage only, shown in the inset) of impacting PEO solution ( $M_W = 4 \times 10^6$  Daltons,  $c = 200$  ppm,  $De = 1.52$ ,  $D_0 = 2.29$  mm), on three representative surfaces at  $We = 14.1$ . The retraction velocity and apparent  $Wi$  are highest for the nanotextured surface (NC), where complete rebound is observed. (b) Maximum spread factor (ratio of the maximum diameter to initial drop diameter before the impact) as a function of  $We^{1/4}$ . The silanized smooth (SS), micropost (MP) and nanocone (NC) are respectively shown as black circles, red squares and blue triangles, and for PEO 4.0M, three different concentrations are represented using different size symbols. .... 143

**Figure 4-3** Time evolution of normal stress difference ( $\Delta\tau$ ) of PEO solution ( $M_W = 4 \times 10^6$  Daltons,  $c = 200$  ppm,  $We = 14.1$ ) is shown for the three different surfaces. For the same time duration and extensional rate, the nanotextured surface (NC) displays higher retraction velocity and higher apparent extension rate than the microtextured surface (MP). And it shows a smaller normal stress difference, implying a lower energy dissipation level by polymer stretching due to extensional flow, which rationalize the observed complete rebound of PEO solution. Inset: The schematic drawing of stress growth and stress relaxation associated with stick-slip fluid motion over a textured surface. .... 145

**Figure 4-4** A drop impact dynamics diagram that shows bouncing and deposition. This diagram is constructed based on two essential dimensionless parameters: (1) elasticity ( $Wi$ ) and (2) surface characteristics (determined by details of the texture). Deposition, full rebound and partial rebound are shown using filled, open and half-filled symbols, respectively. The diagram includes a hydrophobic surface smooth silanized glass (SS) and three canonical examples of superhydrophobic textured surfaces: micropost (MP), nanocone (NC) and lotus leaf (see text for details)..... 148

**Figure 5-1** Natural and artificial examples of fog harvesting surfaces. (a) Slender leaves of trees (Image courtesy Robert Holmes). (b) A spider web decorated with droplets of water collected from fog (Image courtesy William Lee). (c) A large area man-made fog collector deployed in the Atacama Desert of Chile (4) and (d) triangular weave of the Raschel Mesh used in Large Fog Collector. (e) The basic mechanism of fog collection by physical impaction of droplets on the mesh, collection of larger coalesced droplets, and subsequent drainage..... 155

**Figure 5-2** Fog flow through a woven mesh surface, and a contour plot of the fog harvesting efficiency. (a) Illustration indicating the stream surfaces of fog laden wind and their divergence after passing through a woven mesh surface. (b) An enlarged picture focusing on the interaction between incoming fog droplets and a horizontal mesh element. Droplets that are closer to the central axis are trapped on the cylindrical wire, whereas droplets closer to the periphery follow the streamline around the wire. Droplets on the wire coalesce, and once they grow past a threshold size, they drain under gravity. (c) A contour plot of the fog harvesting efficiency ( $\eta$ ) as a function of the ratio of radius of the fog droplets to the radius of the wire ( $R^* = r_{fog}/R$ ) and the spacing ratio of the woven mesh ( $D^* = (R + D)/R$ ). The location of various mesh surfaces and corresponding predicted efficiencies are highlighted on the design chart. .... 157

**Figure 5-3** Two factors that reduce collection efficiency, and the surface modification design space that depicts the relative resistance to re-entrainment and drainage. Two factors that inhibit fog harvesting and reduce collection efficiency are (a) re-entrainment of collected droplets in the wind and (b) blockage of the mesh. (c) The plot identifies the range of droplet sizes where the forces of adhesion dominate the drag forces, and establishes a criterion for a threshold droplet size for re-entrainment. (d) A second constraint arises from

comparing the weight of the droplet with the surface pinning force arising from contact angle hysteresis. The threshold size where gravity dominates hysteretic pinning can be decreased by minimizing  $CAH = \cos\theta_{rec} - \cos\theta_{adv}$  ..... 164

**Figure 5-4** The design space constructed from two dimensionless parameters related to work of adhesion (abscissa) and contact angle hysteresis (ordinate) depicts the relative resistance to re-entrainment and drainage. Measured values for droplets of water ( $V = 10 \mu\text{L}$ ) deposited on several different coatings are shown in the plot. Wetting characteristics corresponding to a higher work of adhesion and lower contact angle hysteresis are ideal for the maximum fog collection efficiency..... 167

**Figure 5-5** Measured fog collection efficiency. The coordinates of various mesh surfaces tested in the laboratory are depicted on the design space in (a) and the measured fog-collecting efficiencies ( $N = 3$ ) are plotted in (b) and (c). At any point to the right of the critical lines shown for the polyolefin and POSS-PEMA coating in Figure 5-5a (*i.e.* any point in the shaded region with  $D < D_{crit}$ ), the mesh openings clog with liquid droplets and the fog harvesting efficiency deteriorates. (b) and (c) explore the role of the mesh coating and structure (*i.e.*, the individual fiber size  $R$  and the spacing  $D$ ). In (c) the theoretical efficiency is shown by a broken line. The measured fog collection efficiency increases monotonically as the radius of the wire mesh decreases from  $R = 445 \mu\text{m}$  (●) to  $R = 172 \mu\text{m}$  (▲), but decreases in the case of  $R = 127 \mu\text{m}$  (▶) as we enter the drainage-limited zone on the design chart. The time evolution of the fog harvesting performance of the optimal wire mesh (▲) and the Raschel mesh is compared over many hours in (d). The optimal wire mesh (▲) collects more water and reaches a steady state faster than the Raschel mesh (◇).  
..... 170

**Figure 5-6** Schematic diagram of water droplets on a cylindrical mesh filament (cross-sectional view) and on one grid element of a woven mesh (top view). Both droplets are assumed to be spherical caps with the algebraic average of contact angles  $\theta = (\theta_{adv} + \theta_{rec})/2$  ..... 174

**Figure 5-7** An image of the clogging droplets on a woven mesh. .... 176

**Figure 5-8** A micrograph of the POSS-PEMA spraycoated mesh.<sup>24</sup> ..... 177

**Figure 5-9** Evolution of the advancing (dark blue) and receding (light blue) contact angles of water droplets on the liquid-impregnated surfaces. The contact angles were measured every

three minutes while water droplets were released from a height of 10 mm (corresponding to impact velocity  $v = 0.44$  m/s;  $We \approx 6.7$ ) from the inclined surfaces ( $45^\circ$ ) with the flow rate of 3.3 ml/min (corresponding to 70 impacts per minute)..... 178

**Figure 5-10** Illustration and actual image of the experimental setup for fog collection efficiency measurement. .... 179

**Figure 5-11** Predicted fog harvesting efficiency  $\eta$  for a double layered Raschel mesh (blue) and for a woven mesh with  $R = 172 \mu\text{m}$ , and  $D^* = 3.5$  (red) are compared for six conditions of fog droplet size and wind velocity. Velocities ( $v_0$ ) in m/s and fog droplet radius ( $r_{\text{fog}}$ ) in  $\mu\text{m}$  are: (1)  $v_0 = 0.5$ ,  $r_{\text{fog}} = 3$ , (2)  $v_0 = 0.5$ ,  $r_{\text{fog}} = 6$ , (3)  $v_0 = 2$ ,  $r_{\text{fog}} = 3$ , (4)  $v_0 = 2$ ,  $r_{\text{fog}} = 6$ , (5)  $v_0 = 8$ ,  $r_{\text{fog}} = 3$ , and (6)  $v_0 = 8$ ,  $r_{\text{fog}} = 6$ , respectively..... 180

## LIST OF TABLES

<b>Table 2-1</b> Water Contact Angle Information (at $T = 25^{\circ}C$ ).....	76
<b>Table 2-2</b> The structure geometry for rigorous coupled wave analysis (RCWA). 20 discrete layers were used for defining nanotaper structures and the duty cycles of each layer are listed in the table. The period is 200 nm.....	87
<b>Table 3-1</b> Effect of the pillar spacing on the surface properties of 3 $\mu\text{m}$ pillar array FOTS surfaces. ....	105
<b>Table 3-2</b> Effect of the pillar size and pillar height on the surface properties of various pillar array FOTS surfaces. ....	112
<b>Table 4-1</b> List of physico-chemical properties of fluids and important dimensionless numbers associated with drop impact dynamics .....	132
<b>Table 4-2</b> Geometrical dimensions and wetting properties of different textured surfaces. ....	139
<b>Table 5-1</b> The values of the receding contact angle, contact angle hysteresis, and critical radii $r_c$ and $r_e$ for each surface coating, with the laboratory fog condition used in the humidity chamber experiment ( $v_0 \approx 2 \text{ m/s}$ ) and a representative value of $C_D = 0.7$ . For this airstream velocity, all four of the coatings show $r_c \ll r_e$ . As a result of the large values of $\theta_{rec}$ (which lead to easy drop roll-off and low adhesion forces), the POSS-PEMA spraycoating (denoted PPS) shows a smaller value of $r_e$ than the half spacing $D$ of most of the woven meshes used in the fog collection experiments, which explains the low collection efficiency value we measure experimentally (because of re-entrainment of deposited water droplets back into the convected air stream). The liquid-impregnated surfaces initially exhibit a critical droplet drainage radius ( $r_c$ ) that is similar to the POSS-PEMA dipcoating (denoted PPD), but after a short period of operation this ultimately transitions to a value that is greater than the critical radius of the original polyolefin material (denoted PO). The reason for the increased value of $r_c$ for the liquid-impregnated coating is described in the next section.....	177



# CHAPTER 1

## 1. Introduction

Reproduced in part with permission from

Park, K.-C.; Choi, H. J.; Chang, C.-H.; Cohen, R. E.; McKinley, G. H.; Barbastathis, G. Nanotextured Silica Surfaces with Robust Superhydrophobicity and Omnidirectional Broadband Supertransmissivity. *ACS Nano* **2012**, *6*, 3789-3799.

Zhao, H.; Park, K.-C.; Law, K.-Y. Effect of Surface Texturing on Superoleophobicity, Contact Angle Hysteresis, and “Robustness”. *Langmuir*, **2012**, *28*, 14925-14934.

Copyright 2012 American Chemical Society.

## 1.1 Introductory Remarks

In general, interfacial phenomena include physico-chemical static and dynamic interactions occurring at the interface that divides two phases of materials.<sup>1</sup> Numerous interfacial phenomena play important roles in a wide range of areas, from nature to industrial facilities and our daily life.<sup>1-3</sup> For example, millimetric spherical water droplets that are formed on and rolled off lotus leaves have inspired a great number of research papers on nonwetting surfaces and inspired production of waterproof fabrics including Gore-Tex®.<sup>1</sup> The scope of interfacial phenomena has been extended from a narrow definition that focuses mainly on material interactions in surface chemistry to broader interests in other disciplines including optics and fluid dynamics.<sup>2,4-10</sup>

This chapter reviews the basic concepts of wetting phenomena and other important interfacial phenomena, such as optical reflection and stress/energy interactions on various textured surfaces, before exploring the discussion of core parts in this thesis. In Figure 1-1, various functional textured surfaces are categorized by the dimensionless length scale  $L/\ell_{\text{cap}}$  and complexity of topography, where  $L$  is the length scale of surface texture and  $\ell_{\text{cap}}$  is the capillary length ( $\ell_{\text{cap}} = (\gamma/\rho g)^{1/2}$ , where  $\gamma$  is the water-air interfacial tension,  $\rho$  is the density of water, and  $g$  is the standard gravity) that represents the characteristic length scale of droplets in which there is a balance between pressures by the surface tension and gravitational effects. The first section overviews the definition of interface, line tension force (or surface energy) and equilibrium contact angle, introducing Young's relation. The second section explains the effect of surface texture on the wettability of solid surfaces, with relevant concepts including two wetting models and their thermodynamical stabilities as well as critical conditions for the wetting transition



between the two models. Superwetting and super-liquid-repellency are also introduced with their useful functionalities. The third section discusses important concepts in optics and solid mechanics used in this thesis are briefly introduced related to the surface texture. In particular, optical reflection and fracture by normal and shear loads at the interface are emphasized.

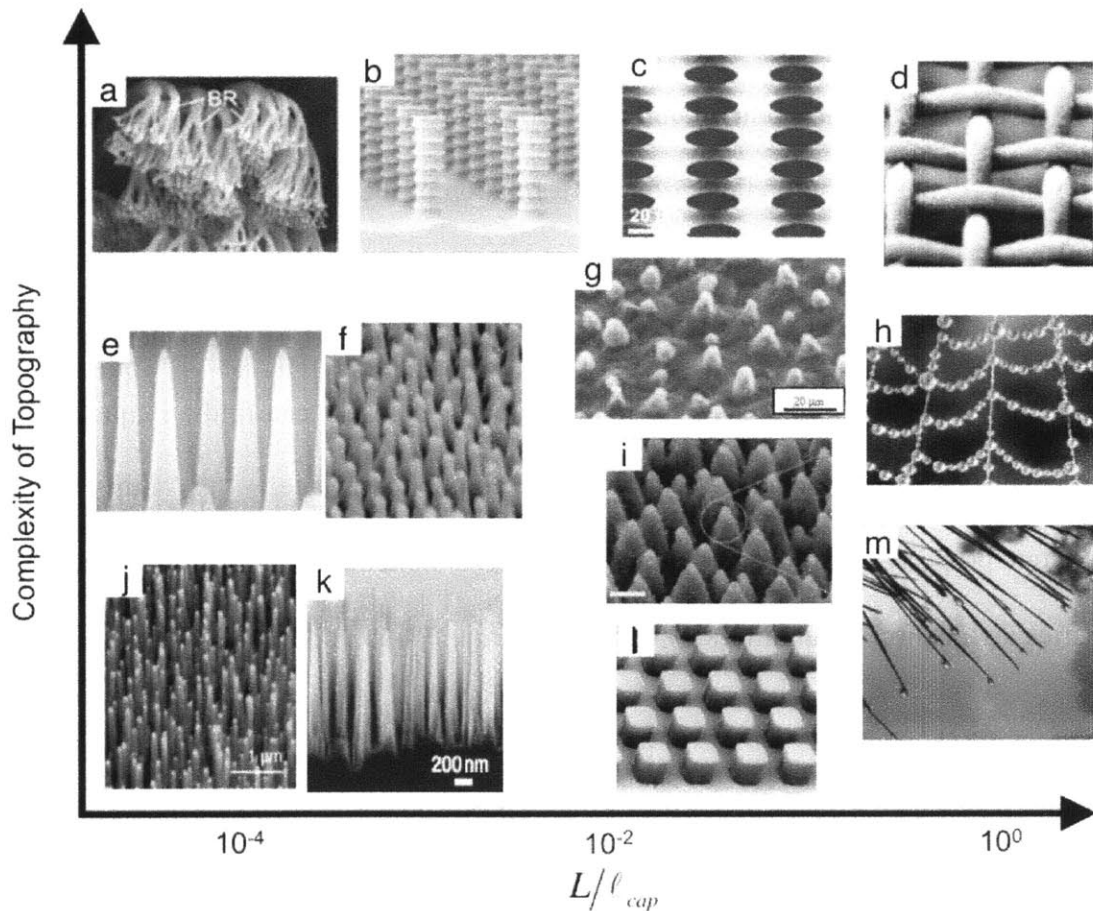


**Figure 1-1** A schematic of the topographic complexity of various natural and artificial textured surfaces as a function of the dimensionless length scale  $L/\ell_{cap}$ , where  $\ell_{cap}$  is the capillary length ( $\ell_{cap} = (\gamma/\rho g)^{1/2}$ , where  $\gamma$  is the water-air interfacial tension,  $\rho$  is the density of water, and  $g$  is the standard gravity). The surfaces are: (a) gecko foot,<sup>45</sup> (b) wavy wall structure,<sup>41</sup> (c) microhoodoo,<sup>17</sup> (d) woven mesh with corpuscular nanotexture,<sup>46</sup> (e) nanocone,<sup>31</sup> (f) cicada wing,<sup>47</sup> (g) lotus leaf,<sup>48</sup> (h) spider web (Image courtesy William Lee), (i) *Calathea Zebrina* leaf,<sup>49</sup> (j) carbon nanotube,<sup>32</sup> (k) silicon nanostructure,<sup>7</sup> (l) micropillar, (m) slender leaves of trees (Image courtesy Robert Holmes). In particular, the nanocone, wavy wall structures, micropillars, and woven meshes are intensively investigated in this thesis.

## 1.2 Interfacial Tension of Materials and Equilibrium Contact Angle

When two different materials (or phases) create an interface between them (*e.g.* when a homogeneous material is divided by introduction of a different insoluble material), the cohesive force between the atoms or molecules of a homogeneous material before the formation of the interface is replaced by the adhesion force between two different kinds of atoms or molecules at the interface.<sup>1,11</sup> This replacement of interaction force can be interpreted as the difference of thermodynamical energies before and after the formation of the interface, which is referred to as the work of adhesion.<sup>1,11</sup> When a droplet replaces vapor (or air) and contacts on the flat chemically homogeneous solid surface, then interfacial tension force per unit length (or energy per unit area) between the three phases – liquid, vapor and solid - can find an equilibrium state by force balance in the tangential direction of the flat solid surface.<sup>1,11,12</sup> At this equilibrium state, a unique property, equilibrium contact angle ( $\theta_E$ ) is determined by Young's relation, which also satisfies a global minimum in the Gibbs free energy.<sup>13,14</sup>

$$\cos\theta_E = (\gamma_{SV} - \gamma_{SL})/\gamma_{LV} \quad (1-1)$$

where  $\gamma$  refers to the interfacial tension and subscripts  $S$ ,  $L$ ,  $V$  refer to the solid, liquid and vapor (or air) phases, respectively (Figure 1-2).

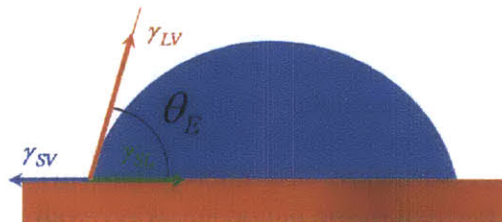


**Figure 1-2** Schematic sketch of side view of droplet (blue) on a chemically homogeneous flat surface (red), surrounded by vapor (or air).

Regarding the equilibrium state and contact angle, three important points should be noted here. First, only the surface properties, not the bulk properties of the solid or liquid plays an important role in determining this equilibrium.<sup>15</sup> Second, for interfacial tension forces normal to the flat solid surface, the Young's modulus of solid is assumed large enough to ignore the deformation of the solid that can influence the equilibrium contact angle.<sup>14</sup> Third, in many cases the existence of vapor is ignored because of its negligible difference from air.<sup>13</sup>

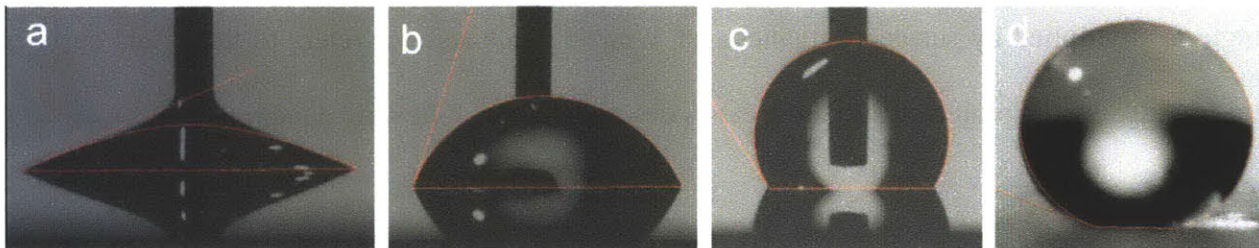


**Figure 1-3** Water contact angles on different surface coatings. (a) Superwetting ( $\theta_E < 10^\circ$ ). (b) Hydrophilic ( $\theta_E < 90^\circ$ ). (c) Hydrophobic ( $90^\circ < \theta_E < 150^\circ$ ). (d) Superwater-repellent ( $\theta_E > 150^\circ$ ).

Practically, the surface energy of solid is modified by surface coating methods in order to control the equilibrium contact angle, in particular for creating highly wetting or nonwetting surfaces.<sup>1-3,11</sup> Depending on the range of the equilibrium contact angle of the water droplet on the surface, the states with  $\theta_E < 10^\circ$ ,  $\theta_E < 90^\circ$ ,  $\theta_E > 90^\circ$ , and  $\theta_E > 150^\circ$  are referred to as superwetting, hydrophilic, hydrophobic, super water-repellent, respectively (Figure 1-3).<sup>1-3</sup>

### 1.3 Effect of Surface Texture on Wetting Phenomena

Even on a very low surface energy flat solid surface, water can obtain a maximum equilibrium contact angle of  $\theta_E = 125^\circ$ .<sup>16-18</sup> However, roughness can increase water contact angle due to the effect of surface texture according to the two models (Figure 1-4) on the apparent contact angle ( $\theta^*$ ) of liquids on textured surfaces.<sup>19,20</sup> The first model suggested by Wenzel describes the fully-wetted state of droplets on textured surfaces (Figure 1-4a).<sup>19</sup> The cosine value of apparent contact angle ( $\theta^*$ ) can be calculated as the cosine value of an equilibrium contact angle  $\theta_E$  multiplied by surface roughness (or Wenzel roughness,  $r_W$  refers to the actual surface area divided by the projected surface area) as described in the following equation.

$$\cos\theta^* = r_W \cos\theta_E \quad (1-2)$$

Here, it should be noted that hydrophilicity ( $\theta_E < 90^\circ$ ) or hydrophobicity ( $\theta_E > 90^\circ$ ) is amplified by the magnitude of roughness  $r$ .

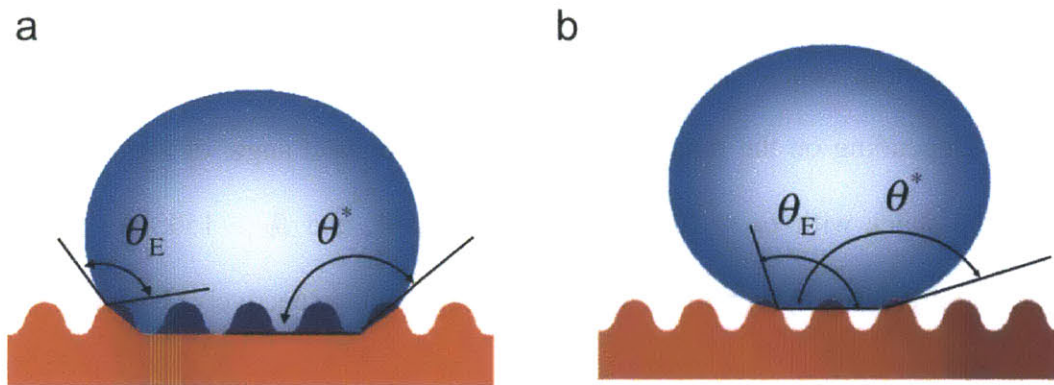


**Figure 1-4** Schematic sketches of side view of (a) the fully-wetted Wenzel state and (b) the composite Cassie-Baxter state, with the comparison between the local equilibrium contact angle ( $\theta_E$ ) and the apparent contact angle on textured surfaces ( $\theta^*$ ).<sup>21, 23</sup>

The second model referred to as Cassie-Baxter model describes a liquid-solid-air composite state in which a liquid droplet sits partially on solid asperities and partially on air pockets entrapped within the microscopic asperities (Figure 1-4b).<sup>20</sup> If the net surface tension force at the liquid-solid-air three phase contact line is sufficient to support the pressure difference across the liquid-air interface between the asperities, then the apparent contact angle  $\theta^*$  can be obtained by averaging the local equilibrium contact angle on the solid surface ( $\theta_E$ ) and on air ( $\theta_{E,air} = 180^\circ$ ) with the liquid-solid area fraction  $f_1$  and liquid-air area fraction  $f_2$ , per unit area of the composite interface.

$$\cos\theta^* = f_1 \cos\theta_E - f_2 \tag{1-3}$$

On rough surfaces, a droplet-air-solid system can have multiple local free energy ( $G$ ) minima in the process of wetting or dewetting on the surface texture (Figure 1-5a-c). This thermodynamic picture rationalizes the different values of apparent contact angle observed in advancing and receding contact lines.<sup>1,2</sup> When the droplet volume is increased and thus the three phase contact line “advances” outward on the solid-air interface by addition of liquid through the syringe connected to the droplet, then an advancing contact angle ( $\theta_{adv}$ ) for the liquid can be measured by a goniometer.<sup>1-3</sup> On the other hand, when the droplet volume is decreased and thus the contact line “recedes” in the opposite direction by suction of liquid through the syringe, then a receding contact angle ( $\theta_{rec}$ ) can be measured.<sup>1-3</sup> In general,  $\theta_{adv} \geq \theta_{rec}$  and the difference between the two values is referred to as “contact angle hysteresis (CAH)”.<sup>1-3</sup> In Chapter 5, we also define a parameter  $CAH$  related to this definition of contact angle hysteresis (CAH) as  $CAH = \cos\theta_{rec} - \cos\theta_{adv}$ . Johnson and Dettre have shown that there can be a significant difference in the contact angle hysteresis in two wetting regimes on rough surfaces with the same

surface coating.<sup>22</sup> As shown in the Figure 1-5d, the Cassie-Baxter state (greater roughness cases) shows smaller differences between the advancing and receding contact angles than the Wenzel state (smaller roughness cases) of water droplet on rough surfaces, because of smaller pinning effect in the Cassie-Baxter state compared to the greater pinning observed in the Wenzel state.<sup>22</sup> The advancing and receding contact angle values influence the sliding angle (*i.e.* the inclination angle at which a droplet starts slide off a flat surface) and droplet impact dynamics on solid surfaces because the direction of surface tension forces in the process of droplet motion are closely related to the dynamic contact angles and their differences.<sup>2</sup>

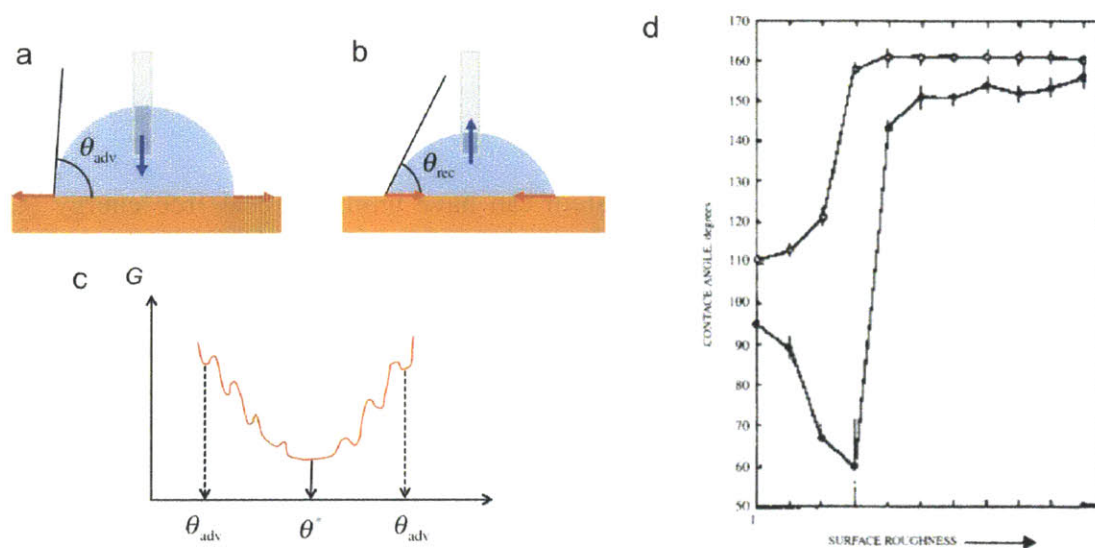


**Figure 1-5** (a-c) Advancing and receding contact angles and their locations in the schematic of free energy – apparent contact angle relation. (d) Advancing (hollow) and receding (solid) contact angles of water on rough wax surfaces, plotted versus the surface roughness.<sup>21</sup>

Water droplets can display an apparent contact angle greater than  $150^\circ$  and contact angle hysteresis less than  $5^\circ$  on such “Cassie-Baxter surfaces”, which are generally referred to as superhydrophobic surfaces.<sup>2,3</sup> On superhydrophobic surfaces, water droplets can easily roll or bounce off the nonwettable textured surfaces, leading to the ready removal of dust particles and contaminants, generally referred as to “self-cleaning”.<sup>1-3</sup>

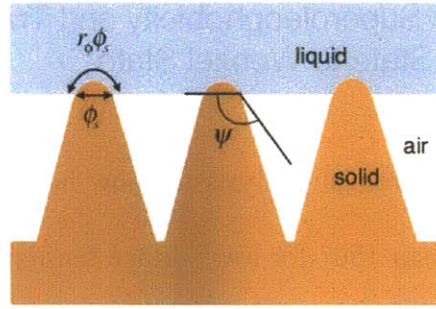


**Figure 1-6** A schematic illustration of the various characteristic geometrical parameters used in the Cassie-Baxter relation (Eq. 1-4).

On the other hand, on extremely wetting surfaces, the Wenzel state results in a superhydrophilic surface that displays an apparent contact angle less than  $10^\circ$ .<sup>1-3</sup> By changing the direction of the net surface traction of the three-phase contact line on the hydrophilic conical structure shown in Figure 1-6, so that  $\theta_{adv} - \psi < 0^\circ$ , where  $\psi$  is the texture angle defined as the angle between the horizontal line and the tangential line at the three phase contact line, the liquid meniscus is strongly imbibed into the structure with a traction force.<sup>23</sup> Higher values of the Wenzel roughness ( $r_w$ ) can promote superhydrophilicity and progressively smaller apparent contact angles by capillary imbibition.<sup>24</sup> Condensation on such surfaces promotes formation of a continuous liquid film with strong antifogging characteristics.<sup>25</sup>

In his recent work, Marmur suggested two generalized parameters  $r_\phi$  (ratio of the actual wetted area to the occluded area) and  $\phi_s$  (the area fraction of the liquid-air interface occluded by the texture, see Figure 1-6 for details) that can be used for general shape of surface texture and interpreted the Cassie-Baxter model as follows.<sup>26,27</sup>

$$\cos \theta^* = r_\phi \phi_s \cos \theta_E - (1 - \phi_s) \quad (1-4)$$

where  $f_1 = r_\phi \phi_s$  and  $f_2 = 1 - \phi_s$  (see Eq.1-3).

## 1.4 Re-entrant Structure for Superoleophobicity and Transition from Metastable Cassie-Baxter State to Wenzel State

Marmur also used his theoretical analysis to show how it is possible to achieve a high apparent contact angle greater than  $150^\circ$  for low surface tension liquids such as hexadecane or other hydrocarbon liquids, by generating thermodynamically metastable Cassie-Baxter state.<sup>27,28</sup> As shown in Figure 1-7a, typical rough structure ( $90^\circ \leq \psi < 180^\circ$ ) can support a pressure difference across the water-air interface and can exhibit superhydrophobicity because the direction of surface tension force ( $F$ ) is opposite to that of the applied pressure difference so that  $\theta_E - \psi > 0$ . On the other hand, the same structure cannot support a Cassie-Baxter state for low surface tension liquids because the equilibrium or advancing contact angles of those liquids are typically less than  $90^\circ$  and thus does not satisfy  $\theta_E - \psi > 0$  (Figure 1-7b) and the direction of surface tension is no longer opposite to that of the applied pressure difference. Tuteja *et al.* have demonstrated superoleophobicity or omniphobicity by employing appropriate re-entrant structure as shown Figure 1-8 in conjunction with appropriate surface chemistry and surface roughness.<sup>17,23,28</sup>

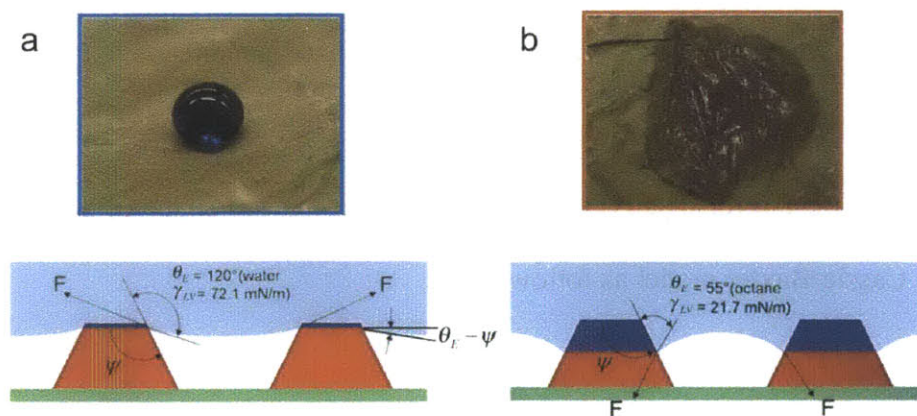


**Figure 1-7** (a) Water and (b) octane droplets on lotus leaf and schematic sketch (cross-sectional view) wetting of the two liquids on typical rough structures with a characteristic angle  $\psi$ .<sup>23</sup>



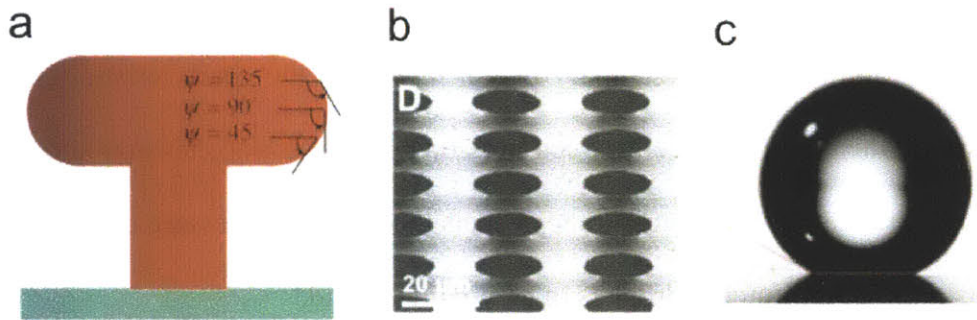


**Figure 1-8** Re-entrant structures. (a) Schematic sketches of hoodoo structure and characteristic texture angle  $\psi$  at three different points. (b) Fabricated microhoodoo structure.<sup>17</sup> (c) Superoleophobicity of a microhoodoo surface (for octane,  $\gamma_{LV} = 21.6$  mN/m).<sup>17</sup>

In contrast to the global free energy minimum of superhydrophobic state created by low surface energy coating and surface roughness, the metastability of the superoleophobic Cassie-Baxter state has led to more intensive discussions on the critical conditions that give rise to a transition to the Wenzel state by external perturbation such as drop impact or vibration.<sup>3,23,28</sup> Beyond the critical pressure difference (referred to as “breakthrough pressure ( $P_B$ )” or “impalement pressure”, the maximum pressure difference that the liquid-air interface can maintain), the surface loses its super liquid repellency and “wets out” until the liquid is removed by evaporation or wiping.<sup>3,23,28,29</sup>

As we show in Figure 1-9, there are two scenarios on the wetting transition from the Cassie-Baxter state to the Wenzel state.<sup>28-30</sup> The “touch down” or “sag” impalement (Figure 1-9a) describes the instantaneous wetting once the lowest part of liquid-air interface touches the bottom of textured surfaces and the other “depinning” impalement (Figure 1-9b) represents the gradual descending of three phase contact line when  $\theta \rightarrow \theta_{adv}$ .<sup>28-30</sup> Tuteja *et al.* proposed dimensionless design parameters based on the two scenarios, which can evaluate the robustness of the metastable Cassie-Baxter state by scaling the breakthrough pressure with a reference

pressure ( $P_{ref}$ ).<sup>28</sup> The reference pressure is chosen as the Laplace pressure of a liquid droplet with the diameter of capillary length ( $\ell_{cap} = (\gamma/\rho g)^{1/2}$ ) where  $\rho$  is the liquid density, and  $g$  is the acceleration due to gravity.<sup>28</sup> The capillary length represents the characteristic length scale of droplets in which there is a balance between pressures by the surface tension and gravitational effects.<sup>1,2</sup> Therefore the reference pressure represents the minimum pressure difference across the meniscus arising from millimetric droplets in gravitational field.<sup>21, 28</sup>

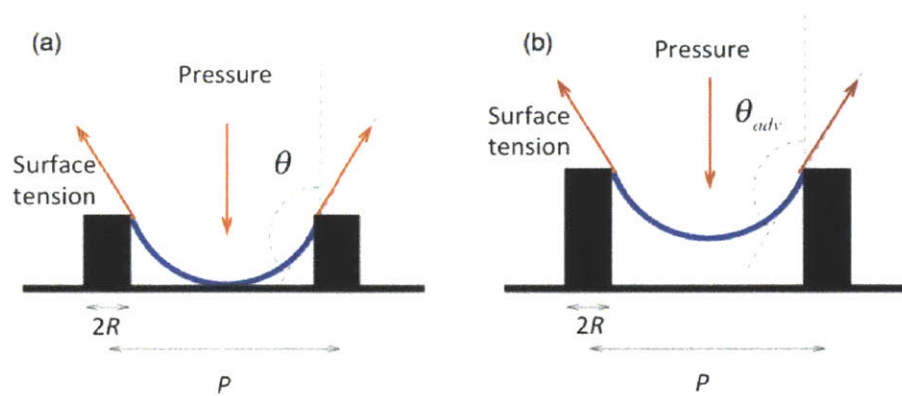


**Figure 1-9** Two wetting transition modes. (a) Touch down transition when the apex of the meniscus touches the substrate. (b) Depinning transition when the angle the meniscus makes with the texture reaches the advancing contact angle.<sup>29</sup>

The wetting transition condition is influenced by the combination of equilibrium contact angle and spacing, height, and periodicity of surface texture.<sup>2,3,28,31</sup> Increasing the aspect ratio of the texture and incorporating a very low solid-phase surface energy helps to eliminate wetting transitions between the Cassie-Baxter state and the Wenzel state that are associated with contact line depinning events.<sup>31</sup> In addition to high aspect ratios, studies have shown that an array of high aspect ratio posts with large number density can show superhydrophobicity with strong resistance against transition to the Wenzel state.<sup>31-34</sup>

The hydrodynamic interaction of impacting rain droplets with textured solid surfaces is an important design feature of robust superhydrophobic surfaces deployed in the environment.<sup>31</sup> The weak shock generated by the impact of a droplet on a rigid impenetrable surface can generate dynamic pressures that are much higher than the static Laplace pressure.<sup>35</sup> The initial impact generates a water hammer pressure ( $P_{WH} \sim 0.5\rho cV$ ) where  $\rho$  is the density of water ( $\approx 1000 \text{ kg/m}^3$ ),  $c$  is speed of sound in water ( $\approx 1500 \text{ m/s}$ ) and  $V$  is the impact velocity, respectively, which decays rapidly ( $t_{WH} \sim Ma^2 R/V$ , where  $Ma$  is the Mach number and  $R$  is the radius of impacting liquid droplet) to a Bernoulli pressure ( $P_B \sim \rho V^2$ ).<sup>36-38</sup> Under these dynamic conditions even apparently-robust textured nonwetting surfaces can lose their superhydrophobicity.<sup>39</sup> For example, while typical micrometric textured post arrays can support breakthrough pressures on the order of 1 kPa, the maximum dynamic impact pressure of raindrops with typical impact velocities in the range of  $0.3 \text{ m/s} \leq V \leq 5 \text{ m/s}$ , is approximately one thousand times higher, corresponding to pressure differences in the range of  $0.23 \text{ MPa} \leq P_{WH} \leq 3.8 \text{ MPa}$ .<sup>40</sup>

## 1.5 Mechanical Durability of Textured Surfaces

In addition to the robustness of the Cassie-Baxter state of a liquid-air-solid meniscus on textured surfaces, the mechanical durability of the surface is one of another substantial points that preserve the surface texture for super-nonwettability.<sup>31,41</sup> For practical applications under various conditions of shear or normal loading conditions on the surface texture, the slender features of the nanotexture can be damaged through either bending or buckling fracture (Figure 1-10), depending on the magnitude and direction of loads.<sup>31,41,42</sup> For example, mechanical

modeling shows that bending of the pillars is the key failure mode in abrasion, which can be avoided with a short pillar structure.<sup>41</sup> A typical such case of concern is the dynamic pressure (several MPa) associated with impact of raindrops.<sup>31</sup> The critical conditions for fracture by buckling and bending are reviewed in this thesis. The path to fabricate a superoleophobic surface that can withstand external force equivalent of a gentle cleaning blade (up to  $\sim 30$  kPa) without wetting and abrasion failure is also discussed.<sup>41</sup>

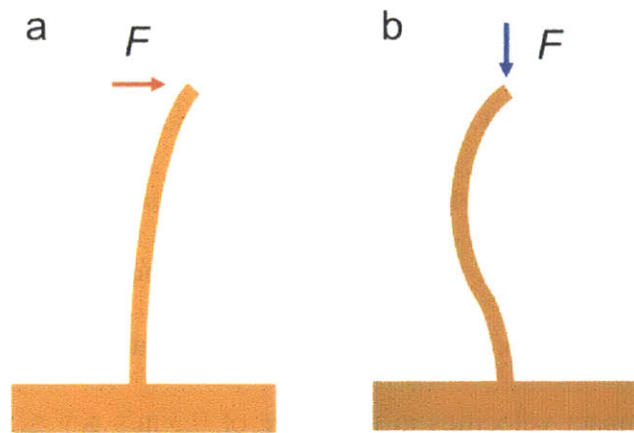


**Figure 1-10** Two modes of distortion of slender beam that lead to the fracture. (a) Bending by shear load. (b) Buckling by normal load.<sup>42</sup>

## 1.6 Reflection at Optical Interfaces

Similar to the droplet impact, many photons (or electromagnetic waves) approach a typical air-solid interface and show interesting interaction associated with the change of refractive index from one material to another material, leading to the creation of reflection as shown in Figure 1-11.<sup>43</sup> Researchers have shown that the moth eye exploits the nanopillar arrays shown in Figure 1-1 to suppress reflection by reducing the sudden refractive index change at the interface between air and solid material.<sup>43</sup> The solid nanopillar arrays have a lateral period  $P$  of

approximately  $P \approx 200$  nm of lateral period and submicrometer height which gradually increase or decrease the relative fraction between air and solid in the direction of light, regardless of its incidence angle so that the average refractive index changes smoothly between two materials, which is referred to as “adiabatic index-matching”<sup>7, 8, 44</sup>.

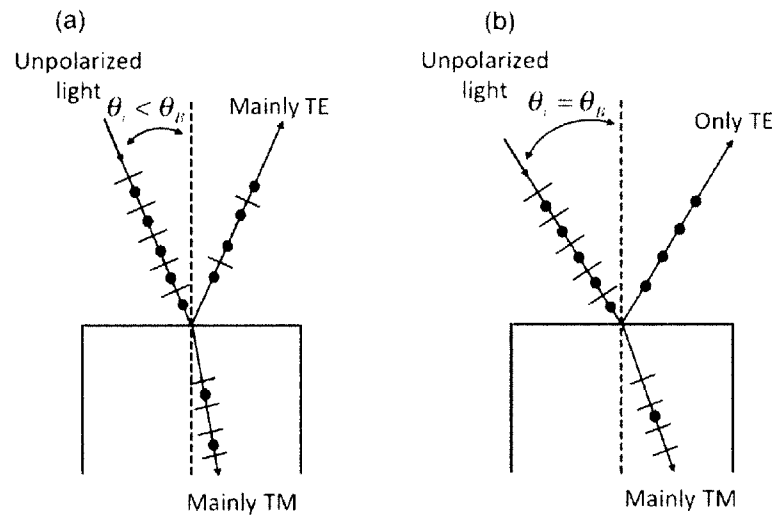


**Figure 1-11** Schematics of refracted and reflected waves (s-polarized or transverse electric (TE) light and p-polarized or transverse magnetic (TM) light) at an interface between air and glass plate (a) when an incident angle ( $\theta_i$ ) is smaller than Brewster’s angle ( $\theta_B$ )<sup>43</sup> and (b) when an incident angle is equal to Brewster’s angle ( $\theta_i = \theta_B$ ) (Copyright, Center for Occupational Research and Development). The oscillation of electric dipoles in the incident plane influences the reflected waves.<sup>43</sup>

In this thesis, we employ the design of tapered conical nanotextures to fabricate broadband omnidirectional anti-reflective surfaces; the slender conical features result in a large topographic roughness (corresponding to high  $r_\phi$  and low  $\phi_s$ ) whilst the axial gradient in the effective refractive index minimizes reflection through adiabatic index-matching between air and the substrate.<sup>31</sup>

## 1.7 Thesis Objectives and Outline

In this thesis, we will explore a broad range of interfacial phenomena associated with droplet dynamics on textured surface. The first step is understanding of existing natural and artificial nonwetting surfaces and relevant interdisciplinary principles including optics, solid mechanics, and rheology. Applying analytical and numerical calculations for the design of a variety of micro/nanotextured surfaces with different scientific/engineering goals, we fabricated tapered conical nanotextures, nanopillars with wavy sidewall, micropillars, and permeable woven meshes. The experimental results demonstrate our designed functionalities, suggesting future directions for practical design of functional surfaces.

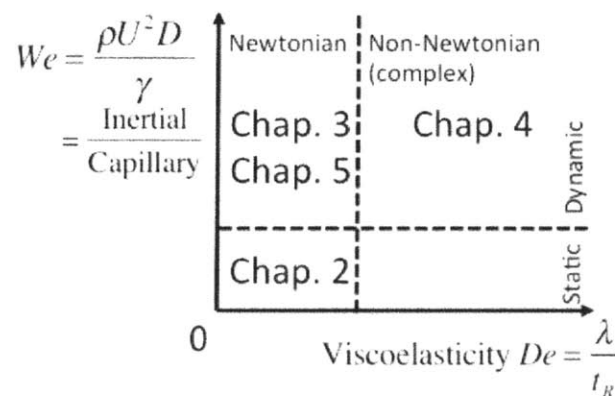


**Figure 1-12** Region of each thesis chapter in the dimensionless physico-chemical properties space composed of two important dimensionless numbers. Weber number ( $We = \rho U^2 D / \gamma$ ) characterizes inertial effect relative to capillary effect, where  $\rho$  is the density of liquid,  $U$  is the velocity of droplet,  $D$  is the diameter of droplet, and  $\gamma$  is the liquid-air interfacial tension. Deborah number ( $De = \lambda / t_R$ ) characterizes viscoelasticity, where  $\lambda$  is the relaxation time and  $t_R$  is the Rayleigh time.

Each chapter of this thesis can be categorized as shown in Figure 1-12. In Chapter 2, we start to study the interaction between textured surfaces and sessile water droplets corresponding to static Newtonian fluids ( $We = 0, De = 0$ ). Our investigation in Chapter 3 includes the region of

dynamic Newtonian fluids ( $We > 0$ ,  $De = 0$ ), in particular low surface tension liquids. Then we move to the region of dynamic non-Newtonian (or complex) fluids ( $We > 0$ ,  $De > 0$ ) that possess viscoelasticity in Chapter 4. After exploring millimetric droplets regions, we investigate the region of micrometric fog droplets corresponding to dynamic Newtonian fluids ( $We > 0$ ,  $De = 0$ ).

In specific, Chapter 2 of this thesis aims at the development of superhydrophobic and superphotophilic surfaces (i.e. highly transmissive surfaces that suppress reflection and scattering of light at the interface). Designing multifunctional surfaces that have user-specified interactions with impacting liquids and with incident light is a topic of both fundamental and practical significance. Taking cues from nature, we use tapered conical nanotextures to fabricate the multifunctional surfaces; the slender conical features result in large topographic roughness whilst the axial gradient in the effective refractive index minimizes reflection through adiabatic index-matching between air and the substrate. Precise geometric control of the conical shape and slenderness of the features as well as periodicity at the nanoscale are all keys to optimizing the multi-functionality of the textured surface, but at the same time these demands pose the toughest fabrication challenges. Here we report a systematic approach to concurrent design of optimal structures in the fluidic and optical domains, and a fabrication procedure that achieves the desired aspect ratios and periodicities with few defects, and large pattern area. Our fabricated nanostructures demonstrate structural superhydrophilicity or, in combination with a suitable chemical coating, robust superhydrophobicity. Enhanced polarization-independent optical transmission exceeding 98% has also been achieved over a broad range of bandwidth and incident angles. These nanotextured surfaces are also robustly anti-fogging or self-cleaning offering potential benefits for applications such as photovoltaic solar cells.

In Chapter 3, the robustness issue in the previous chapter is extended to superoleophobicity and mechanical durability. The effect of surface texturing (pillar size, spacing and height) of a fluorosilane (FOTS) modified pillar array silicon surface comprising of  $\sim 3 \mu\text{m}$  diameter pillars ( $6 \mu\text{m}$  pitch with  $\sim 7 \mu\text{m}$  height) that is both superhydrophobic and superoleophobic on wettability, contact angle hysteresis and “robustness” are investigated. We study the static, advancing and receding contact angles as well as the droplet sliding or “roll-off” angles as a function of the solid area fraction. The results reveal that pillar size and pillar spacing have very little effect on the static and advancing contact angles as they are found to be insensitive to the solid area fraction  $0.04 \leq \phi_s \leq 0.4$  as the pillar diameter varies from 1 to 5  $\mu\text{m}$  and the center-to-center spacing varies from 4.5 to 12  $\mu\text{m}$ . On the other hand, sliding angle, receding contact angle and contact angle hysteresis are found to be dependent on the solid area fraction. Surface Evolver modeling shows that water droplets wet and pin along the top of the pillar surface whereas hexadecane wets the pillar surface and then penetrates into the sidewall of the pillar with the contact line pinning underneath the re-entrant structure shown in Figure 1-1. Due to the partial penetration of the hexadecane drop into the pillar structure, the effect on the receding contact angle and hysteresis is larger relative to water. A larger cap thickness effect (see Figure 1-8 for the schematic of hoodoo or overhang structure) is observed with octane due to its lower surface tension. The robustness of the pillar array surface against external pressure induced wetting and abrasion is modeled. Mechanical modeling shows that bending of the pillars is the key to resisting failure by abrasion, which can be avoided with a short pillar structure. The path to fabricate a superoleophobic surface that can withstand external force equivalent of a gentle cleaning blade (up to  $\sim 30 \text{ kPa}$ ) without wetting and abrasion failure is discussed.



Chapter 4 extends the scope of liquid rheology on the droplet dynamics by moving beyond Newtonian liquids to the study of complex liquids. The deposition of aqueous drops on non-wetting surfaces is an important canonical problem for many applications, including suppressing rebound of sprayed herbicides on intrinsically hydrophobic plant leaves, for inkjet printing and for spray coating applications. The addition of a small amount of high molecular weight polymer has been demonstrated to suppress drop rebound on smooth hydrophobic surfaces, though the mechanism is still being debated in the literature. In this thesis, we aim to understand the underlying mechanism, and further explore how viscoelasticity influences drop impact outcomes on textured surfaces. We present drop impact experiments of well-characterized viscoelastic fluids on micro- and nano-textured superhydrophobic surfaces in addition to smooth hydrophobic surfaces. We show that the impact of viscoelastic drops on nano-textured surfaces can result in complete rebound. By adopting a stick-slip flow model on textured surfaces with various topographic length scales and solid area fractions, we rationalize the dynamics leading to complete rebound following drop impact even for viscoelastic fluids.

Finally in Chapter 5, we focus on another area of droplet dynamics – collection of very small water droplets using permeable structures. Fog represents a large, untapped source of potable water, especially in arid climates. Various plants and animals use textural as well as chemical features on their surfaces to harvest this precious resource. In this thesis, we investigate the influence of surface wettability characteristics, length scale, and weave density on the fog harvesting capability of woven meshes. We develop a combined hydrodynamic and surface wettability model to predict the overall fog collection efficiency of the meshes and cast the findings in the form of a design chart. Two limiting surface wettability constraints govern re-entrainment of collected droplets and clogging of mesh openings. Appropriate tuning of the

wetting characteristics of the surfaces, reducing the wire radii, and optimizing the wire spacing all lead to more efficient fog collection. We use a family of coated meshes with a directed stream of fog droplets to simulate a natural foggy environment and demonstrate a five-fold enhancement in the fog-collecting efficiency of a conventional polyolefin mesh. The design rules developed in this thesis can be applied to select a mesh surface with optimal topography and wetting characteristics to harvest enhanced water fluxes over a wide range of natural convected fog environments.

## References

1. Butt, H.-J.; Graf, K.; Kappl, M. *Physics and Chemistry of Interfaces*; Wiley-VCH: Weinheim, 2006.
2. Quéré, D. Wetting and Roughness. *Annu. Rev. Mater. Res.* **2008**, *38*, 71-99.
3. Bhushan, B.; Jung, Y. C.; Koch, K. Micro-, Nano- and Hierarchical Structures for Superhydrophobicity, Self Cleaning, and Low Adhesion. *Philos. Trans. R. Soc., A* **2009**, *367*, 1631-1672.
4. Yarin, A. L. Drop Impact Dynamics: Splashing, Spreading, Receding, Bouncing. *Annual Review of Fluid Mechanics.* **2006**, *38*, 159-192.
5. Reyssat, M.; Richard, D.; Clanet, C.; Quere, D. Dynamical Superhydrophobicity. *Faraday Discuss.* **2010**, *146*, 19-33.
6. Li, Y.; Zhang, J.; Zhu, S.; Dong, H.; Jia, F.; Wang, Z.; Tang, Y.; Zhang, L.; Zhang, S.; Yang, B. Bioinspired Silica Surfaces with near-Infrared Improved Transmittance and Superhydrophobicity by Colloidal Lithography. *Langmuir* **2010**, *26*, 9842-9847.
7. Huang, Y.-F.; Chattopadhyay, S.; Jen, Y.-J.; Peng, C.-Y.; Liu, T.-A.; Hsu, Y.-K.; Pan, C.-L.; Lo, H.-C.; Hsu, C.-H.; Chang, Y.-H.; *et al.* Improved Broadband and Quasi-Omnidirectional Anti-Reflection Properties with Biomimetic Silicon Nanostructures. *Nat. Nanotechnol.* **2007**, *2*, 770-774.
8. Choi, K.; Park, S. H.; Song, Y. M.; Lee, Y. T.; Hwangbo, C. K.; Yang, H.; Lee, H. S. Nano-Tailoring the Surface Structure for the Monolithic High-Performance Antireflection Polymer Film. *Adv. Mater.* **2010**, *22*, 3713-3718.
9. Deinega, A.; Valuev, I.; Potapkin, B.; Lozovik, Y. Minimizing Light Reflection from Dielectric Textured Surfaces. *J. Opt. Soc. Am. A* **2011**, *28*, 770-777.
10. Grann, E. B.; Moharam, M. G.; Pommet, D. A. Optimal Design for Antireflection Tapered Two Dimensional Subwavelength Grating Structure. *J. Opt. Soc. Am. A* **1995**, *12*, 333-339.
11. Hiemenz, P. C.; Rajagopalan, R. *Principles of Colloid and Surface Chemistry*; CRC Press: Boca Raton, 1997.
12. de Gennes, P. G. Wetting: Statics and Dynamics. *Rev. Mod. Phys.* **1985**, *57*, 827-863.
13. Young, T. An Essay on the Cohesion of Fluids. *Phil. Trans. R. Soc. A.* **1805**, *95*, 65.
14. Blokhuis, E. M.; Shilkrot, Y.; Widom, B. Young's Law with Gravity. *Molecular Phys.* **1995**, *86*, 891-899.

15. Zisman, W. A. Relation of the Equilibrium Contact Angle to Liquid and Solid Construction. In Contact Angle, Wettability and Adhesion, ACS Advances in Chemistry Series. *American Chemical Society*: Washington DC, 1964.
16. Hishino, T.; Meguro, M.; Nakamae, K.; Matsushita, M.; Ueda, Y. The Lowest Surface Free Energy Based on –CF<sub>3</sub> Alignment. *Langmuir* **1999**, *15*, 4321-4323.
17. Tuteja, A. et al. Designing Superoleophobic Surfaces. *Science* **2007**, *318*, 1618-1622.
18. Mabry, J. M.; Vij, A. Iacono, S. T.; Viers, B. D. Fluorinated Polyhedral Oligomeric Silsesquioxanes (F-POSS). *Ange. Chem. Int. Ed.* **2008**, *47*, 4137-4140.
19. Wenzel, R. N. Resistance of Solid Surfaces to Wetting by Water. *Ind. Eng. Chem.* **1936**, *28*, 988-994.
20. Cassie, A. B. D.; Baxter, S. Wettability of Porous Surfaces. *Trans. Faraday Soc.* **1944**, *40*, 0546-0550.
21. Choi, W. Micro-Textured Surfaces for Omniphobicity and Drag-Reduction. *Massachusetts Institute of Technology, PhD Thesis*, **2010**.
22. Johnson, R. E.; Dettre, R. H. Contact Angle Hysteresis. In Contact Angle, Wettability and Adhesion, ACS Advances in Chemistry Series. *American Chemical Society*: Washington DC, 1964.
23. Tuteja, A.; Choi, W.; McKinley, G. H.; Cohen, R. E.; Rubner, M. F. Design Parameters for Superhydrophobicity and Superoleophobicity. *MRS Bull.* **2008**, *33*, 752-758.
24. Reyssat, M.; Courbin, L.; Reyssat, E.; Stone, H. A. Imbibition in Geometries with Axial Variations. *J. Fluid Mech.* **2008**, *615*, 335-344.
25. Cebeci, F. C.; Wu, Z. Z.; Zhai, L.; Cohen, R. E.; Rubner, M. F. Nanoporosity-Driven Superhydrophilicity: A Means to Create Multifunctional Antifogging Coatings. *Langmuir* **2006**, *22*, 2856-2862.
26. Marmur, A. Wetting on Hydrophobic Rough Surfaces: To be Heterogeneous or not to be? *Langmuir* **2003**, *19*, 8343-8348.
27. Marmur, A. From Hydrophilic to Superhydrophobic: Theoretical Conditions for Making High-contact-angle Surfaces from Low-contact-angle Materials. *Langmuir* **2008**, *24*, 7573-7579.
28. Tuteja, A.; Choi, W.; Mabry, J. M.; McKinley, G. H.; Cohen, R. E. Robust Omniphobic Surfaces. *Proc. Natl. Acad. Sci. U. S. A.* **2008**, *105*, 18200-5.
29. Bartolo, D.; Bouamrine, F.; Verneuil, É.; Buguin, A.; Silberzan, P.; Moulinet, S. Bouncing or Sticky Droplets: Impalement Transitions on Superhydrophobic Micropatterned Surfaces. *Europhys. Lett.* **2006**, *74*, 299-305.

30. Papadopoulos, P.; Mammen, L.; Deng, X.; Vollmer, D.; Butt, H.-J. How Superhydrophobicity Breaks Down. *Proc. Natl. Acad. Sci. U. S. A.* **2013**, *Early Edition*, 1-5.
31. Park, K.-C.; Choi, H. J.; Chang, C.-H.; Cohen, R. E.; McKinley, G. H.; Barbastathis, G. Nanotextured Silica Surfaces with Robust Superhydrophobicity and Omnidirectional Broadband Supertransmissivity. *ACS Nano* **2012**, *6*, 3789-3799.
32. Lau, K. K. S.; Bico, J.; Teo, K. B. K.; Chhowalla, M.; Amaratunga, G. A. J.; Milne, W. I.; McKinley, G. H.; Gleason, K. K. Superhydrophobic Carbon Nanotube Forests. *Nano Lett.* **2003**, *3*, 1701-1705.
33. Journet, C.; Moulinet, S.; Ybert, C.; Purcell, S. T.; Bocquet, L. Contact Angle Measurements on Superhydrophobic Carbon Nanotube Forests: Effect of Fluid Pressure. *Europhys. Lett.* **2005**, *71*, 104-109.
34. Nosonovsky, M., Bhushan, B. Roughness Optimization for Biomimetic Superhydrophobic Surfaces. *Microsyst. Technol.* **2005**, *11*, 535-549.
35. Eggers, J.; Fontelos, M. A.; Josserand, C.; Zaleski, S. Drop Dynamics after Impact on a Solid Wall: Theory and Simulations. *Phys. Fluids* **2010**, *22*, 062101.
36. Lesser, M. Analytic Solutions of Liquid-Drop Impact Problems. *Proc. R. Soc. A* **1981**, *377*, 289-308.
37. Rosenblatt, M.; Ito, Y. M.; Eggum, G. E. Analysis of Brittle Target Fracture from a Subsonic Water Drop Impact. In *Erosion: Prevention and Useful Applications*; Adler, W. F., Ed. American Society for Testing and Materials: 1979; pp 227-254.
38. Sanada, T.; Ando, K.; Colonius, T. In *Numerical Analysis of High Speed Droplet Impact*, 7th Intl. Conf. on Multiphase Flow, Tampa, FL, May 30-June 4; 2010.
39. Li, X.; Ma, X.; Lan, Z. Dynamic Behavior of the Water Droplet Impact on a Textured Hydrophobic/Superhydrophobic Surface: The Effect of the Remaining Liquid Film Arising on the Pillars' Tops on the Contact Time. *Langmuir* **2009**, *26*, 4831-4838.
40. Zorba, V.; Stratakis, E.; Barberoglou, M.; Spanakis, E.; Panagiotis, T.; Anastasiadis, S. H.; Fotakis, C. Biomimetic Artificial Surfaces Quantitatively Reproduce the Water Repellency of a Lotus Leaf. *Adv. Mater.* **2008**, *20*, 4049-4054.
41. Zhao, H.; Park, K.-C.; Law, K.-Y. Effect of Surface Texturing on Superoleophobicity, Contact Angle Hysteresis, and "Robustness". *Langmuir*, **2012**, *28*, 14925-14934.
42. Timoshenko, S. P.; Gere, J. M. *Theory of Elastic Stability*. McGraw-Hill: New York, 1961.
43. Hecht, E. *Optics*. Addison Wesley: San Francisco, 2002.
44. Kanamori, Y.; Sasaki, M.; Hane, K. Broadband Antireflection Gratings Fabricated Upon Silicon Substrates. *Opt. Lett.* **1999**, *24*, 1422-1424.
45. Gao, H.; Wang, X.; Yao, H.; Gorb, S; Arzt, E. Mechanics of hierarchical adhesion

structures of geckos. *Mech. Mater.* **2005**, *37*, 275–285.

46. Srinivasan, S.; Choi, W.; Park, K.-C.; Chhatre, S. S.; Cohen, R. E.; McKinley, G. H. Drag reduction for viscous laminar flow on spray-coated non-wetting surfaces. *Soft Matter* **2013**, *9*, 5691-5702.

47. Xie, G.; Zhang, G.; Lin, F.; Zhang, J.; Liu, Z.; Mu, S. The Fabrication of Subwavelength Anti-Reflective Nanostructures Using a Bio-Template. *Nanotechnology* **2008**, *19*, 095605.

48. Barthlott, W.; Neinhuis, C. Purity of the Sacred Lotus, or Escape from Contamination in Biological Surfaces. *Planta* **1997**, *202*, 1-8.

49. Schulte, A. J.; Koch, K.; Spaeth, M.; Barthlott, W. Biomimetic Replicas: Transfer of Complex Architectures with Different Optical Properties from Plant Surfaces on Technical Materials. *Acta Biomater.* **2009**, *5*, 1848-1854.

# CHAPTER 2

## 2. Design of Silica Nanocone Structures for Transparent Superhydrophobic and Supertransmissive Surfaces

Reproduced with permission from

Park, K.-C.; Choi, H. J.; Chang, C.-H.; Cohen, R. E.; McKinley, G. H.; Barbastathis, G. Nanotextured Silica Surfaces with Robust Superhydrophobicity and Omnidirectional Broadband Supertransmissivity. *ACS Nano* **2012**, *6*, 3789-3799.

Copyright 2012 American Chemical Society.

## 2.1 Introduction and Theory

### 2.1.1 Analysis of Natural and Artificial Textured Surfaces

Natural biological surfaces have evolved to optimize their physicochemical properties and structures at the micro/nanoscale for a wide variety of functions, ranging from wettability to optical properties.<sup>1-3</sup> Microscopic studies of the textured surfaces commonly encountered on living organisms, *e.g.* lotus leaves, desert beetles, and moth eyes, have revealed complementary roles of material properties and texture on the surface functionalities that have been developed during adaptation to different environments.<sup>4-8</sup> These studies have in turn inspired biomimetic surfaces emulating the self-cleaning,<sup>9-13</sup> water harvesting,<sup>6</sup> and anti-reflective<sup>14-18</sup> capabilities of functional surfaces found in nature. It has also been recognized recently that many natural surfaces are not optimized solely for their responsiveness to a single functional requirement; nature is an excellent architect for designing and optimizing surfaces that fulfill multiple purposes.<sup>19</sup>

Multifunctionality is also critical for practical engineering applications such as energy harvesting and operation of optical instrumentation in extreme climates or humid conditions where the wetting, reflectivity, and other surface properties must satisfy optimally multiple design characteristics in order to fulfill system requirements.<sup>20, 21</sup> For example, the collecting efficiency of a photovoltaic solar cell is highly influenced by both surface dust contamination and Fresnel reflection losses over a broad range of wavelengths and incident angles.<sup>15, 20, 21</sup> The operational efficiency and longevity would benefit from both self-cleaning and anti-reflection surface properties. To achieve the high transmissivity required for operation of optical



instrumentation under humid conditions in chemical and biological laboratories, antifogging and anti-reflection as well as enhanced transparency would convey critical advantages and these multifunctional surface design strategies could also find practical utility in enhanced performance characteristics of common objects such as goggles and vehicle windshields.<sup>22</sup> However, coupled analyses of the functional design constraints followed by integrative design and simultaneous realization of specified wetting and optical functions have been rare and limited to simple pairwise combinations from two distinct fields.<sup>15, 19-21, 23</sup>

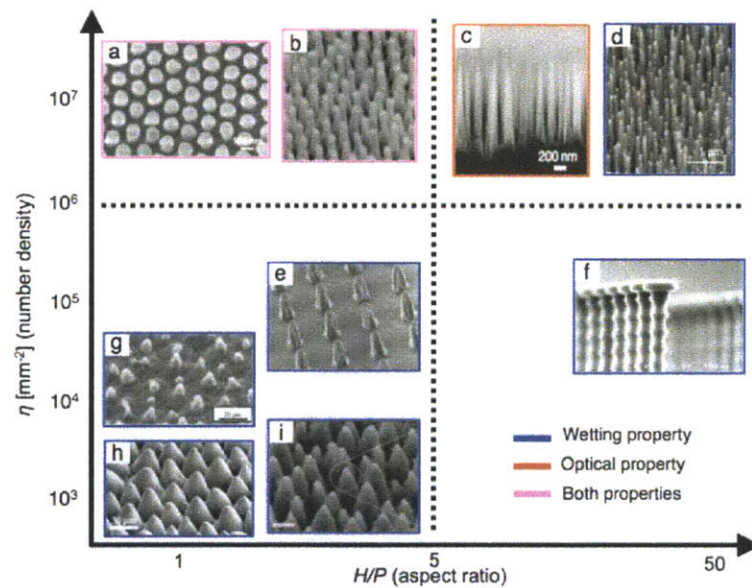


**Figure 2-1** Plot of the number density ( $\eta$ ) of nanoscale features as a function of the aspect ratio ( $H/P$ ) for natural and artificial textured surfaces. The surfaces are: a) mosquito eye, b) cicada wing, c) silicon nanostructure, d) carbon nanotube, e) perfluoropolyether nanopillar (diameter at the base of pillars  $\approx 500$  nm), f) nanonail, g) *Calathea Zebrina* leaf, h) lotus leaf, and i) microconical structure. Reprinted with permission from ref 23 (a, Copyright 2007 Wiley-VCH), ref 18 (b, Copyright 2008 IOP Publishing Ltd), ref 31 (c, Copyright 2007 Nature Publishing Group), ref 12 (d, Copyright 2003 ACS), ref 13 (f, Copyright 2008 ACS), ref 27 (g, Copyright 2009 Elsevier), ref 1 (h, Copyright Springer-Verlag 1997), and ref 49 (i, Copyright 2008 Wiley-VCH). To maximize transmission by minimizing reflection, a number density greater than the horizontal borderline (for circumventing interference effects of light) and an aspect ratio close to the vertical borderline (associated with the fracture by bending or buckling of high aspect ratio nanostructure (see 2.1.3)) are required.

The competing constraints associated with multifunctional features such as water-wettability, anti-reflectivity, optical transparency, and mechanical robustness that we seek in this thesis can be compared quantitatively by design charts that rank various natural and artificial surfaces in terms of the number density of features  $\eta$ , *i.e.*, the number of asperities in  $1 \text{ mm}^2$ , (which is inversely proportional to their period  $P = 2R$ ) and their aspect ratio  $H/P$  as shown in Figure 2-1 and 2-2A. In studies of super-repellency, the canonical natural example is the surface of the lotus leaf, *Nelumbo nucifera* ( $\eta \approx 3 \times 10^3$ ,  $H/P \approx 0.5$ ). Studies have revealed that its superhydrophobicity (*i.e.*, exhibiting apparent contact angles with water  $\theta^* \geq 150^\circ$  and low contact angle hysteresis) arises from both hierarchical roughness and the intrinsic chemical characteristics of the surface.

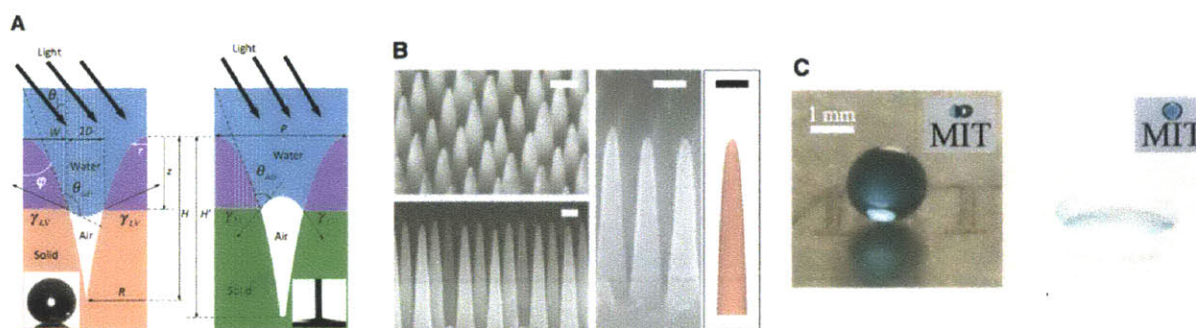


**Figure 2-2** Design and development of optimal nanostructured multi-functional surfaces. (A) Schematic drawings of the three phase contact line on hydrophobically-modified and hydrophilic (as fabricated) nanotaper structures. The insets show corresponding goniometer images for  $5 \mu\text{l}$  droplets with apparent contact angles of  $\theta^* \approx 165^\circ$  and  $\theta^* \leq 5^\circ$  respectively. (B) Micrograph of the final developed nanotaper structure with numerical rendering of a cubic paraboloid. All scale bars represent 200 nm. (C) Blue-dyed water droplets sitting on a transparent nanotaper surface and on flat glass, each placed on top of printed black letters. The insets are top views of the same two surfaces. The very weak reflection and high contact angle of the tapered nanocone surface are in contrast to the intense reflection and low contact angle of water on flat glass.

On rough surfaces, the wetting characteristics of water droplets can be explained through two distinct models.<sup>4, 5</sup> The Wenzel model (Eq. 1-2)<sup>4</sup> describes sessile droplets that fully wet the surface texture. On the other hand, the Cassie-Baxter model (Eq. 1-3)<sup>5</sup> describes water droplets that reside partially on the solid texture and partially on a raft of air pockets entrapped within the microscopic texture which enable the surface to become superhydrophobic. On such ‘Cassie-Baxter surfaces’, water droplets can easily roll or bounce off, leading to the ready removal of dust particles and contaminants.<sup>1, 10, 11</sup> Increasing the aspect ratio ( $H/P$ ) of the texture and incorporating a very low solid-phase surface energy helps to eliminate wetting transitions between the Cassie-Baxter state and the Wenzel state that are associated with contact line depinning events.<sup>10</sup>

In addition to high aspect ratios ( $H/P \gg 1$ ), the feature density, characteristic geometric length scale and topography of the surface texture all play pivotal roles in creating superhydrophobic surfaces that exhibit robust Cassie-Baxter interfaces and that can resist wetting under dynamic conditions.<sup>11, 12, 24, 25</sup> Studies have shown that an array of high aspect ratio posts with large number density (*e.g.*, a chemically treated carbon nanotube forest as shown in Figure 2-1d) can show superhydrophobicity with strong resistance against transition to the Wenzel state.<sup>12, 25</sup> This irreversible transition occurs when the applied pressure difference between the liquid drop sitting on the surface and the underlying gas phase (arising, for example, from dynamic external perturbation, such as droplet impact), reaches a critical value.<sup>24</sup> This value is defined as the critical breakthrough pressure  $P_{crit}$ , *i.e.*, the maximum pressure difference that the liquid-air interface can maintain. The key result is that to achieve greater breakthrough pressure we require progressively smaller feature spacing.

## 2.1.2 Analysis of Cone Structure as a Self-stabilizing Topography and Optical Bandpass Filter

Moving beyond simple cylindrical post arrays, experiments and calculations on a wide range of surface topographies have suggested that enhanced superhydrophobicity can be obtained by high-density conical or pyramidal structures with small hemispherical caps.<sup>26</sup> Such structures promote a robust Cassie-Baxter state with higher apparent contact angles and lower hysteresis, owing to the very small liquid-solid area fraction  $f_s = \phi_s = 2\pi(1 - \cos\theta_{adv})(r/P)^2$ , where  $r$  is the radius of hemispherical top shown in Figure 2-2, (in the case of an advancing contact angle  $\theta_{adv} \geq 90^\circ$  and a square array of conical structures with hemispherical tops) as well as negligible effects of contact line pinning on the hemispherical tops of the features.<sup>26</sup>

The conical shape of the nanotextures developed in this thesis also plays an important role in providing greater resistance to loss of superhydrophobicity. The structure is self-stabilizing and the critical breakthrough pressure increases progressively as the advancing liquid meniscus penetrates into the surface texture due to the continuously decreasing spacing between each cone. This self-stabilization can be quantified by modifying the dimensionless robustness parameter introduced by Tuteja *et al.*<sup>24</sup> By considering the geometric features in Figure 2-2A that parameterize the high aspect ratio taper structures, the relevant dimensionless parameter becomes

$$T^*(z/H) = P_{crit}/P_{ref} = \pi\ell_{cap}(z/H)^{\dagger} \cos(\theta_{adv} - \varphi) / \left[ 2P \left( 1 - (\pi/4)(z/H)^{\dagger} \right) \right] \quad (2-1)$$

where  $P_{ref} = 2\gamma_{LV}/\ell_{cap}$  is the reference pressure scale for millimetric drops,  $\gamma_{LV}$  is the surface tension,  $\ell_{cap} = \sqrt{\gamma_{LV}/\rho g}$  is the capillary length,  $\rho$  is the density of the liquid,  $g$  is the gravitational constant,  $\theta_{adv}$  is the advancing contact angle of water on a flat chemically homogenous surface, and  $\varphi$  is the cone angle of the feature as shown in Figure 2-2A (see

Appendix A for derivation). The magnitude of the critical breakthrough pressure  $P_{crit}/P_{ref}$  increases as  $z/H \rightarrow 1$  and for smaller values of  $P$  (which is proportional to  $\eta^{-1}$ ).

The length scale and shape profile of the conical structure also explain the characteristics of superhydrophilic surfaces such as *Calathea Zebrina*<sup>27</sup> (Figure 2-1), which display apparent contact angles with water lower than 10 degrees (shown in the inset of Figure 2-2A), simply by changing the surface chemistry. By changing the direction of the net surface traction of the three-phase contact line on the hydrophilic conical structure, so that  $\theta_{adv} - \phi < 90^\circ$  (Figure 2-2A), the liquid meniscus is strongly imbibed into the structure with a traction force that increases as the spacing between features decreases.<sup>28</sup> Higher values of the Wenzel roughness ( $r_w$ ) and of the feature density ( $\eta$ ) in conical nanofeatures can thus also promote superhydrophilicity and progressively smaller apparent contact angles by capillary imbibition.<sup>29</sup> Condensation on such surfaces promotes formation of a continuous liquid film with strong antifogging characteristics.<sup>10, 30</sup>

In parallel to these studies of structural control of wetting properties, bio-inspired studies on the antireflective optical properties of synthetically-fabricated subwavelength structures have been carried out.<sup>31, 32</sup> Fresnel reflections occur naturally at all optical interfaces when there is a step discontinuity in refractive index, which can be thought of as an optical impedance mismatch. Structures with subwavelength tapered features, inspired by structures such as those found on the moth-eye surface (Figure 2-1), emulate an effective medium with an axially-varying refractive index, which results in adiabatic impedance matching and hence reflection suppression.<sup>15, 31</sup> Concomitantly, transmission of incident light through transparent subwavelength conical structures is enhanced over a broad range of wavelengths and incident angles.<sup>32</sup>

By analogy with the robustness such as  $A^{*24}$  measures introduced to rank and compare the resistance to wetting of different nanotexture designs, the transmission enhancing capabilities of a synthetic tapered cone structure can be expressed in terms of dimensionless design parameters that compare the structure height and period with the incident wavelength and angle. Antireflective transparent subwavelength structures behave essentially like a band-pass filter, in which the band-pass range indicates the spectral regime with suppressed Fresnel reflection.<sup>33, 34</sup> The upper and lower wavelength bounds ( $\lambda_{\max}$  and  $\lambda_{\min}$ , respectively) for this band-pass can be tailored by controlling the geometry of the structure, and can be approximated as  $\lambda_{\max} \approx 2Hn_a \cos\theta_i$  and  $\lambda_{\min} \approx P(n_s + n_a \sin\theta_i)$ , where  $n_s$  and  $n_a$  are the refractive indices of the substrate and ambient, respectively, and  $\theta_i$  is the incident angle as shown in Figure 2-2A (see Appendix C for derivation). Using this analysis we derive the following expression for the approximate normalized operating bandwidth

$$B^* = \Delta\lambda/\lambda_{\min} = (\lambda_{\max} - \lambda_{\min})/\lambda_{\min} = (H/P)(2n_a \cos\theta_i/(n_s + n_a \sin\theta_i)) - 1. \quad (2-2)$$

We use this measure as the non-dimensional optical merit function, analogous to the parameter  $T^{*24}$  that we used to characterize the wetting behavior. To enhance the transmission bandwidth  $B^*$  on nanotextured surfaces, it is again crucial to be able to fabricate subwavelength nanostructures with high aspect ratio ( $H/P \gg 1$ ) and uniformity. This conclusion is entirely consistent with the design requirements we have highlighted for controlling wetting behavior.

### 2.1.3 Critical stresses leading to fracture by bending or buckling of slender nanotexture.

As an additional benefit, such tapered cones are more resistant to mechanical instabilities associated with buckling and bending than cylindrical pillars with the same aspect ratio and volume.<sup>35</sup> However, solid mechanical analysis also suggests that very slender structures may lead to structural instabilities under sufficiently large axial or lateral loads as discussed in Section 1.5. There is thus a trade-off between the fluidic, optical and structural properties of the texture. The final aspect ratio ( $H/P \approx 5.5$ ) chosen for the nanotexture fabricated in this thesis was selected to be able to withstand the dynamic loads associated with vertical impact of typical raindrops (see the calculations in Appendix A).

Strong structural robustness against various imposed mechanical stresses is a necessary condition to preserve the optimal design of nanotexture for simultaneous control of wetting and optical properties. For practical applications under various conditions of shear or normal loading conditions (*i.e.* along the axis of the features), the slender feature of the nanotexture can be damaged through either bending or buckling fracture, depending on the magnitude and direction of loads as briefly discussed in Section 1.5. A typical such case of concern is the dynamic pressure associated with impact of raindrops. To estimate the critical lateral or axial force (or stress) on the tip of slender tapered nanocones leading to the fractures damage under consideration, the nanotexture is approximated as a truncated cone as shown in Figure 2-3.

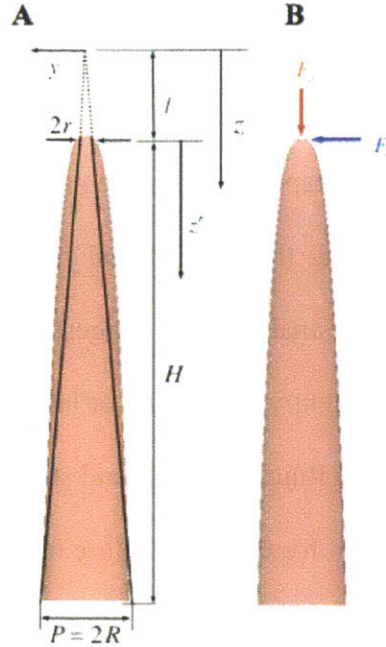


**Figure 2-3** (A) A schematic diagram (cross-sectional view) of the slender nanotaper structure. The light red shape represents approximation of the structure as a cubic paraboloid, whereas the black solid lines represent the sidewall of the truncated cone used for the analysis. (B) Lateral ( $F_l$ ) and axial forces ( $F_a$ ) acting on the tip of the nanotexture.

To calculate the amount of and location maximum tensile (normal) stress by lateral point load  $F_l$  at the tip of the truncated cone, the maximum normal stress at any cross section in the structure  $l \leq z \leq l + H$  can be written as,<sup>36</sup>

$$\sigma_n = \frac{M_z}{S_z} = \frac{F_l(z-l)}{\pi[W(z)]^3/4} \quad (2-3)$$

where  $M_z$  is the bending moment,  $S_z$  is the section modulus,  $W(z) = r + (R-r)(z-l)/H$  is the radius of cross section at distance  $z$ , and  $l$  is the distance between the virtual cone tip and actual cone tip, respectively, as shown in Figure 2-2A and 2-3.



By substituting  $z' = z - l$  and  $R - r \approx 9r$  from the values  $r \approx 10$  nm and  $R \approx 100$  nm in the design (and confirmed by measurements from the micrographs (Figure 2-2C) after fabrication) the maximum normal stress is expressed as,

$$\sigma_n = \frac{4F_l z'}{\pi [r + 9rz'/H]^3} \quad (2-4)$$

To determine the location  $z'$  where the maximum normal stress occurs, we can use the equation  $d\sigma_n/dz' = 0$ . The result is  $z' = H/18$ . By substituting the value into the above equation and using  $r \approx P/20$  (from the design  $P = 2R \approx 200$  nm), we can obtain the maximum normal stress at that point,

$$\sigma_n = \frac{16F_l H}{243\pi r^3} = \frac{16\sigma_{s, \text{rain}} H}{243r} \approx 1.32 \left( \frac{H}{P} \right) \sigma_{s, \text{rain}} \quad (2-5)$$

where the term  $\sigma_{s, \text{rain}} (= F_l/\pi r^2)$  represents the shear stress generated by raindrop impact at various impact angles on the tip of the truncated cone. We can compare the above result with the experimentally-determined typical stress needed to fracture bulk glass (which is 100 MPa and much smaller than the theoretical stress of 10 GPa necessary to break atomic bonds.<sup>37</sup>)

$$\sigma_n \approx 1.32 \left( \frac{H}{P} \right) \sigma_{s, \text{rain}} < 100 \text{ MPa} \quad (2-6)$$

Thus, the maximum value of aspect ratio  $H/P$  results in approximately 5, in consideration of  $\sigma_{s, \text{rain}} \approx 3.7$  MPa and a safety factor of 4, a typical value for the design of pressure vessels.<sup>38</sup> Note that the actual value of the radius  $W(z' = H/18)$  in the real nanotexture is greater than the radius obtained from the truncated cone approximation, which implies that the real nanostructure can resist even more lateral force than the computed value. In addition, we

note that the smooth shape of the nanostructure is closed to the cubic paraboloid shape of a fully stressed beam that attains a constant normal stress at every point  $z'$ .<sup>36</sup>

For computing the axial point load on the top of slender tapered nanocones, the approach used in a previous study for the calculation of critical buckling loads<sup>35</sup> is adopted. The governing equation Eq. 2-7 for buckling of truncated cone can be converted into a Bessel differential equation Eq. 2-9 by changing  $z$  into  $t = 1/z$ , as follows.

$$EI_r \left( \frac{z}{l} \right)^4 \frac{d^2 y}{dz^2} = -F_a y \quad (2-7)$$

$$\frac{d^2 y}{dt^2} + \frac{2}{t} \frac{dy}{dt} + \frac{F_a l^4}{EI_r} y = 0 \quad (2-8)$$

$$\frac{d^2 y}{dx^2} + \frac{2p+1}{x} \frac{dy}{dx} + \left( \frac{\alpha^2 x^{2r} + \beta^2}{x^2} \right) y = 0 \quad (2-9)$$

where  $F_a$  is the axial load on the axis of truncated cone,  $y$  is the lateral distance from the center of virtual cone tip as shown in Figure 2-3,  $E$  is the Young's modulus of the cone material from which the cone is fabricated,  $I_r$  is the moment of inertia of the top side of truncated cone.

The solution of this differential equation can be obtained as

$$y = x^{-p} \left[ C_1 J_{q/r} \left( \frac{\alpha}{r} x^r \right) + C_2 Y_{q/r} \left( \frac{\alpha}{r} x^r \right) \right] \quad (2-10)$$

$$y = t^{-\frac{1}{2}} \left[ C_1 J_{\frac{1}{2}} \left( \frac{F_a l^4}{EI_r} t \right) + C_2 Y_{\frac{1}{2}} \left( \frac{F_a l^4}{EI_r} t \right) \right] \quad (2-11)$$

where  $p = 1/2$ ,  $r = 1$ ,  $\beta = 0$ ,  $q = 1/2$ , and  $\alpha^2 = F_a l^4 / EI_r$ . And  $J_{\frac{1}{2}}(\alpha t)$  and  $Y_{\frac{1}{2}}(\alpha t)$  are the Bessel functions of the first and second kind, of the order of  $1/2$ , respectively. These Bessel functions are asymptotically expressed as

$$Y_\nu(x) = \frac{J_\nu(x) \cos \nu\pi - J_{-\nu}(x)}{\sin \nu\pi} \quad (2-12)$$

$$Y_{\frac{1}{2}}(\alpha t) = -J_{-\frac{1}{2}}(\alpha t) = \sqrt{\frac{2}{\pi\alpha t}} \cos \alpha t \quad (2-13)$$

$$J_{\frac{1}{2}}(\alpha t) = \sqrt{\frac{2}{\pi\alpha t}} \sin \alpha t \quad (2-14)$$

$$y = \frac{1}{t} \sqrt{\frac{2}{\pi\alpha}} [C_1 \sin \alpha t + C_2 \cos \alpha t] \quad (2-15)$$

We can obtain the following final form of the solution for buckling of truncated cone, by substituting  $t = 1/z$  into Eq. 2-15 as

$$y = z \left[ A \sin \frac{\alpha}{z} + B \cos \frac{\alpha}{z} \right] \quad (2-16)$$

Once we obtain the value of  $\alpha$  from the boundary conditions, we can compute the critical buckling pressure  $P_{crit} \equiv F_a / \pi r^2$  at the tip of truncated cone. The two boundary conditions are as follows.

$$y = 0 \text{ at } z = l \quad (2-17)$$

$$\frac{dy}{dz} = 0 \text{ at } z = l + H \quad (2-18)$$

leading to

$$\tan \frac{\alpha}{l} = -\frac{B}{A} \quad (2-19)$$

$$\tan \frac{\alpha}{l+H} = \frac{\frac{\alpha}{l+H} A - B}{A + \frac{\alpha}{l+H} B} = \frac{\frac{\alpha}{l+H} - \frac{B}{A}}{1 + \frac{\alpha}{l+H} \frac{B}{A}} = \frac{\frac{\alpha}{l+H} + \tan \frac{\alpha}{l}}{1 - \frac{\alpha}{l+H} \tan \frac{\alpha}{l}} \quad (2-20)$$

To calculate the value of  $\alpha$ , we substitute  $\varepsilon = \alpha/(l+H)$  and  $(l+H)/l = 12$  from the values determined by bending analysis and re-write Eq. 2-20 as

$$\tan \varepsilon = \frac{\varepsilon + \tan 12\varepsilon}{1 - \varepsilon \tan 12\varepsilon} \quad (2-21)$$

From the values of  $x$  at the intersection of the two graphs  $y=x$  and  $y = (\tan x - \tan 12x)/(1 + \tan x \tan 12x)$ , we find  $\varepsilon \approx 0.26, 0.53, \dots$ . We select the smallest value and substitute into  $\alpha = \varepsilon(l+H)$  to find  $\alpha \approx 0.31 \times 10^{-6}$  because we are interested in the smallest critical axial force.

Recalling the relation between  $\alpha$  and the axial force,

$$\alpha^2 = \frac{F_a l^4}{EI_r} = P_{crit} \left( \frac{16l^2}{E} \right) \left( \frac{l+H}{P} \right)^2 \quad (2-22)$$

we can re-write the equation for the critical buckling pressure  $P_{crit}$  as

$$P_{crit} = (9.6 \times 10^{-14}) \frac{E}{16l^2} \left( \frac{l+H}{P} \right)^{-2} \quad (2-23)$$

The value of  $P_{crit}$  should be greater than the maximum value of dynamic pressure by raindrop impact and this inequality leads to

$$\frac{l+H}{P} < \left( \frac{16l^2}{9.6 \times 10^{-14}} \right) \sqrt{\frac{E}{P_{rain}}} \quad (2-24)$$

The resultant inequality 2-24 in consideration of  $(l+H)/P \approx 6$ ,  $l \approx 10^{-7}$  m, and  $\sqrt{E/P_{rain}} \sim 10^2$  shows that the highest aspect ratio truncated cone structure determined by the critical lateral load leading bending is strong enough to prevent buckling with the same safety factor used in the analysis of bending loads.

## 2.2 Experimental Methods

### 2.2.1 Fabrication of Tapered Nanocone Surfaces

For the fabrication of nanotextured surfaces, each of the thicknesses of the multiple coated layers on a 6 inch ultraviolet (UV) grade double-side-polished fused silica wafer (thickness = 550  $\mu\text{m}$ ) was optimized for interference lithography (Figure 2-4A). Polysilicon films (240 nm) were deposited on both sides of the fused silica wafer with a chemical vapor deposition technique for realizing a high aspect ratio silicon oxide structures. Photoresist (S1813,

ShIPLEY, 4  $\mu\text{m}$ ) was spun onto both sides of the polysilicon layers of the fused silica wafer as a protective layer, and the wafer was cut into 4 samples of size 45 mm  $\times$  45 mm. The photoresist on the top of the polysilicon was cleaned with N-Methylpyrrolidone (NMP, positive resist stripper, BASF) and RCA cleaning for 20 minutes, and was sonicated for 5 minutes at room temperature. Hydrogen silsesquioxane (HSQ14, Dow Corning, 340 nm) films were then spun on both sides of the sample and hard-baked at 500°C in the oven for 11 hours to be cured as the first hardmask, because a cured HSQ layer is similar to SiO<sub>2</sub> etch mask layer.

After RCA cleaning, sonication, and plasma oxygen etching for 30 seconds in order to remove organic particulates, an antireflective coating layer (I-con 7, Brewer Science, 105 nm) was spun on the both sides and baked at 180°C in the oven for 1 hour. For baking, an oven was used instead of a hot plate, because both sides of the sample need to be protected equally. A positive photoresist (PFI-88A2, Sumitomo, 250 nm) was spun on only one side of the sample, while the photoresist (S1813, Shipley, 4  $\mu\text{m}$ ) was spun on top of the backside of the sample as a protective layer. This was then baked on the hot plate at 180°C for 90 seconds. Using Lloyd's mirror, a  $\lambda = 325$  nm wavelength laser beam makes an interference pattern with a 200 nm period standing wave projected onto the photoresist.<sup>39, 40</sup> Two separate orthogonal laser exposures (each exposure dose = 21.35 mJ/cm<sup>2</sup>) projected onto the photoresist at the incident angle of 54.34° for 5 minutes each, with an interval time of one minute (to avoid burning of the photoresist) and the exposed photoresist is developed to leave a pattern of posts (Figure 2-4B).

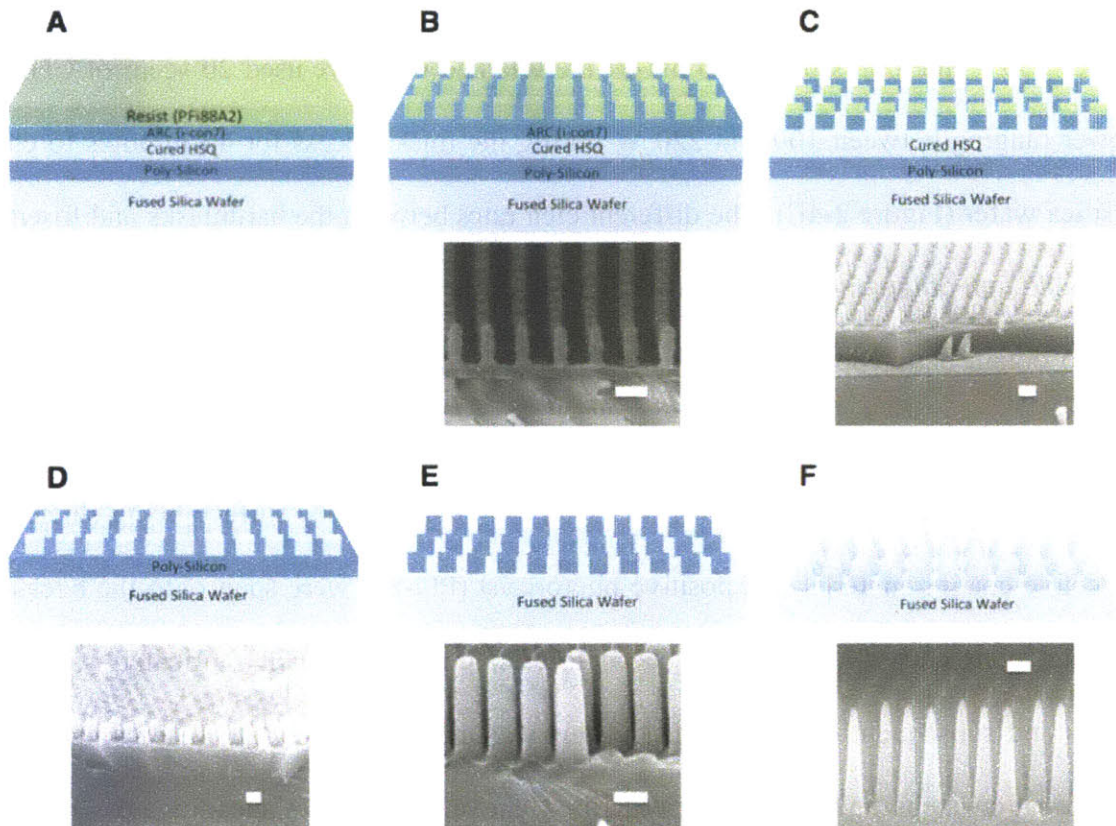


**Figure 2-4** Stages of the fabrication process. (A) Deposition of multiple coating layers. (B) Development of photoresist pattern. (C-F) Subsequent etching steps of antireflective coating layer (C), cured HSQ layer (D), polysilicon layer (E), and fused silica wafer (F). All the white scale bars on the micrographs represent 200 nm.

Oxygen and  $\text{CHF}_3$  reactive ion etching processes were used to remove the residual photoresist and open the polysilicon surface from cured HSQ. We kept the pressure at 7 mTorr and a microwave power level of 100W and used 20 sccm of oxygen plasma etching for 45 seconds (Figure 2-4C) to etch the antireflective coating layer. Then we used 20 sccm of  $\text{CHF}_3$  at a voltage of 350 V and the pressure at 10 mTorr with the power ranging between 100 and 170 W during the etch for 14 minutes in order to etch the cured HSQ layer (Figure 2-4D). The cured HSQ pattern was transferred without defect to the polysilicon layers (240 nm) with HBr reactive ion etching. For etching of polysilicon layer, we used 20 sccm of HBr for 6 minutes, keeping the

pressure at 10 mTorr and a microwave power level of 200 W during the process. Finally, a voltage of 350V and a pressure of 10 mTorr are retained while we used 20 sccm of CHF<sub>3</sub> with the power ranging between 100 and 220 W during the final process for 40 minutes to etch the fused silica wafer (Figure 2-4E). The different etch rates between the hardmasks and fused silica enable realization of the high aspect ratios (Figure 2-4F).

To obtain better optical performance, the fused silica must be patterned on both sides. Additional repeatable processes were conducted as described below. After 40 minutes of RCA cleaning, the photoresist (S1813, 4 μm) was spun onto the patterned surface being shielded. An antireflective coating material and positive photoresist (PFI-88) were spun onto the backside of the sample, consecutively. A pattern of photoresist posts was again fabricated with double exposures and subsequent development, and this was transferred down to fused silica with the same fabrication steps and conditions described above. After RCA cleaning, the rest of the polysilicon layers was removed by tetramethylammonium hydroxide (TMAH) etching (25 wt%) for 1 minute at 80°C without influencing the fabricated fused silica nanostructures on both sides.

### 2.2.2 Vapor-phase Low Surface Energy Coating

To make the surface hydrophobic, the surface was then treated by a chemical vapor deposition of 1H,1H,2H,2H-perfluorodecyltrichlorosilane<sup>41</sup> (Alfa Aesar, 96%) in an oven at 110°C for 10 hr.

### 2.2.3 Contact Angle Measurements

Advancing and receding contact angle measurements were performed using a Ramé-Hart model 590 goniometer, by dispensing liquid droplets of volume  $V = 5\mu\ell$  and adding volume to



the droplets at the flow rate of  $1 \mu\ell/s$ . Roll-off angles were measured by using an automatic tilting stage at a rate of  $1^\circ/s$ .

## 2.2.4 Optical Transmission Measurements

Optical transmission measurements were carried out using two optical measurement systems. A Cari-500 (UV-VIS-NIR) spectrophotometer was used for the polarization-dependent transmission measurements in the UV-VIS-NIR range (250-1700 nm) with a Glan-Taylor polarizer (PGT-S1V). A stabilized helium–neon laser (632.8 nm) was used to measure the transmission-incident angle with a 20LP-VIS-B Precision Linear Polarizer. The angular resolution of the instruments was  $0.07^\circ$ .

## 2.3 Results and Discussion

### 2.3.1 Superhydrophobicity/superhydrophilicity of Nanocone Structure

To simultaneously meet our fluidic and optical design requirements, we fabricated slender tapered cone structures with cone angle  $\varphi_{avg} \approx 4.8^\circ$ , on a periodic spacing  $P \approx 200$  nm and height  $H = 1.1 \pm 0.05 \mu\text{m}$  with tip radius of curvature  $r = 17 \pm 4$  nm directly on a fused silica substrate as shown in Figure 2-2B. The aspect ratio  $H/P \approx 5.5$  yields dimensionless design parameter values of  $T^* \sim 10^4$  and  $B^* \approx 6.3$  at incident angle  $\theta_i = 0^\circ$  (see Eq. 2-1 and 2-2, Figure 2-2A). Our choice of fused silica as the substrate material ensures enhanced transmission at visible and infrared wavelengths, by contrast, previous studies have reported lower bandwidth

measures ( $1.4 \leq B^* \leq 3.0$ ) on subwavelength antireflection structures,<sup>32, 42</sup> or have been based on absorptive materials (*e.g.*, silicon, gallium arsenide, carbon nanotubes, *etc.*) which suppress surface reflection but do not enhance transmission.<sup>15, 31</sup>

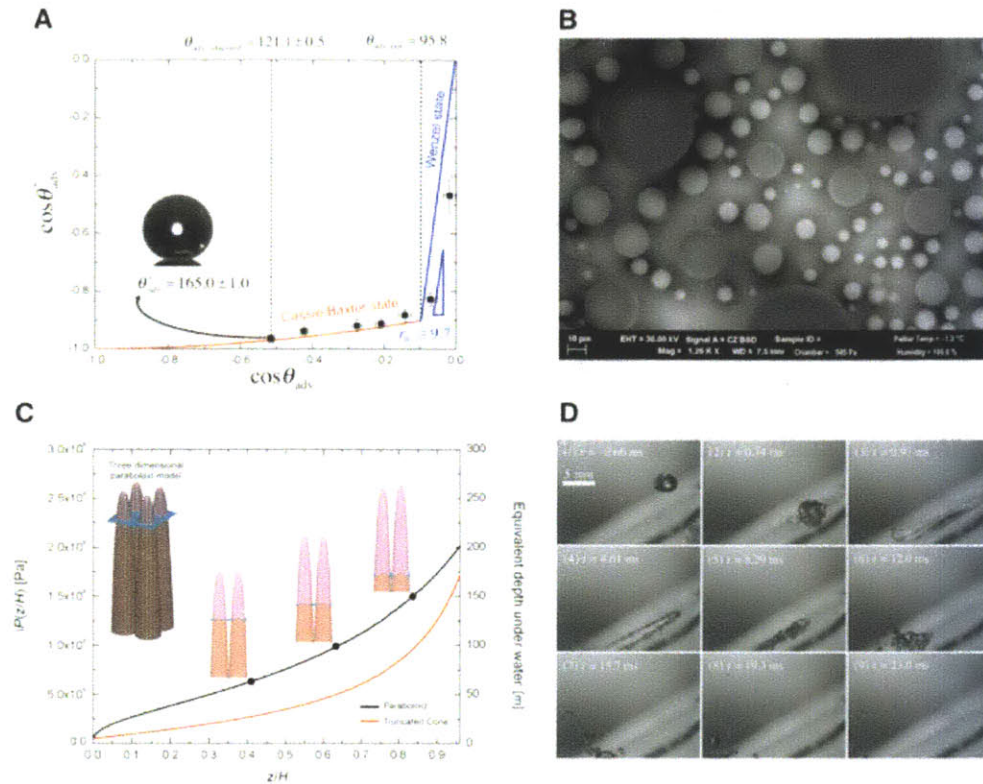


**Figure 2-5** Extreme wetting properties of the nanocone structure. (A) Wetting diagram with experimental results obtained using droplets of water-ethanol mixtures with various compositions sitting on silane-treated flat ( $\theta_{adv}$ ) and tapered nanocone ( $\theta_{adv}^*$ ) surfaces. The inset represents a pure water droplet sitting on the silanized nanotaper surface (bottom left). (B) Environmental scanning electron microscope images of condensing water drops on the silanized nanocone surface showing spherical droplets resting on the tips of the nanotaper surface. (C) Calculation of the pressure difference  $\Delta P(z/H)$  that the water-air interface can resist at given penetration depths into the structure, based on the simple analytic scaling of the dimensionless robustness parameter ( $T^*$ , Eq. 2-1) (D) Sequential images of a water droplet impact on an oblique ( $30^\circ$  from the horizontal plane) nanotaper surface (taken through the use of a high speed camera;  $V_{imp} \approx 6.26$  m/s and  $We \approx 1785$ ). The last image on the bottom right side shows that no residual droplets remain on the nanotaper surface due to the high robustness of the Cassie-Baxter state to the high dynamic pressure of the impacting drop.

The high aspect ratio nanostructures have subwavelength spacing ( $P < \lambda$ ) and were patterned over a large area ( $> 1600 \text{ mm}^2$ ) of the substrate using two orthogonal interference lithography exposures to yield a defect-free periodic square array. Structural superhydrophilicity can be readily attained from the inherent hydrophilicity of the untreated silicon oxide surface. The final fabricated superhydrophobic and transparent anti-reflective surface enables a millimetric water droplet (dyed blue in Figure 2-2C) to form an almost perfect spherical bead (apparent advancing contact angle  $\theta_{adv}^* = 165 \pm 1^\circ$ , apparent receding contact angle  $\theta_{rec}^* = 164 \pm 1^\circ$ , and roll-off angle  $\theta_{roll-off}^* \leq 2^\circ$ ).

We represent the relationship between the apparent advancing contact angle  $\theta_{adv}^*$  on the nanotextured surface (ordinate) and the advancing contact angle on a flat surface (abscissa) on a wetting diagram (see Figure 2-5A).<sup>43</sup> The red and blue lines indicate the thermodynamically-stable Wenzel state or Cassie-Baxter state, respectively.<sup>43</sup> The cross-over point at  $\theta_{crit}$  can be calculated by equating the energies for the two distinct wetting states.<sup>10, 28</sup> Advancing contact angles above this value lead to a lower overall free energy for droplets in the Cassie-Baxter state as compared to the corresponding Wenzel state.<sup>28</sup> Contact angle measurements using a range of water-ethanol mixtures possessing different surface tensions ( $47.2 \text{ mN/m} \leq \gamma_{LV} \leq 72.0 \text{ mN/m}$ ), and different advancing contact angles  $\theta_{adv}$  on flat silanized silica glass wafers confirm the predictions of the two models for the evolution in the apparent advancing contact angle observed on the silanized nanotextured surface.

To quantify the robustness of the macroscopic non-wetting behavior of these surfaces, we investigate nucleation and condensation phenomena *in situ* using an environmental scanning electron microscope (ESEM, Zeiss Evo 55). The micrograph in Figure 2-5B demonstrates that the nanotexture supports a non-wetting Cassie-Baxter state with microscopic spherical droplets.

The maximum sustainable pressure difference for this surface can be estimated to be  $\Delta P = 2\gamma_{LV}/r_d \approx 96 \text{ kPa}$ , where  $r_d = 1.5 \text{ }\mu\text{m}$  is the radius of the smallest droplet observable.

In addition to quantifying the capillary hydrostatics of droplets at rest on the nanotextured surface, the hydrodynamic interactions of impacting rain droplets with textured solid surfaces is an important design feature for robust superhydrophobic surfaces deployed in the environment. The weak shock generated by the impact of a droplet on a rigid impenetrable surface can generate dynamic pressures that are much higher than the static Laplace pressure.<sup>44</sup> The initial impact generates a water hammer pressure ( $P_{WH} \sim 0.5\rho cV$ ) where  $\rho$  is the density of water,  $c$  is speed of sound in water and  $V$  is impact velocity, respectively, which decays rapidly (see Appendix A for a time scale related to water hammer pressure) to a Bernoulli pressure ( $P_B \sim \rho V^2$ ).<sup>45-47</sup> Under these dynamic conditions even apparently-robust textured nonwetting surfaces can lose their superhydrophobicity.<sup>48</sup> For example, while typical micrometric textured post arrays can support breakthrough pressure on the order of 1 kPa,<sup>11</sup> the maximum dynamic impact pressure of raindrops with typical impact velocities in the range of  $0.3 \text{ m/s} \leq V \leq 5 \text{ m/s}$ ,<sup>47</sup> is approximately one thousand times higher, corresponding to pressure differences in the range of  $0.23 \text{ MPa} \leq P_{WH} \leq 3.8 \text{ MPa}$ . As a result of the progressively decreasing length scale between neighboring high aspect ratio asperities, the high-density tapered conical structure exhibits extremely high breakthrough pressures corresponding to several MPa as shown in Figure 2-5C. Evaluation of our modified design parameter  $T^*$  (Eq. 2-1) provides a simple analytic expression for the maximum pressure (assuming the liquid meniscus between four asperities forms a hemispherical liquid cap)  $P_{crit} = T^*(z/H \rightarrow 1) \cdot P_{ref} \approx 2.3 \text{ MPa}$ . This estimate is supported by more complete numerical calculations using Surface Evolver<sup>50</sup> (see Appendix B) which show that the critical breakthrough pressure monotonically increases as the

three-phase contact line advances into the valleys between the tapered cone. These exceedingly high values of critical breakthrough pressure and the concomitant self-stabilization effect stem from the tapered conical structure which results in the minimum spacing on the order of tens of nanometers near the bottom of each valley. The sequence of high-speed camera (Vision Research Phantom v5.0) images shown in Figure 2-5D following impact of a water drop ( $V \approx 6.26$  m/s, corresponding to Weber number  $We \approx 1785$ ) clearly shows the consequences of this self-stabilization effect, with complete droplet rebound and roll-off at higher impact velocities than previous dynamic studies.<sup>11, 48, 49</sup>

### 2.3.2 Broadband Omnidirectional Transmission and Solar Irradiance

The slender tapered nanocone structures also exhibit enhanced optical transmissivity. In Figure 2-6A and B we show the measured transmission for a flat fused silica surface and for single-sided and double-sided nanotexture surfaces. The measurements were carried out over a wide range of incident angles from  $0^\circ$  to  $80^\circ$  using both TE-polarized and TM-polarized irradiation with a wavelength  $\lambda = 632.8$  nm and the measured transmission data agree well with theoretical calculations by rigorous coupled wave analysis (RCWA, see Appendix C).

As shown in Figure 2-6A, the measured transmission of TE-polarized light through the double-sided nanotextured surface was enhanced to be above 90% even for incident angles as large as  $75^\circ$  thanks to the high aspect ratio and slow taper; by contrast the transmission of flat glass drops to 38%. For the single-sided nanocone surface the transmission is limited by Fresnel reflection arising from the step discontinuity in refractive index at the flat rear surface.

The measured transmission values of TM-polarized light through the single and double-sided nanotaper surfaces are greater than 90% at 70° as shown in Figure 2-6B. The double-sided nanotextured surface has slightly lower measured transmission than the single-sided surfaces from 40° to 70° due to the accumulation of defects induced during the sequential fabrication of nanocone arrays on both sides of the substrate, and the transmission shows no Brewster peak since there is no step discontinuity in the refractive index.<sup>51</sup> The single-sided surface, on the other hand, still exhibits the Brewster effect on the rear surface, and the transmission increases up to 99.4% at 56°.

The transmission measurements through the double-sided surfaces were also carried out over a broad range of wavelength ( $250 \text{ nm} \leq \lambda \leq 1700 \text{ nm}$ ) using TE-polarized and TM-polarized irradiation at incident angles  $\theta_i = 0^\circ, 30^\circ, 45^\circ, 60^\circ$ . In Figure 2-6C and D, the double-sided surface exhibits transmission greater than 98% at  $\theta_i = 0^\circ$  over a wide range of wavelengths. The measurements show a decrease in transmission ( $\theta_i = 0^\circ$ ) at a lower wavelength bound of approximately 300 nm, because the 200 nm-period nanocone structure becomes increasingly diffractive. The transmission measurements at incident angles  $\theta_i = 30^\circ, 45^\circ$ , and  $60^\circ$  demonstrate that the minimum wavelength bound ( $\lambda_{\min}$ ) increases with increasing incident angle for both polarized lights, which typically narrows the operational bandwidth for omnidirectional transmission (see Appendix). Figure 2-7 shows the arithmetically averaged transmission of the experimental results shown in Figure 2-6C (TE-polarized light) and D (TM-polarized light).

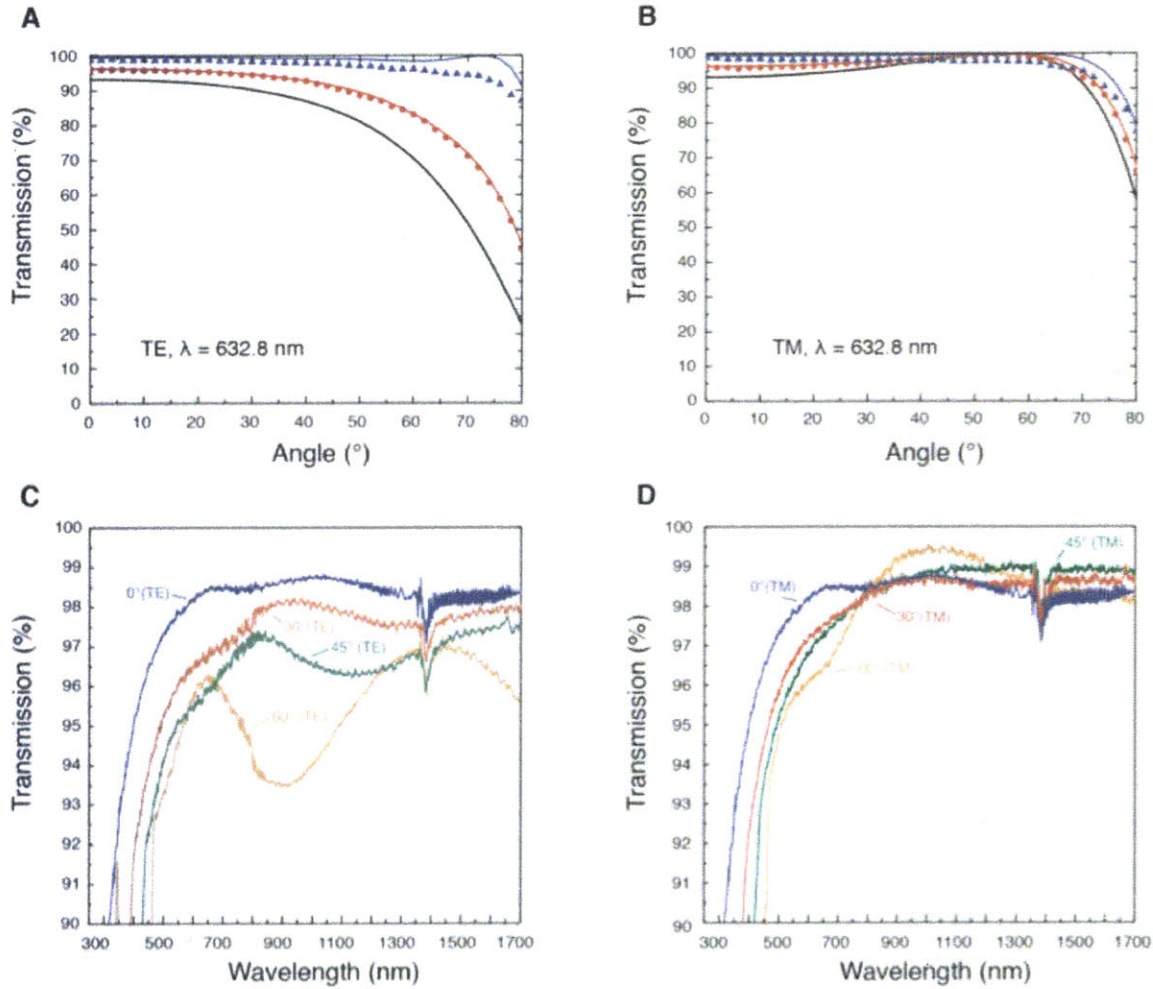


**Figure 2-6** Enhanced broadband, omnidirectional optical transmission of the nanotaper structure. (A and B) Optical transmission for both transverse electric (TE) and transverse magnetic (TM) polarized light through the single and double-sided nanotaper surfaces (represented in red circle and blue triangle, respectively) is measured by changing the incident angle of a laser source. The theoretical model results calculated by using rigorous coupled wave analysis are also shown in solid lines (flat fused silica surface in black, single-sided nanotaper surface in red, and double-sided nanotaper surface in blue) for comparison. (C and D) Measured broadband transmission for TE-polarized and TM-polarized lights at the four different incident angles with a wide range of wavelength.

To quantify the effectiveness of the nanocone surface for possible application as an outer protective layer for photovoltaic cells, we define a spectrally averaged transmittance

$$S(\theta_i) = \int_{\lambda_a}^{\lambda_b} S_r(\lambda) \cdot T(\lambda, \theta_i) d\lambda / \int_{\lambda_a}^{\lambda_b} S_r(\lambda) d\lambda, \text{ which yields the power collection efficiency if}$$

multiplied by the quantum efficiency. Here  $S_r(\lambda)$  is the spectral solar irradiance at sea level (Figure 2-7),<sup>52</sup> and  $T(\lambda, \theta_i)$  is the arithmetically averaged transmission of the surfaces as a function of wavelength and incident angle. For the tapered nanocones fabricated here, the spectrally averaged transmittance  $S(\theta_i = 0^\circ, 30^\circ, 45^\circ, 60^\circ)$  from  $\lambda_a = 300$  nm to  $\lambda_b = 1100$  nm are 0.98, 0.97, 0.95, and 0.94, respectively. The invariance of these values shows that the irradiation transmitted to a solar cell covered with such a surface texture will not vary with the solar elevation angle. By contrast, a flat fused silica surface yields values  $S(\theta_i = 0^\circ, 30^\circ, 45^\circ, 60^\circ$  and from  $\lambda_a = 300$  nm to  $\lambda_b = 1100$  nm) = 0.93, 0.92, 0.91, and 0.85.

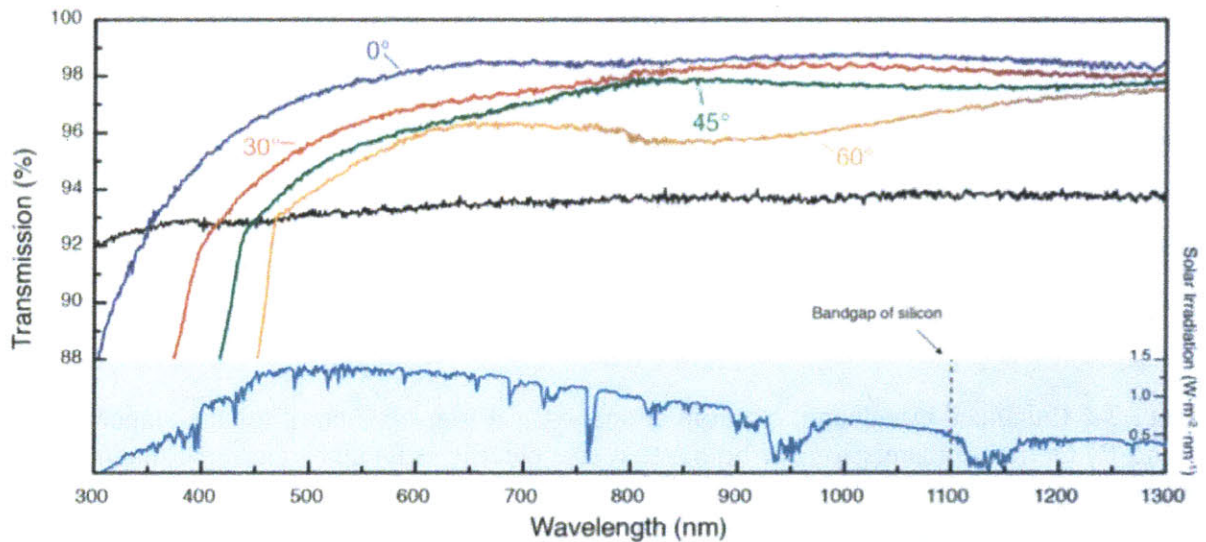


**Figure 2-7** Averaged broadband transmission with two measurements on both TE and TM polarizations in Figure 2-6 C and D at the four different incident angles with a range of wavelength ( $300 \text{ nm} \leq \lambda \leq 1300 \text{ nm}$ ). The black line is the measured broadband transmission of the flat fused silica surface at normal incident angle. Spectral solar irradiation data (light blue) with respect to the same wavelength is shown in the inset for reference, and the dashed black line depicts the band gap of crystalline silicon, one of materials used for solar cells, which means that no light can be absorbed in photovoltaic devices for wavelengths greater than this value.



### 2.3.3 Self-cleaning and Anti-fogging Effect

In many practical applications, including solar panels, self-cleaning and prevention of contaminant fouling; or avoidance of fogging are also important to preserve high transmission. These deterrents are largely mitigated in our nanotextured surfaces again due, respectively, to either superhydrophobicity or structural superhydrophilicity. To quantify, we compared changes in the transmission of the nanotextured surface and a flat silica surface after contaminant fouling using a  $\lambda = 632.8$  nm red laser at normal incidence. The transmission tests in Figure 2-8A and B show that for three different common particulate contaminants placed on the nanotextured surfaces the surfaces can be completely cleaned by at most three droplet impacts, whereas water droplets are ineffective at cleaning the conventional flat glass surfaces due to the hysteretic pinning of residual water droplets.

As shown in Figure 2-8C, a clear in-focus image of the white letters transmitted through the nanotextured surface also demonstrates qualitatively the antifogging property conferred by structural superhydrophilicity. When viewed through a conventional hydrophilic flat glass surface placed adjacently, the image is much more blurry by comparison. We quantify this difference in Figure 2-8D by measuring the time evolution of transmissivity after exposing the nanotextured and conventional surfaces to a stream of saturated steam and then placing the surfaces (at  $t = 5$  s) into the path of the laser beam. Transmission through the fogged flat glass slide rapidly drops and then gradually increases to a constant value that remains lower than that of the tapered cone surface. This loss of transmissivity on the flat hydrophilic surface is due to the deposition of microscopic droplets that remain pinned on the surface, as well as intrinsic reflection on the glass slide.<sup>53</sup> On the other hand, measurements on the double-sided nanotextured surface shows an immediate recovery of transmission to a very high plateau value

as a result of rapid imbibition of the thin layer of water followed by a uniform evaporation rate across the entire surface.

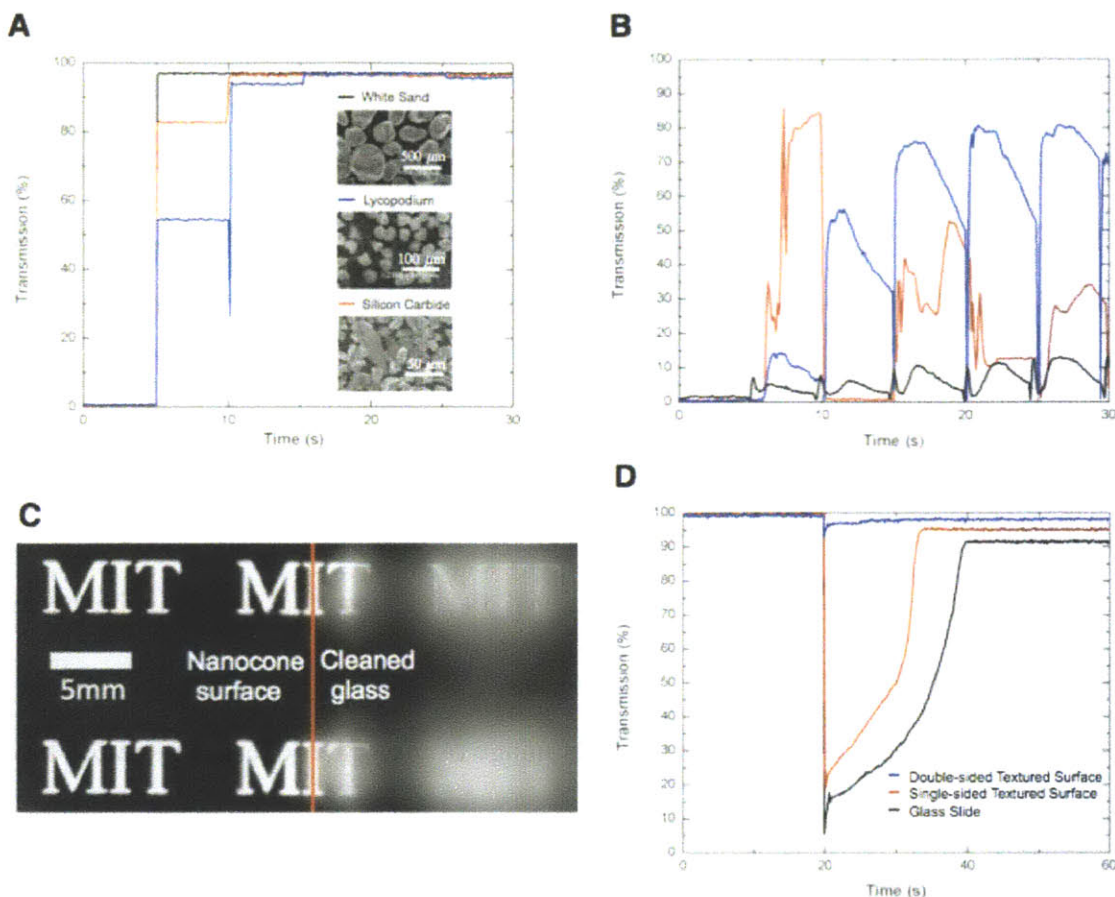


**Figure 2-8** Optical transmission measurements for quantifying the self-cleaning and anti-fogging properties of the nanocone surfaces. (A and B) Evolution of the transmission of 632.8 nm red laser through surface-contaminated tapered nanocone surface and flat glass surfaces, respectively. The transmission measurements were recorded while water droplets were released from a height of 10 mm (corresponding to impact velocity  $V \approx 0.44$  m/s;  $We = 6.9$ ) from the inclined surfaces ( $30^\circ$ ) every five seconds. The apparent contact angles ( $\theta^* > 160^\circ$ ) as well as contact angle hysteresis ( $CAH < 3^\circ$ ) of our superhydrophobic nanotextured surface remained unaltered after more than 100 realizations of the self-cleaning tests that were carried out over a period of greater than 6 months.<sup>41</sup> (C) Image of printed letters viewed through fogged (nanocone (left) and flat glass (right) surfaces. (D) Change of transmission due to fogging and defogging on double-sided nanotaper (blue), single-sided nanotaper (red) and flat cleaned glass (black) surfaces.

## 2.4 Conclusion

By developing a novel double mask etching process for large-area patterning on silicon oxide substrates, we have demonstrated that sub-wavelength tapered conical structures with high aspect ratio and large packing densities result in multi-functional surfaces with enhanced liquid wettability and omnidirectional transparency across a broad spectrum of visible and near infrared wavelengths. By combining observations of various natural textured surfaces and quantitative analysis of the underlying physical principles controlling wetting, optical transmission, and mechanical robustness, the dimension and slenderness of the nanocone structures have been optimized to achieve superior antiwetting performance and optical transmissivity. Texturing square arrays of these tapered nanocones on both sides of a flat silicon oxide substrate, followed by a suitable chemical modification of the solid surface energy, enables us to show that it is possible to combine robust superhydrophobicity (or superhydrophilicity) with minimal scattering or reflection of light over a wide range of incident angles, wavelengths and polarization states. Additional optical transmission experiments have demonstrated and quantified the macroscopic self-cleaning and anti-fogging functionalities of the nanocone structures, suggesting numerous practical engineering applications including photovoltaic cells, windshields, and goggles. Nanotextured surfaces of the type discussed in this thesis can be produced in larger scale; scanning beam interference lithography tools and large chamber plasma etchers have been employed to fabricate nanostructures over silica surfaces as large as 12-inch wafers.<sup>54</sup> Alternative methods for large-scale, low cost, high throughput manufacturing of functional nanostructures have also been described, including replication into bulk metallic glass<sup>55</sup> or through the use of roll-to-roll nanoimprinting technology with ultraviolet-curable polymers.<sup>56</sup>

Appendix A Dimensionless measure of robustness  $T^*(z/H)$  of the Cassie-Baxter state against an applied pressure difference across the water-air interfaces.

For a slender tapered cone structure, transition from the Cassie-Baxter state (See Table 2-1 for water contact angle information) to the Wenzel state is due to the application of a sufficiently-large external pressure difference across the water-air meniscus that form the composite interfaces.<sup>24</sup> Typical high aspect ratio pillar structures possessing a constant value for the critical pressure difference that the liquid meniscus can resist when the contact line is located on the vertical sidewall of pillars. By contrast the pressure difference that the nanotaper structure can support as the liquid meniscus descends along the oblique sidewall since the spacing between nearby structures becomes increasingly narrow (see Figure 2-2A). The dimensionless measure of robustness  $T^*$  compares this pressure difference as a function of penetration depth  $z/H$  into the microstructure with the reference pressure  $P_{ref} = 2\gamma_{LV}/\ell_{cap}$ , which characterizes the typical pressure difference across the liquid-air interface for millimetric-sized liquid droplets sitting at rest on the top of the posts.<sup>5</sup>

**Table 2-1** Water Contact Angle Information (at  $T = 25^\circ C$ )

Apparent Advancing Contact Angle ( $\theta_{adv}^*$ )	Apparent Receding Contact Angle ( $\theta_{rec}^*$ )	Contact Angle Hysteresis (CAH)	Roll-off Angle ( $\theta_{roll-off}^*$ )
$165 \pm 1^\circ$	$164 \pm 1^\circ$	$\leq 3^\circ$	$\leq 2^\circ$

Note that due to the high aspect ratio of the nanotaper structure and the small pitch, we can neglect the sagging of the liquid-air interface and this does not drive the wetting transition except when the meniscus is very close to the base of the structure. More accurate calculation of sagging and curvature of the liquid meniscus is provided in the next section (Appendix B).

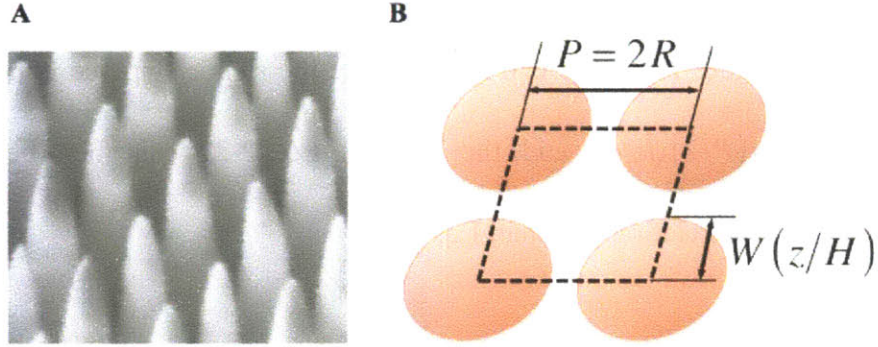


**Figure 2-9** (A) SEM micrograph of slender tapered nanocone structure. (B) A schematic diagram of horizontally cross-sectioned nanotaper structure.

The general force balance on the liquid meniscus at equilibrium equates the pressure difference across the liquid-air interface ( $\Delta P$ ) multiplied by the area with the surface tension ( $\gamma_{LV}$ ) multiplied by the total length of the contact line contained in the unit cell as shown in Figure 2-9. Assuming that (i) the contact line is on the same horizontal plane and (ii) the angle between the direction of surface tension and axis of nanotaper is  $\theta_{adv} - \varphi$  (see Figure 2-2A) at all points along the contact line, we obtain

$$\Delta P \cdot (P^2 - \pi W^2) = \gamma_{LV} \cdot (2\pi W) \cdot \cos(\theta_{adv} - \varphi) \quad (2-25)$$

where the column radius  $W$  is a function of the penetration depth  $z/H$  depending on the approximation of the shape of nanotaper structures (e.g. a truncated cone or a cubic paraboloid).

The overall force balance (Eq. 2-25) can be re-written as,

$$\Delta P = \frac{2\pi\gamma_{LV}W \cos(\theta_{adv} - \varphi)}{P^2 - \pi W^2} \quad (2-26)$$

Thus, the dimensionless robustness parameter  $T^*$  is obtained as follows.

$$T^* = \frac{\Delta P}{P_{ref}} = \frac{2\pi\gamma_{LV}W \cos(\theta_{adv} - \varphi)}{(P^2 - \pi W^2)/(2\gamma_{LV}/\ell_{cap})} = \frac{\pi \ell_{cap} (W/P) \cos(\theta_{adv} - \varphi)}{P [1 - \pi (W/P)^2]} \quad (2-27)$$

Finally, from Figure 2-2B, we can approximate the slender tapered cone structure as a cubic paraboloid,  $W = (P/2)\sqrt[3]{z/H}$  and the formula Eq. 2-27 can then be re-written by substituting the paraboloid relation to obtain Eq. 2-1

$$T^*(z/H) = \frac{\pi \ell_{cap} (z/H)^{\frac{1}{3}} \cos(\theta_{adv} - \varphi)}{2P [1 - (\pi/4)(z/H)^{\frac{2}{3}}]}$$

This above dimensionless parameter provides a measure of how robust the Cassie-Baxter state is when the contact line is located at a certain vertical position  $z/H$  and can be easily re-dimensionalized into a physical pressure difference  $\Delta P = T^* \cdot P_{ref}$ , which determines the equilibrium penetration distance of the liquid-solid-air three phase contact line into the microstructure, depending on the external pressure difference acting on the meniscus. In Figure 2-5C, the values of  $\Delta P = T^* \cdot P_{ref}$  are plotted as a function of  $z/H$ , assuming the shape of the nanotaper structure to be a cubic paraboloid or a truncated cone.

The values of  $T^*$  obtained for the nanocone structures are very large because the pitch  $P$  is only 200 nm and because the chosen scale for pressure  $P_{ref} = 2\gamma_{LV}/\ell_{cap}$  for a static liquid droplet is very small. If desired, this dimensionless group can also be rescaled by selecting an alternate (larger) scale for the characteristic pressure encountered during the dynamic events such as droplet impact. For example, if the Bernoulli pressure scale  $P_b \sim \frac{1}{2}\rho V^2$  is selected as the characteristic scale then the dimensionless robustness can be rescaled to give

$$\tilde{T} = \frac{\Delta P}{P_b} = T^* \frac{P_{ref}}{P_b} = T^* \frac{4\gamma_{LV}}{\rho V^2 \ell_{cap}} \quad (2-28)$$

The magnitude of the dimensionless value of  $T^*$  is thus reduced by a scaling factor that is essentially the Weber number  $We = 2\rho V^2 \ell_{cap} / \gamma_{LV}$  of a droplet of typical size  $\ell_{cap}$ . This can be as large as  $We \sim 10^3$  for droplet impact studies on these surfaces.

It is important to note that simulations show that the dynamic pressure decays very rapidly to half of its peak value before the meniscus reaches the bottom of conical nanostructure ( $H \approx 1100$  nm). This is because of the very short time scale of generation and attenuation of water hammer pressure associated with the high speed of sound in water and the small dimensions of the droplet.<sup>45, 46</sup> To compare the time scale for the penetration of the liquid meniscus into the structure and evolution of dynamic pressure, we introduce a time scale for the generation of water hammer pressure, which is

$$t_{WH} \sim Ma^2 R/V, \quad (2-29)$$

where  $Ma$  is the Mach number and  $R$  is the radius of impacting liquid droplet.<sup>45</sup> The time scale for the attenuation to half of water hammer pressure was also shown to be the same order of magnitude by numerical calculation.<sup>46</sup> For example, when a millimetric water droplet impacts on the nanotextured surfaces ( $V \sim 5$  m/s and  $R \sim 10^{-3}$  m), the time scale for the generation and attenuation (to half) of water hammer pressure ( $P_{WH} \approx 3.7$  MPa) near the droplet impact point is at most on the order of  $10^{-8}$  s. This time scale implies the liquid meniscus penetrates on the order of  $10^{-8}$  m if the water flow is not decelerated by the viscous shear stress on the wetted sidewalls of nanostructures.

## Appendix B A computational model to calculate the meniscus location of water-air interfaces contacting the nanotaper structures under various imposed pressure differences.

A composite liquid-air interface formed on the slender nanotaper texture becomes more robust against external pressure as the fluid meniscus approaches the base of the structure, as explained in Appendix A. However, the assumptions employed in the analytic calculation of the dimensionless robustness parameter  $T^*$  (Eq. 2-1) are no longer valid if the meniscus is very close to the base, because it is severely distorted. Hence, it is necessary to compute the exact shape of liquid-air interface to analyze the robustness of the Cassie-Baxter state using numerical techniques.<sup>57, 58</sup>

The Surface Evolver program can compute the equilibrium shape of liquid-vapor interfaces by minimizing the total free energy of the system under user-specified initial conditions and constraints.<sup>50</sup> In the Evolver input datafile, we can virtually create a part of a millimetric droplet sitting on four nanotapers, assuming the droplet size is much greater than the texture size.

A polyhedral structure incorporating a part of liquid-vapor interface (light blue), four solid-liquid interfaces (light purple), and a part of solid-vapor interface (light red) is evolved into a smoothly curved, or ‘sagging’ liquid-vapor interface connected smoothly to four neighboring nanotaper structures as the iteration proceeds (see Figure 2-10, A and B). Note that during the iterations, Young’s contact angle is preserved locally and the pressure difference acts only on the liquid-air interface (light blue). It is important to note that this distortion does not arise from gravity, but from the complex geometric shape of the solid-liquid boundary.



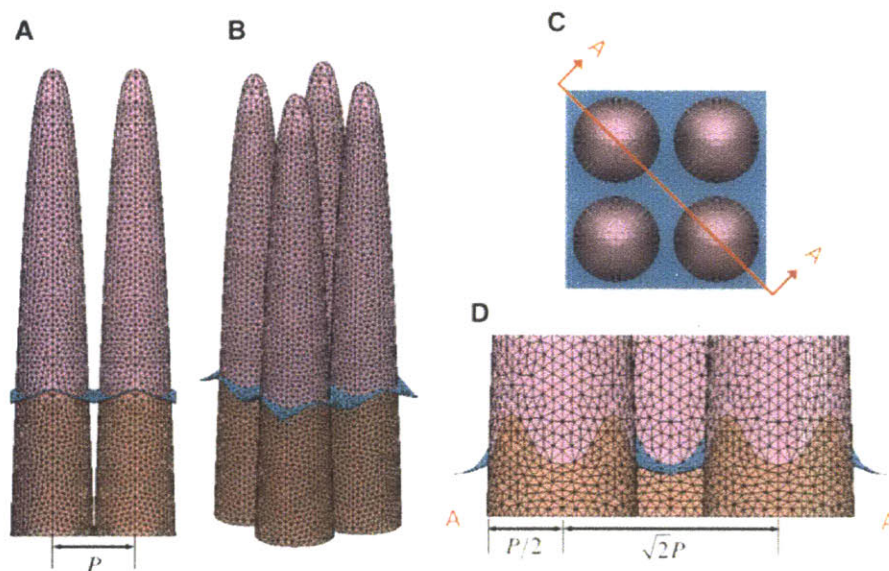


**Figure 2-10** (A-C) Side view, oblique view, and top view of the calculated equilibrium shape of the water-air interface with four neighboring nanotaper structures. Solid-liquid, solid-air, and liquid-air interfaces are represented by light purple, light red, and light blue colors, respectively. (D) A magnified side view of diagonal cross-section (A-A in C) shows the severely distorted shape of three phase contact line and the liquid-air interface.

As shown in Figure 2-5C of the main manuscript, the position of the meniscus at a given imposed pressure difference is consistent with the results from the dimensionless robustness parameter  $T^*$ . The magnified cross-sectional view (Figure 2-10D) of a meniscus located close to the base of the nanotapers clearly shows the distortion of the liquid-air interface at equilibrium. Using this computational method, we can more precisely estimate the breakthrough pressure, *i.e.*, the maximum pressure that these high-aspect ratio textured nonwetting surfaces can resist before the transition from the Cassie-Baxter state to the Wenzel state occurs, and incorporate the geometric details of the nanotextures shown in Figure 2-2B.

## Appendix C Dimensionless measure of optical transmission bandwidth for the characterization of antireflective tapered nanocone surfaces.

In this section we derive a dimensionless design parameter  $B^*$  that characterizes the bandwidth of optical transmission based on the geometry and optical properties of the nanocone structure. This factor can be used to evaluate the optical performance of any nanotextured structure as a bandpass filter and suggest optimal design of omnidirectional broadband transmissive structures. We focus on how the broadband response is affected by the structure geometry and incident angle. A diagram of the optical configuration is depicted in Figure 2-11, where light with wavelength  $\lambda$  illuminates the nanocone array (substrate index  $n_s$ ) at incident angle of  $\theta_i$ . The aspect ratio is defined as  $H/P$ , where  $H$  and  $P$  are the height and period of the nanostructure, respectively. The reflected intensity  $R_i$  at the interface between two mediums for TE-polarized light is given by the well-known Fresnel equation:

$$R_i = \left( \frac{n_a \cos \theta_i - n_b \cos \theta_t}{n_a \cos \theta_i + n_b \cos \theta_t} \right)^2 \quad (2-30)$$

The subwavelength structures described in this thesis emulate an effective medium for adiabatic impedance matching to eliminate, or reduce, this reflection.

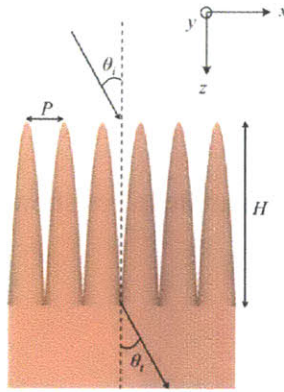


**Figure 2-11** Diagram of the structure geometry and incident light configuration.

The optical response of subwavelength antireflection structures is similar to an optical bandpass filter, where the long cutoff wavelength  $\lambda_{\max}$  is determined by the structure height  $H$ , and the short cutoff wavelength  $\lambda_{\min}$  by the structure period  $P$ .<sup>34,59</sup> Starting with the long cutoff wavelength, we observe that  $H$  and the  $z$ -component of the incident wave vector,

$$k_z = n_a \frac{2\pi}{\lambda} \cos \theta_i \quad (2-31)$$

must satisfy

$$k_z 2H > 2\pi \quad (2-32)$$

The structure height of subwavelength antireflection structures should be greater than a wavelength of incident light in the medium to ensure adiabatic impedance matching. The factor of 2 is empirically defined, and is based on RCWA theoretical simulation work.<sup>34</sup> Rearranging inequality (2-32) leads to

$$\lambda_{\max} \sim 2H n_a \cos \theta_i \quad (2-33)$$

establishing  $H$  as a scaling parameter, and predicting the maximum operating wavelength for a given  $H$ , ambient index, and incident angle. It is important to note that the maximum wavelength of this effective optical bandpass filter decreases with increasing incident angle.

On the lower bound of the bandpass filter, the structure period governs the minimum wavelength cutoff. This occurs when the structure is no longer subwavelength and becomes diffractive. To examine this effect, the wave vector for the first diffracted order is given by,

$$n_s \frac{2\pi}{\lambda} \sin \theta_{diff} = \frac{2\pi}{P} - n_a \frac{2\pi}{\lambda} \sin \theta_i \quad (2-34)$$

Setting  $\sin \theta_{diff} \rightarrow 1$  ensures the diffracted beam is evanescent, thus transferring all the energy in the specular transmitted zeroth order. Reorganizing Eq. 2-34, the minimum operating wavelength can be approximated as,<sup>34,59</sup>

$$\lambda_{min} \sim P(n_s + n_a \sin \theta_i) \quad (2-35)$$

This expression indicates that the structure period  $P$  acts as another scaling parameter, and the minimum operating wavelength increases with increasing incident angles. Figure 2-12 plots the normalized maximum and minimum operating wavelength as functions of incident angles. Therefore to yield a wider broadband response, the height of nanostructure needs to be maximized and the period of structure minimized, leading to the combined requirement of a high aspect-ratio nanocone structure.

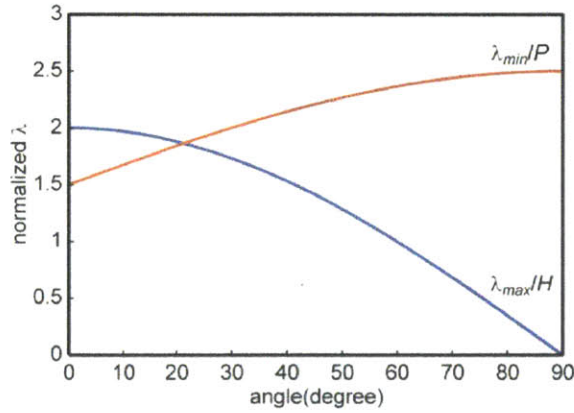


**Figure 2-12** Normalized maximum and minimum operating wavelengths plotted against incident angle.

Using equation (Eq. 2-34) and approximation (2-35), we define the normalized bandwidth as:

$$B^* = \frac{\Delta \lambda}{\lambda_{min}} = \left( \frac{H}{P} \right) \left( \frac{2n_a \cos \theta_i}{n_s + n_a \sin \theta_i} \right) - 1 \quad (2-2)$$

where  $\Delta\lambda = \lambda_{\max} - \lambda_{\min}$ . This simple relationship can be used to predict the operating bandwidth of the structure, which represents the optical parameter to maximize. Figure 2-13 depicts the normalized bandwidth vs. incident angle for various aspect ratios. As expected, higher aspect ratios lead to a larger operating bandwidth for all incident angles, whereas large incident angles lead to decreased bandwidth.

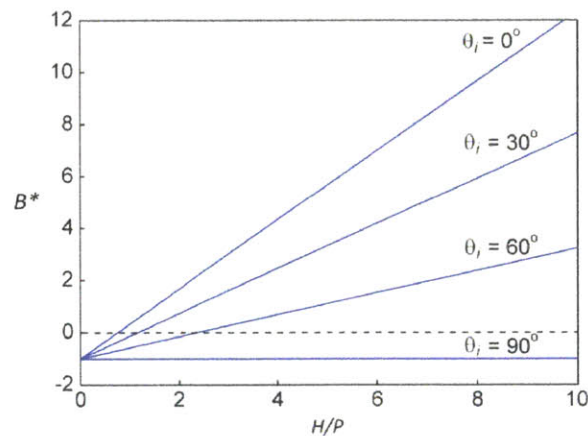


**Figure 2-13** The normalized operating bandwidth ( $B^*$ ) vs. structure aspect ratio for different incident angles. For the structure to function at large angles, high aspect ratio structures are required.

Next we validate these first-principle models by comparing them to rigorous theory. Figure 2-14 depicts the reflectivity simulated at an air/glass interface ( $n_s = 1.5$ , period  $P = 200$  nm) for incident angles of  $0^\circ$ ,  $45^\circ$ ,  $60^\circ$ , and  $70^\circ$  as a function of structure height normalized by the incident wavelength. The structure has a cubic paraboloidal profile with a square lattice, and is simulated by 20 discrete layers using rigorous coupled-wave analysis (RCWA).<sup>60, 61</sup> It can be observed that the reflectivity is effectively suppressed when the structure  $H$  is larger than the wavelength  $\lambda$ . Note the ratio  $H/\lambda_{\max}$  at different incident angle for adequate reflection suppression follows the general trend described by Eq. 2-33.

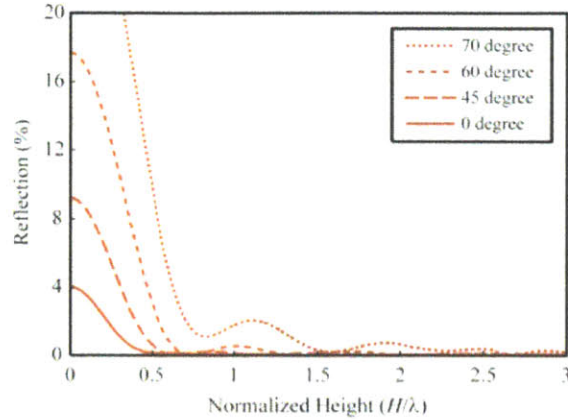


**Figure 2-14** Reflection of antireflection nanostructure simulated using RCWA for a number of incident angles as functions of normalized structure height.

The simplified model can be further tested by comparing the bandpass optical response, as shown in Figure 2-15. In this RCWA simulation the nanocone structure has  $P = 200$  nm,  $H = 800$  nm, and four incident angles,  $\theta_i = 0, 30, 45,$  and  $60^\circ$  are examined. A 99% transmission cut-off level is added to Figure 2-15, so that the operating bandwidth for each angle can be compared. Figure 2-15 shows that the operating bandwidth for each angle follows the general trend predicted by Eq. 2-2.

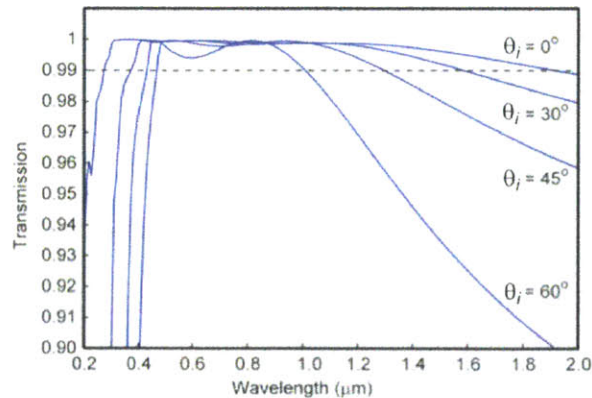


**Figure 2-15** Transmission efficiency of the antireflective nanocone structure simulated using RCWA for a number of incident angles as functions of the wavelength of the incident illumination.

## Appendix D Measurements of broadband and omnidirectional optical transmission of the double-sided nanotaper surfaces.

A Cari-500 (UV-VIS-NIR) spectrophotometer was used for the polarization-dependent transmission measurements in the UV-VIS-NIR range with the Glan-Taylor polarizer (PGT-S1V). The theoretical model results (dashed lines) shown in Figure 2-16, 17 and 18 were calculated by 20 discrete layers using two dimensional rigorous coupled wave analysis (RCWA)<sup>60,61</sup> with 121 spatial harmonics retained. The structure geometry is approximated from micrographs, and are given in Table 2-2.

**Table 2-2** The structure geometry for rigorous coupled wave analysis (RCWA). 20 discrete layers were used for defining nanotaper structures and the duty cycles of each layer are listed in the table. The period is 200 nm.

Layer	Duty cycle	Layer	Duty cycle
1 (Top layer)	0.07	11	0.58
2	0.14	12	0.61
3	0.21	13	0.64
4	0.28	14	0.67
5	0.35	15	0.71
6	0.39	16	0.75
7	0.43	17	0.79
8	0.47	18	0.84
9	0.51	19	0.89
10	0.55	20	0.94

Figure 2-16, 17, and 18 show the measured optical transmission of the surface and simulated transmission using RCWA for both transverse electric (TE) and transverse magnetic (TM) polarized lights as a function of the wavelength from 300 nm to 1700 nm at the incident angles of 30°, 45° and 60°, respectively. The measured optical transmission with TM-polarized

light is slightly higher than that with TE-polarized light because of the Brewster effect, also expected in the simulation results. In Figure 2-18, the transmission of TM-polarized light has the maximum value 99.5% at the wavelength of 1083 nm, while that of TE-polarized light has the minimum value 93.4% at the wavelength of 915 nm in the near infrared region, where the light is not diffractive. In addition, all the transmission values drop as the incident angle increases, but those are still above 90% over a wavelength region from 465 nm to 1700 nm. The RCWA simulations are in a good agreement with the experimental data on the general efficiency trend. The measured experimental data have slightly lower absolute efficiency due to defects and mechanical damage on the double-sided patterned surface. The optical transmission exhibits transmission drop at the wavelength of 1390 nm, since Si-OH band has an absorption band centered here.<sup>62</sup>

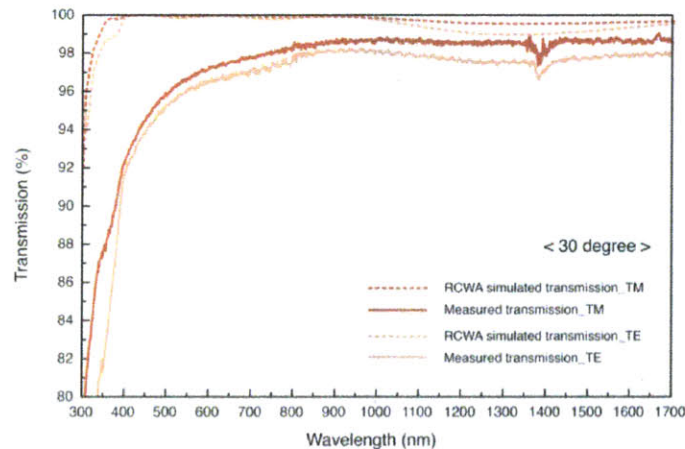


**Figure 2-16** Measured optical transmission of the nanotaper structures and simulated transmission using RCWA for both transverse electric (TE) and transverse magnetic (TM) polarized lights as a function of the wavelength at 30° incident angle.



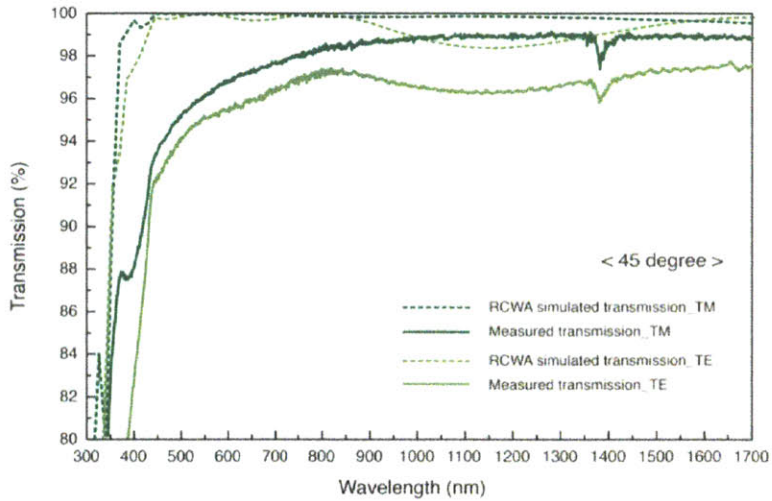


**Figure 2-17** Measured optical transmission of the nanotaper structures and simulated transmission using RCWA for both TE and TM-polarized lights as a function of the wavelength at 45° incident angle.

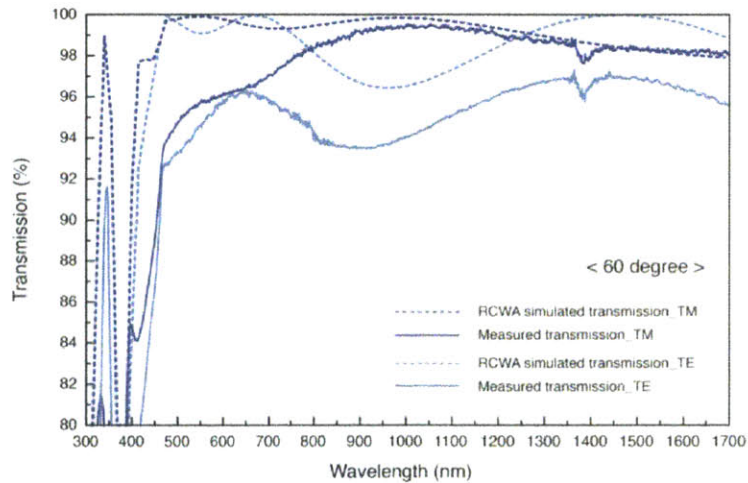


**Figure 2-18** Measured optical transmission of the nanotaper structures and simulated transmission using RCWA for both TE and TM-polarized lights as a function of the wavelength at 60° incident angle.

## References

1. Barthlott, W.; Neinhuis, C. Purity of the Sacred Lotus, or Escape from Contamination in Biological Surfaces. *Planta* **1997**, *202*, 1-8.
2. Clapham, P. B.; Hutley, M. C. Reduction of Lens Reflection by Moth Eye Principle. *Nature* **1973**, *244*, 281-282.
3. Hamilton, W. J.; Seely, M. K. Fog Basking by the Namib Desert Beetle, *Onymacris Unguicularis*. *Nature* **1976**, *262*, 284-285.
4. Wenzel, R. N. Resistance of Solid Surfaces to Wetting by Water. *Ind. Eng. Chem.* **1936**, *28*, 988-994.
5. Cassie, A. B. D.; Baxter, S. Wettability of Porous Surfaces. *Trans. Faraday Soc.* **1944**, *40*, 0546-0550.
6. Parker, A. R.; Lawrence, C. R. Water Capture by a Desert Beetle. *Nature* **2001**, *414*, 33-34.
7. Wilson, S. J.; Hutley, M. C. The Optical Properties of "Moth Eye" Antireflection Surfaces. *Opt. Acta* **1982**, *29*, 993-1009.
8. Parker, A. R.; Townley, H. E. Biomimetics of Photonic Nanostructures. *Nat. Nanotechnol.* **2007**, *2*, 347-353.
9. Lafuma, A.; Quéré, D. Superhydrophobic States. *Nat. Mater.* **2003**, *2*, 457-460.
10. Quéré, D. Wetting and Roughness. *Annu. Rev. Mater. Res.* **2008**, *38*, 71-99.
11. Bhushan, B.; Jung, Y. C.; Koch, K. Micro-, Nano- and Hierarchical Structures for Superhydrophobicity, Self Cleaning, and Low Adhesion. *Philos. Trans. R. Soc., A* **2009**, *367*, 1631-1672.
12. Lau, K. K. S.; Bico, J.; Teo, K. B. K.; Chhowalla, M.; Amaratunga, G. A. J.; Milne, W. I.; McKinley, G. H.; Gleason, K. K. Superhydrophobic Carbon Nanotube Forests. *Nano Lett.* **2003**, *3*, 1701-1705.
13. Ahuja, A.; Taylor, J. A.; Lifton, V.; Sidorenko, A. A.; Salamon, T. R.; Lobaton, E. J.; Kolodner, P.; Krupenkin, T. N. Nanonails: A Simple Geometrical Approach to Electrically Tunable Superhydrophobic Surfaces. *Langmuir* **2008**, *24*, 9-14.
14. Bernard, C. G. Structural and Functional Adaptation in a Visual System. *Endeavour* **1967**, *26*, 79-84.
15. Kanamori, Y.; Sasaki, M.; Hane, K. Broadband Antireflection Gratings Fabricated Upon Silicon Substrates. *Opt. Lett.* **1999**, *24*, 1422-1424.
16. Lalanne, P.; Morris, G. M. Antireflection Behavior of Silicon Subwavelength Periodic Structures for Visible Light. *Nanotechnology* **1997**, *8*, 53-56.

17. Barnes, G. A.; Flaim, T. D.; Jones, S. F.; Bruce, J.; Dudley, W.; Koester, D. A.; Peters, C. R.; Bobbio, S. M. Antireflective Coating for Deep Uv Lithography Process Enhancement. *Polym. Eng. Sci.* **1992**, *32*, 1578-1582.
18. Xie, G.; Zhang, G.; Lin, F.; Zhang, J.; Liu, Z.; Mu, S. The Fabrication of Subwavelength Anti-Reflective Nanostructures Using a Bio-Template. *Nanotechnology* **2008**, *19*, 095605.
19. Xia, F.; Jiang, L. Bio-Inspired, Smart, Multiscale Interfacial Materials. *Adv. Mater.* **2008**, *20*, 2842-2858.
20. Min, W.-L.; Jiang, B.; Jiang, P. Bioinspired Self-Cleaning Antireflection Coatings. *Adv. Mater.* **2008**, *20*, 3914-3918.
21. Zhu, J.; Hsu, C. M.; Yu, Z. F.; Fan, S. H.; Cui, Y. Nanodome Solar Cells with Efficient Light Management and Self-Cleaning. *Nano Lett.* **2010**, *10*, 1979-1984.
22. Lee, H. J.; Willis, C. Dressed for Combat. *Chem. Ind. (London, U. K.)* **2009**, 21-23.
23. Gao, X.; Yan, X.; Xu, L.; Zhang, K.; Zhang, J.; Yang, B.; Jiang, L. The Dry-Style Antifogging Properties of Mosquito Compound Eyes and Artificial Analogues Prepared by Soft Lithography. *Adv. Mater.* **2007**, *19*, 2213-2217.
24. Tuteja, A.; Choi, W.; Mabry, J. M.; McKinley, G. H.; Cohen, R. E. Robust Omniphobic Surfaces. *Proc. Natl. Acad. Sci. U. S. A.* **2008**, *105*, 18200-5.
25. Journet, C.; Moulinet, S.; Ybert, C.; Purcell, S. T.; Bocquet, L. Contact Angle Measurements on Superhydrophobic Carbon Nanotube Forests: Effect of Fluid Pressure. *Europhys. Lett.* **2005**, *71*, 104-109.
26. Nosonovsky, M., Bhushan, B. Roughness Optimization for Biomimetic Superhydrophobic Surfaces. *Microsyst. Technol.* **2005**, *11*, 535-549.
27. Schulte, A. J.; Koch, K.; Spaeth, M.; Barthlott, W. Biomimetic Replicas: Transfer of Complex Architectures with Different Optical Properties from Plant Surfaces on Technical Materials. *Acta Biomater.* **2009**, *5*, 1848-1854.
28. Tuteja, A.; Choi, W.; McKinley, G. H.; Cohen, R. E.; Rubner, M. F. Design Parameters for Superhydrophobicity and Superoleophobicity. *MRS Bull.* **2008**, *33*, 752-758.
29. Reyssat, M.; Courbin, L.; Reyssat, E.; Stone, H. A. Imbibition in Geometries with Axial Variations. *J. Fluid Mech.* **2008**, *615*, 335-344.
30. Cebeci, F. C.; Wu, Z. Z.; Zhai, L.; Cohen, R. E.; Rubner, M. F. Nanoporosity-Driven Superhydrophilicity: A Means to Create Multifunctional Antifogging Coatings. *Langmuir* **2006**, *22*, 2856-2862.
31. Huang, Y.-F.; Chattopadhyay, S.; Jen, Y.-J.; Peng, C.-Y.; Liu, T.-A.; Hsu, Y.-K.; Pan, C.-L.; Lo, H.-C.; Hsu, C.-H.; Chang, Y.-H.; *et al.* Improved Broadband and Quasi-Omnidirectional Anti-Reflection Properties with Biomimetic Silicon Nanostructures. *Nat. Nanotechnol.* **2007**, *2*, 770-774.

32. Choi, K.; Park, S. H.; Song, Y. M.; Lee, Y. T.; Hwangbo, C. K.; Yang, H.; Lee, H. S. Nano-Tailoring the Surface Structure for the Monolithic High-Performance Antireflection Polymer Film. *Adv. Mater.* **2010**, *22*, 3713-3718.
33. Deinega, A.; Valuev, I.; Potapkin, B.; Lozovik, Y. Minimizing Light Reflection from Dielectric Textured Surfaces. *J. Opt. Soc. Am. A* **2011**, *28*, 770-777.
34. Grann, E. B.; Moharam, M. G.; Pommet, D. A. Optimal Design for Antireflection Tapered Two Dimensional Subwavelength Grating Structure. *J. Opt. Soc. Am. A* **1995**, *12*, 333-339.
35. Timoshenko, S. P.; Gere, J. M. *Theory of Elastic Stability*. McGraw-Hill: New York, 1961.
36. Gere, J. M. *Mechanics of materials*. Brooks/Cole, 2001.
37. Griffith, A. A. The Phenomena of Rupture and Flow in Solids. *Philos. Trans. R. Soc., A* **1921**, *221*, 163-198.
38. Korobkin, A. A. Asymptotic Theory of Liquid-Solid Impact. *Philos. Trans. R. Soc., A* **1997**, *355*, 507-522.
39. Fujita, S.; Maruno, S.; Watanabe, H.; Kusumi, Y.; Ichikawa, M. Periodical Nanostructure Fabrication Using Electron Interference Fringes Produced by Scanning Interference Electron Microscope, *Appl. Phys. Lett.* **1995**, *66*, 2754-2756.
40. Lasagni, A.; Seyler, M.; Holzapfel, C.; Maier, W.; Mücklich, F. Periodical Gratings in Mixed Oxide Films by Laser Interference Irradiation, *Adv. Mater.* **2005**, *17*, 2228-2232.
41. Kobrin, B.; Zhang, T.; Grimes, M. T.; Chong, K.; Wanebo, M.; Chinn, J.; Nowak, R. An Improved Chemical Resistance and Mechanical Durability of Hydrophobic FDTD Coatings, *J. Phys.: Conf. Ser.* **2006**, *34*, 454-457.
42. Li, Y.; Zhang, J.; Zhu, S.; Dong, H.; Jia, F.; Wang, Z.; Tang, Y.; Zhang, L.; Zhang, S.; Yang, B. Bioinspired Silica Surfaces with near-Infrared Improved Transmittance and Superhydrophobicity by Colloidal Lithography. *Langmuir* **2010**, *26*, 9842-9847.
43. Onda, T.; Shibuichi, S.; Satoh, N.; Tsujii, K. Super-Water-Repellent Fractal Surfaces. *Langmuir* **1996**, *12*, 2125-2127.
44. Eggers, J.; Fontelos, M. A.; Josserand, C.; Zaleski, S. Drop Dynamics after Impact on a Solid Wall: Theory and Simulations. *Phys. Fluids* **2010**, *22*, 062101.
45. Lesser, M. Analytic Solutions of Liquid-Drop Impact Problems. *Proc. R. Soc. A* **1981**, *377*, 289-308.
46. Rosenblatt, M.; Ito, Y. M.; Eggum, G. E. Analysis of Brittle Target Fracture from a Subsonic Water Drop Impact. In *Erosion: Prevention and Useful Applications*; Adler, W. F., Ed. American Society for Testing and Materials: 1979; pp 227-254.
47. Sanada, T.; Ando, K.; Colonius, T. In *Numerical Analysis of High Speed Droplet Impact*, 7th Intl. Conf. on Multiphase Flow, Tampa, FL, May 30-June 4; 2010.

48. Li, X.; Ma, X.; Lan, Z. Dynamic Behavior of the Water Droplet Impact on a Textured Hydrophobic/Superhydrophobic Surface: The Effect of the Remaining Liquid Film Arising on the Pillars' Tops on the Contact Time. *Langmuir* **2009**, *26*, 4831-4838.
49. Zorba, V.; Stratakis, E.; Barberoglou, M.; Spanakis, E.; Panagiotis, T.; Anastasiadis, S. H.; Fotakis, C. Biomimetic Artificial Surfaces Quantitatively Reproduce the Water Repellency of a Lotus Leaf. *Adv. Mater.* **2008**, *20*, 4049-4054.
50. Brakke, K. A. The Surface Evolver. *Experimental Mathematics* **1992**, *1*, 141-165.
51. Chuang, S.-Y.; Chen, H.-L.; Shieh, J.; Lin, C.-H.; Cheng, C.-C.; Liu, H.-W.; Yu, C.-C. Nanoscale of Biomimetic Moth Eye Structures Exhibiting Inverse Polarization Phenomena at the Brewster Angle. *Nanoscale* **2010**, *2*, 799-805.
52. *Standard Terrestrial Direct Normal Solar Spectral Irradiance Tables for Air Mass 1.5*. American Society for Testing of Materials: Philadelphia, PA, 1982.
53. Srinivasarao, M.; Collings, D.; Philips, A.; Patel, S. Three-Dimensionally Ordered Array of Air Bubbles in a Polymer Film. *Science* **2001**, *292*, 79-83.
54. Heilmann, R.; Chen, C.; Konkola, P.; Schattenburg, M. Dimensional Metrology for Nanometre-scale Science and Engineering: Towards Sub-nanometre Accurate Encoders, *Nanotechnology*. **2004**, *15*, S504-S511.
55. Schroers, J. Processing of Bulk Metallic Glass, *Adv. Mater.* **2009**, *22*, 1566-1597.
56. Kim, J.-G.; Sim, Y.; Cho, Y.; Seo, J.-W.; Kwon, S.; Park, J.-W.; Choi, H.; Kim, H.; Lee, S. Large Area Pattern Replication by Nanoimprint Lithography for LCD-TFT Application, *Microelectron. Eng.* **2009**, *86*, 2427-2431.
57. Lobaton, E. J.; Salamon, T. R. Computation of Constant Mean Curvature Surfaces: Application to the Gas-Liquid Interface of a Pressurized Fluid on a Superhydrophobic Surface. *J. Colloid Interface Sci.* **2007**, *314*, 184-198.
58. Zheng, Q.-S.; Yu, Y.; Zhao, Z.-H. Effects of Hydraulic Pressure on the Stability and Transition of Wetting Modes of Superhydrophobic Surfaces. *Langmuir* **2005**, *21*, 12207-12212.
59. Grann, E. B.; Moharam, M. G. Comparison between Continuous and Discrete Subwavelength Grating Structures for Antireflection Surfaces. *J. Opt. Soc. Am. A* **1996**, *13*, 988-992.
60. Moharam, M. G.; Grann, E. B.; Pommet, D. A.; Gaylord, T. K. Formulation for Stable and Efficient Implementation of the Rigorous Coupled-Wave Analysis of Binary Gratings. *J. Opt. Soc. Am. A* **1995**, *12*, 1068-1076.
61. Moharam, M. G.; Pommet, D. A.; Grann, E. B.; Gaylord, T. K. Stable Implementation of the Rigorous Coupled-Wave Analysis for Surface-Relief Gratings: Enhanced Transmittance Matrix Approach. *J. Opt. Soc. Am. A*, **1995**, *12*, 1077-1086.

62. Toh, K.; Shikama, T.; Nagata, S.; Tsuchiya, B.; Suzuki, T.; Okamoto, K.; Shamoto, N.; Yamauchi, M.; Nishitani, T. Optical Characteristics of Aluminum Coated Fused Silica Core Fibers under 14 MeV Fusion Neutron Irradiation. *J. Nucl. Mater.* **2004**, 329, 1495-1498.

## **CHAPTER 3**

### **3. Effect of Surface Texturing on Superoleophobicity, Contact Angle Hysteresis, and “Robustness”**

Reproduced with permission from

Zhao, H.; Park, K.-C.; Law, K.-Y. Effect of Surface Texturing on Superoleophobicity, Contact Angle Hysteresis, and “Robustness”. *Langmuir*, **2012**, *28*, 14925-14934.

Copyright 2012 American Chemical Society.

## 3.1 Introduction and Theory

### 3.1.1 General Introduction

Printing engines are basically electromechanical devices that put marks of toner and ink on paper. Traditionally, both engine design and print process development are based on optimization of the electromechanical properties. Relatively less attention has been paid to the property of the printing surface. As it turns out, contamination of the printing surface has been a critical issue. The usual countermeasure is to install a cleaner to clean the contamination. This approach is effective, but adds cost and complexity to the engine design. As our demands on performance, cost and sustainability increase, there is a need for future engines to be smaller, simpler with lower cost. Inspired by the Lotus effect,<sup>1-4</sup> we thought that printing surface with self-cleaning ability would radically improve the performance of future engines. Concurrently, we also recognized that surfaces with superhydrophobicity are unlikely to succeed, as most superhydrophobic surfaces are superoleophilic<sup>5</sup> and they will have a high affinity towards toner and ink. As a result, our working target has been surfaces that are non-sticking and exhibit high repellency towards toner and ink.<sup>6-8</sup> Our ultimate goal is to make a surface that is mechanically strong and superoleophobic where toner and ink will be repelled upon contact.

Earlier, we<sup>6</sup> reported the fabrication of a model superoleophobic surface comprising  $\sim 3$   $\mu\text{m}$  diameter pillar arrays (6  $\mu\text{m}$  pitch with  $\sim 7$   $\mu\text{m}$  height) on silicon wafer. The surface texture was made by the conventional photolithographic technique, followed by modifying the chemistry of the textured surface with a fluorosilane. Both static and dynamic contact angle measurement techniques were used to characterize the surface and found that the surface is both



superhydrophobic and superoleophobic with water and hexadecane contact angles exceeding  $150^\circ$  and sliding angles at  $\sim 10^\circ$  (Figure 3-1).

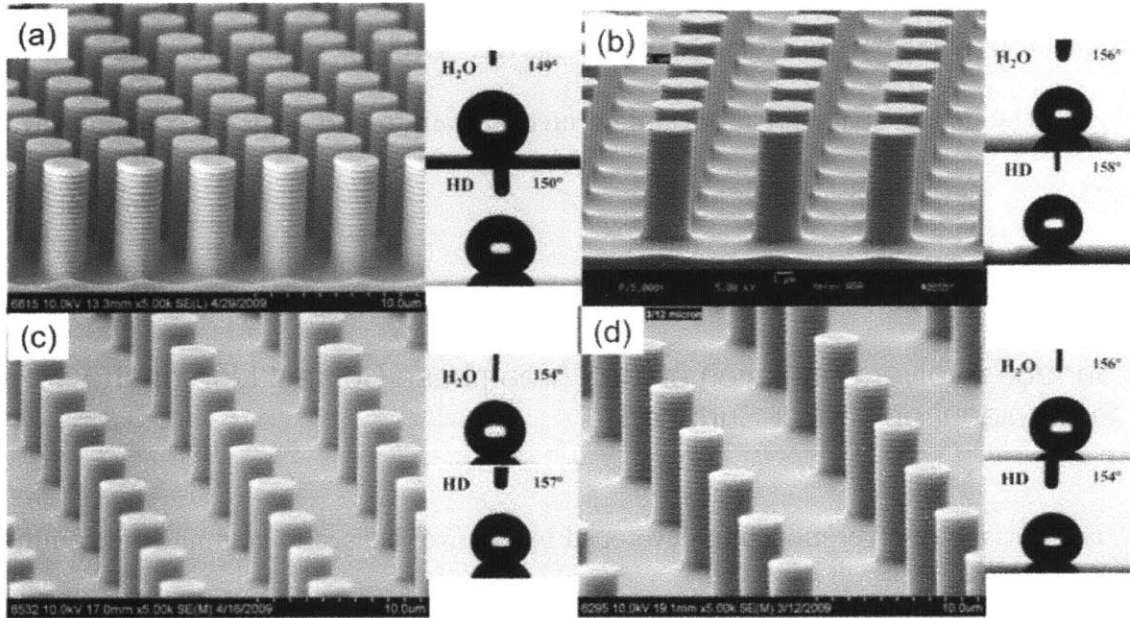


**Figure 3-1** SEM micrographs of  $\sim 3 \mu\text{m}$  diameter pillar array surfaces coated with fluoroocetyl trichlorosilane (FOTS) layer, with (a)  $4.5 \mu\text{m}$ , (b)  $6 \mu\text{m}$ , (c)  $9 \mu\text{m}$ , and (d)  $12 \mu\text{m}$  center-to-center spacing. (Insets: sessile drops of water and hexadecane on the pillar array surfaces)

Systematic investigation revealed that both surface fluorination and the re-entrant structure in the side wall of the pillar is crucial in achieving the superoleophobicity. Our conclusion suggested that both water and oil (hexadecane) are in the Cassie-Baxter state, “sitting” on air in the composite solid-liquid interface. This conclusion was confirmed by microscopy where we were able to make a replica of the interface by first placing a molten drop of hot polyethylene wax on the surface followed by examining the composite interface by SEM (after cooling).<sup>6</sup> In this thesis, we study the effects of pillar spacing, diameter and height on the surface properties. Results show that these structural parameters have very little effect on the

static and advancing contact angles for both water and hexadecane. On the other hand, pillar spacing has profound effects on the dynamic contact angles, particularly the sliding angle, the receding contact angle and the contact angle hysteresis. The importance of contact line pinning is discussed. The robustness of the pillar array surface against wetting breakthrough pressure and mechanical abrasion are assessed using Surface Evolver simulation<sup>9</sup> and mechanical modeling.<sup>10</sup> The design space for fabricating a mechanically robust, superoleophobic surface is discussed.

### 3.1.2 Surface Evolver Simulation of the Three-phase Contact Line on the Superoleophobic Pillar Surface

The Surface Evolver modeling developed by Brakke<sup>9</sup> is used to compute the equilibrium shape of the liquid-vapor interfaces by minimizing various energies of the interfaces under user-specified initial condition and constraints. In this thesis, we employ it to (1) simulate the location of the liquid-solid-vapor three phase contact line on the re-entrant structure, (2) depict the sagging curvature of the liquid-vapor interface, and (3) estimate the robustness of various re-entrant structures by increasing the pressure constraints, i.e. identifying the breakthrough pressure for transition from the Cassie-Baxter state to the Wenzel state.

The superoleophobic surface<sup>6</sup> with the wavy side wall has now been modeled using Surface Evolver to pin point the location of the three-phase contact line of hexadecane along the side wall in the pillar structure. A pillar with the wavy side wall is mathematically created by combining a formula describing a cylinder and a sinusoidal wave formula. The sagging liquid-vapor interface with the defined surface texture is shown in Figure 3-2. The modeling suggests that droplet of hexadecane would be pinned underneath the re-entrant structure of the pillar array

surface. This was validated experimentally where we were able to create a replica of the composite interface using hot polyethylene wax as the liquid and studied the morphology of the interface by SEM.<sup>6</sup>

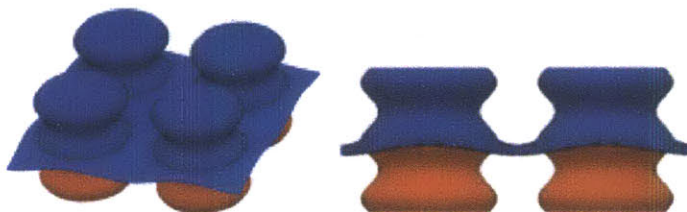


**Figure 3-2** Equilibrium shapes of sagging liquid-air interface of hexadecane on the superoleophobic pillar array FOTS surface (blue: hexadecane, red: pillar)

When an external pressure is applied to the liquid droplet on the pillar array surface, the three phase contact line propagates and starts to wet the pillar structure. Figures 3-3a and 3b show the two wetting failures,  $H^*$  and  $T^*$  as defined by Tuteja and co-workers.<sup>11</sup> As the external pressure increases, the liquid drop starts to sag and penetrate into the void space in the pillar structure.  $H^*$  describes the failure when the sagging liquid drop “touches” the bottom of the pillar structure, transitioning from the superoleophobic Cassie-Baxter state to the fully wetted Wenzel state.  $H^*$  usually occurs when the pillar height is very short. On the other hand,  $T^*$  failure is the result of de-pinning of the contact line due to the increase of capillary pressure at such a point the texture angle  $\psi$  reaches zero. The breakthrough pressure is then defined as the pressure when the liquid starts to de-pin and wet the pillar structure.

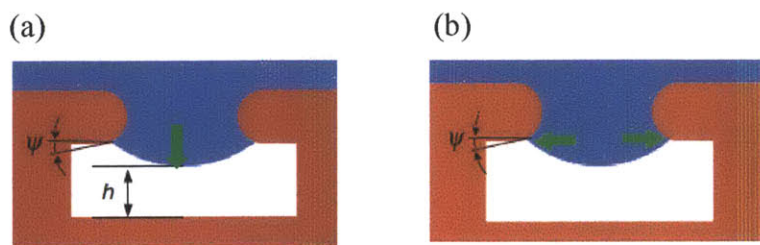


**Figure 3-3** (a)  $H^*$  failure (“touch-down” scenario) under pressure; and (b)  $T^*$  failure (“de-pinning” scenario) under pressure. (blue: hexadecane, red: pillar)

### 3.1.3 Critical Bending and Buckling Loads of Cylindrical Pillar Structures

Assuming an arbitrary force  $F_{\text{global}}$  is applied to area  $A$  on the pillar array surface with dimensions indicated in Figure 3-4, two dimensionless design parameters, bending parameter  $S^*$  and buckling parameter  $N^*$ , can be developed according to the classic solid mechanics bending theory of a circular shape beam with one fixed end and one free end.<sup>10</sup>  $S^*$  and  $N^*$  are the ratios of the maximum theoretical stress the pillars can withstand to the actual stress exerted to the pillar structure under shear and normal stress condition, respectively.

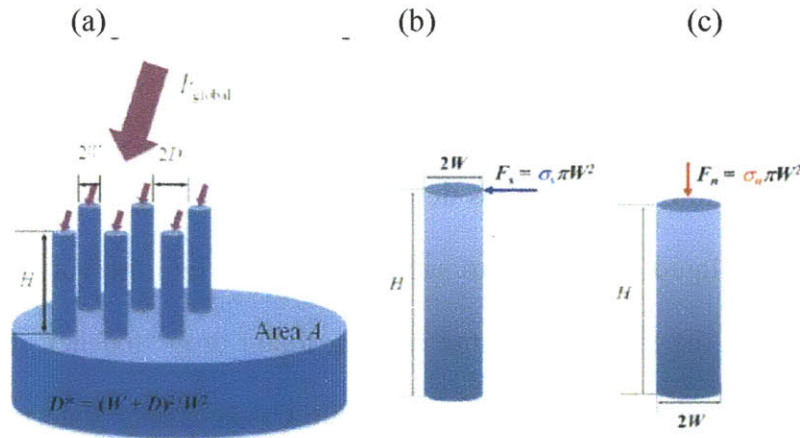


**Figure 3-4** (a) Model textured surface used to model the deformation of the pillar array surface against external force  $F_{\text{global}}$ ; (b) bending failure of a single pillar; and (c) buckling failure of a single pillar.

The bending parameter  $S^*$  is derived as follows.

$$\begin{aligned}
 S^* &= \frac{\sigma_{\text{theoretical}}}{\sigma_s} = \frac{\sqrt{E\gamma/r_0}}{F_s H / (\pi W^3 / 4)} = \frac{\sqrt{E\gamma/r_0}}{(4F_{s,\text{global}} D^* / (\pi A)) \pi W^2 H / (\pi W^3 / 4)} \\
 &= \frac{\pi}{16} \left( \frac{E\gamma}{r_0} \right)^{\frac{1}{2}} \left( \frac{F_{s,\text{global}}}{A} \right)^{-1} (D^*)^{-1} \left( \frac{H}{W} \right)^{-1}
 \end{aligned} \tag{3-1}$$

where  $E$  is Young's modulus of material composing the pillar,  $\gamma$  is surface energy of the material, and  $r_0$  is the distance between neighboring atoms,  $F_{s,\text{global}}$  is the shear force generated from  $F_{\text{global}}$ ,

A is the area, and  $D^* = (W + D)^2/W^2$ ,  $W$ ,  $D$  and  $H$  are the pillar array structural parameters as shown in Figure 3-4.

According to the definition, the pillar structure will survive the pressure when  $S^* > 1$  and the higher the  $S^*$  value, the more robust the pillar structure is mechanically. The pillar structure will have a bending failure when  $S^* < 1$ . When  $S^* = 1$ , the critical shear stress ( $F_{s,global}/A$ ) can be calculated by applying all the related properties of Silicon and the geometrical parameters of the pillar array surface.

Similarly, according to the classic solid mechanics buckling theory of a circular shape beam with one fixed end and one free end, the bending parameter  $N^*$  can be derived.<sup>10</sup>

$$\begin{aligned}
 N^* &= \frac{F_{theoretical} / (\pi W^2)}{\sigma_n} = \frac{\pi^2 EI / (4H^2) / (\pi W^2)}{F_n / (\pi W^2)} \\
 &= \frac{\pi^2 E \pi W^4 / 4 / (4H^2) / (\pi W^2)}{4F_{n,global} D^* / (\pi A)} \\
 &= \frac{\pi^3 E}{64} \left( \frac{F_{n,global}}{A} \right)^{-1} (D^*)^{-1} \left( \frac{H}{W} \right)^{-2}
 \end{aligned} \tag{3-2}$$

where  $F_{n,global}$  is the normal force generated by  $F_{global}$ . Similarly when  $N^* = 1$ , the normal stress exerted by the external force will reach the theoretical buckling stress threshold and the buckling failure will occur. Under this condition, the critical normal stress ( $F_{n,global}/A$ ) can also be calculated. For the same external force, the higher the  $N^*$  value, the more robust the pillars are against buckling.

## 3.2 Experimental Methods

### 3.2.1 Materials and Surface Texture Fabrication

All the textured surfaces studied in this thesis were fabricated on 4 inch test grade silicon wafers (Montco Silicon Technologies, Inc.) by conventional photolithographic techniques followed by surface modification with a conformal nanocoating. The lithographic mask was constructed by Photronics Inc. For the superoleophobic surface with the wavy side wall in the pillars, the texture was defined via 5:1 photolithography on Autostep 200, transferring the patterns from the mask to the photoresist (SPR700-1.2). The surface texture was then created by etching the Si-wafer using the Bosch deep reactive ion etching (DRIE) process. A slightly different process was used to fabricate textured surfaces with the overhang structure. In this case, a SiO<sub>2</sub> thin film was first deposited onto a piranha cleaned Si-wafer via plasma enhanced chemical vapor deposition (GSI PECVD). The texture structures were again defined via 5:1 photolithography using SPR700-1.2 as the photoresist. Autostep 200 (5x reduction wafer exposure tool) was used to transfer the patterns from the mask to the photoresist. Cap patterns were then transferred onto the SiO<sub>2</sub> layer using a CH<sub>3</sub>F/O<sub>2</sub> plasma reactive ion etching process (Oxford 80 RIE). The etching process was stopped when the bare silicon surface was exposed. Pillars were then etched using another fluorine etching processes (SF<sub>6</sub>/O<sub>2</sub>) and the overhang structure was enhanced by an isotropic XeF<sub>2</sub> etch. Schematics and details of the two procedures have been given elsewhere.<sup>6</sup>

### 3.2.2 Surface Modification

After the surface texture was created on the silicon wafer, it was chemically modified by a ~1.5 nm thick fluorosilane layer (FOTS), which was obtained by molecular vapor deposition of tridecafluoro-1,1,2,2-tetrahydrooctyltrichlorosilane onto the bare textured surface in a MVD100 reactor from Applied Microstructures, Inc. The fluorinated textured surface was then heat cured in an oven at ~150°C for ~30 minutes prior to the contact angle measurement.

### 3.2.3 Measurements

Static contact angle and sliding angle measurements were performed on a goniometer model OCA20 from Dataphysics. The drop size of the test liquid was controlled to be ~5  $\mu\text{L}$ . The advancing/receding contact angles were measured using the sessile drop method by adding/removing liquid to/from the existing droplet at a very small volume flow rate (0.15  $\mu\text{L}/\text{sec}$ ).<sup>12</sup> The sliding angles were measured using the tilting base unit accessory TBU 90. After dispensing a 10  $\mu\text{L}$  droplet, the stage was tilted at a rate of 1°/sec to a maximum of 90°. The sliding angle is defined as the angle where the test liquid droplet starts to move.

### 3.2.4 Modeling of Surface Wettability

The Surface Evolver method developed by Brakke<sup>9</sup> was employed to simulate (a) the position of the liquid-solid-vapor three phase contact line on different pillar array surfaces, (b) the sagging curvature of the liquid-vapor interface, and (c) the robustness of the surface

wettability against external pressure. The breakthrough pressure is defined as the pressure where transition from the composite Cassie-Baxter state to the fully wetted Wenzel state occurs. Details of the methodology have been published by Tuteja and co-workers earlier.<sup>11</sup>

### 3.3 Results and Discussion

#### 3.3.1 Effect of Pillar Spacing on Surface Properties

We employed a pillar array FOTS surface comprising  $\sim 3 \mu\text{m}$  diameter pillars with a pitch of  $\sim 6 \mu\text{m}$  on silicon wafer.<sup>6</sup> The pillar height was  $\sim 7.8 \mu\text{m}$  with a wavy side wall structure resulted from the Bosch etching process. The surface was both superhydrophobic and superoleophobic with water and hexadecane contact angles exceeding  $150^\circ$  and sliding angles at  $\sim 10^\circ$ . The superoleophobicity was attributed to both surface fluorination and the re-entrant structure in the wavy side wall of the pillar. Using hot polyethylene wax, we demonstrated experimentally that the contact line for the hydrocarbon liquid pins underneath the re-entrant structure, forming the Cassie-Baxter superoleophobic composite interface (Eq. 1-3). In this thesis, we study the location and the geometry of the solid-liquid-vapor three phase contact line for hexadecane using Surface Evolver modeling and the result confirms that hexadecane indeed pins underneath the re-entrant structure (Figure 3-2).



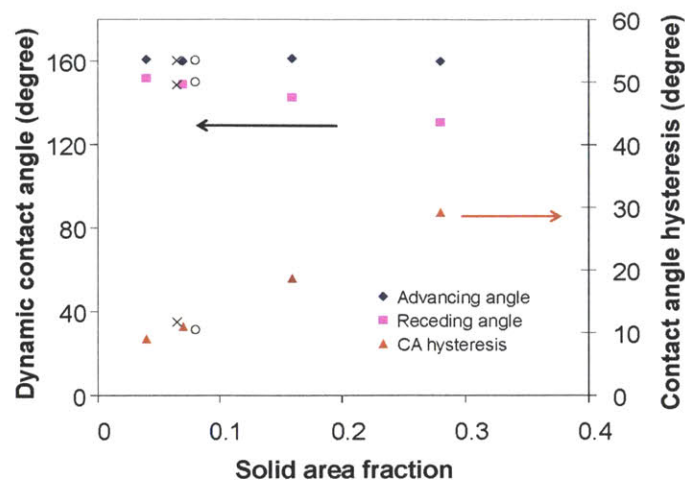


**Figure 3-5** Plot of dynamic water contact angle data versus solid area fraction for 3  $\mu\text{m}$  pillar array FOTS surfaces ( $\blacklozenge$ ,  $\blacksquare$  and  $\blacktriangle$ ). (Insert: dynamic water contact angle data from a 1  $\mu\text{m}$  pillar array (X) and a 5  $\mu\text{m}$  pillar array (O) FOTS surface)

**Table 3-1** Effect of the pillar spacing on the surface properties of 3  $\mu\text{m}$  pillar array FOTS surfaces.

Pillar diameter/pitch/height	Solid area fraction <sup>a</sup>	Testing liquids	Static contact angle <sup>b</sup>	Advancing contact angle <sup>b</sup>	Receding contact angle <sup>b</sup>	Sliding angle <sup>b</sup>
3/ 4.5/ 7.2 $\mu\text{m}$	0.28	water	149.0°	160.0°	130.8°	20.0°
		Hexadecane	150.9°	161.7°	111.1°	19.4°
3/ 6/ 7 $\mu\text{m}$	0.16	water	156.2°	161.3°	142.6°	10.1°
		Hexadecane	157.9°	161.1°	120.9°	9.8°
3/ 9/7 $\mu\text{m}$	0.07	water	154.1°	159.9°	148.9°	5.7°
		Hexadecane	157.4°	160.9°	131.6°	5.7°
3/ 12/ 7 $\mu\text{m}$	0.04	water	156.2°	160.8°	151.8°	3.4°
		Hexadecane	154.3°	161.6°	142.4°	3.7°

(a) Solid area fraction is calculated based on the actual size of the pillars measured from the SEM images, not the designed solid area fraction on the mask, (b) all measurements were averaged of >5 independent measurements and the error is 2° or better.

Figures 3-1 a-d depict the SEM micrographs of 4 different FOTS pillar array surfaces comprising 3  $\mu\text{m}$  diameter pillars (height  $\sim 7 \mu\text{m}$ ) with center-to-center spacing varying from 4.5 to 6 to 9 to 12  $\mu\text{m}$  on Si wafer. Their surface properties were studied by both static and dynamic contact angle measurement techniques and the results are summarized in Table 3-1. Photographs of the water and hexadecane sessile drops are provided in the insets of Figure 3-1. From the static contact angle results, we conclude that all four pillar array FOTS surfaces are superhydrophobic and superoleophobic with water and hexadecane contact angles at or larger than  $150^\circ$  and that varying the pillar spacing does not seem to have an effect on the static contact angle.

Contrast to the static contact angle data, there is a strong pillar spacing effect on the dynamic contact angle. Figures 3-5 and 6 plot the relationship between the advancing and receding contact angle for water and hexadecane, respectively, as a function of the solid area fraction. In this thesis, we use solid area fraction to characterize the structural parameter of the surface. For pillar array surfaces with the same pillar diameter, solid area fraction will decrease as the spacing increases. Results in Figures 3-5 and 6 indicate that although the advancing contact angle does not seem to vary with the solid area fraction, the receding angle is found to decrease as the solid area fraction increases, for both water and hexadecane. As a result, the contact angle hysteresis ( $\Delta$  between advancing and receding contact angle) increases as the solid area fraction increases. It is important to note that the contact angle hysteresis with hexadecane increases to  $\sim 50^\circ$  at solid area fraction 0.28 and is significantly larger than that with water ( $\sim 30^\circ$ ). The larger hysteresis with hexadecane can be attributed to its lower surface tension and deeper pinning on the side wall of the pillar. The advancing and receding contact angles observed in this thesis are found to be in reasonable agreement with those predicted from the

modified Cassie-Baxter equations derived by Choi and co-workers,<sup>13</sup> suggesting that the local area fraction experienced by the contact line determines the size of the advancing and receding contact angles. The solid area fraction effect on hysteresis is consistent with those reported by Choi et. al. also, the larger the solid area fraction the larger the hysteresis.

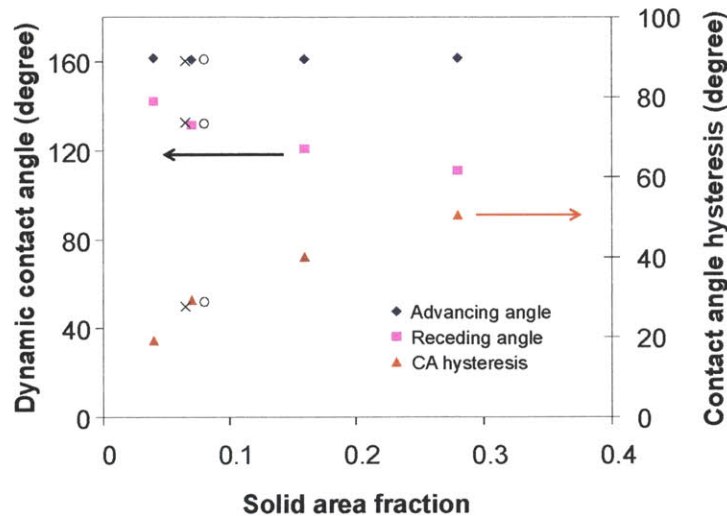


**Figure 3-6** Plot of dynamic hexadecane contact angle data versus solid area fraction for 3  $\mu\text{m}$  pillar array FOTS surfaces ( $\blacklozenge$ ,  $\blacksquare$  and  $\blacktriangle$ ). (Insert: dynamic hexadecane contact angle data from a 1  $\mu\text{m}$  pillar array (X) and a 5  $\mu\text{m}$  pillar array (O) FOTS surface)

Sliding angle is another dynamic contact angle parameter studied in this thesis. Figure 3-7 plots the effect of solid area fraction on the sliding angles for water and hexadecane. At solid area fraction 0.04, both water and hexadecane droplets are very mobile and roll off the surface at very low tilting angles (e.g.  $\sim 3\text{-}4^\circ$ ). However, the sliding angle was found to increase, from  $\sim 4^\circ$  to  $\sim 19^\circ$ , monotonously as the solid area fraction increases (to 0.28). While the trend for the increase is expected, what's surprising is the magnitude of the sliding angle at solid area fraction 0.28. The sliding angles for smooth FOTS Si-wafer surface (solid area fraction 1.0) were measured at  $\sim 13.6^\circ$  with water and  $\sim 9^\circ$  with hexadecane, respectively.<sup>6</sup> The fundamental question one may ask is, why does a textured surface with the same surface chemistry that

exhibits superhydrophobic-like and superoleophobic-like contact angle produce a larger sliding angle than that on the smooth surface? While the phenomenon is not new, it is counter intuitive. This is another example illustrating that high contact angle does not necessarily imply low sliding angle or low hysteresis.

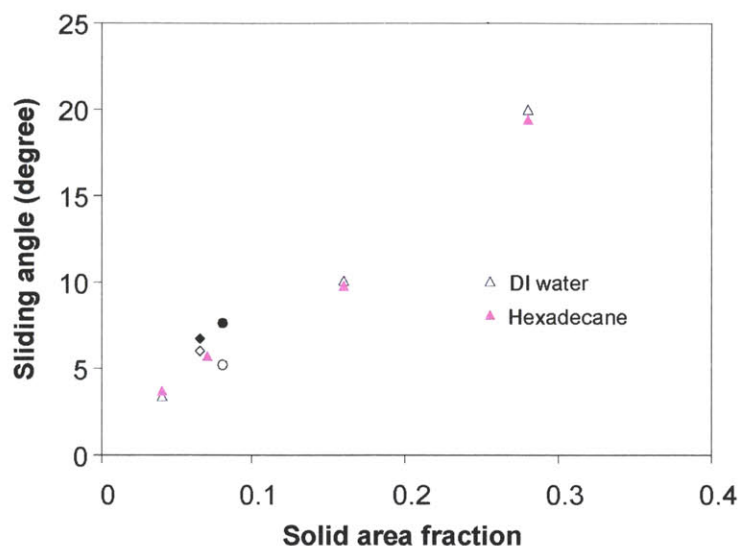


**Figure 3-7** Plot of sliding angle versus solid area fraction for water and hexadecane on 3  $\mu\text{m}$  ( $\triangle$ ,  $\blacktriangle$ ), 1  $\mu\text{m}$  ( $\diamond$ ,  $\blacklozenge$ ); and 5  $\mu\text{m}$  ( $\circ$ ,  $\bullet$ ) pillar array FOTS surfaces (water: open symbols, hexadecane: solid symbols).

Figure 3-8a depicts the liquid-solid interface for an idealized Cassie-Baxter state<sup>14</sup> where the liquid drop is sitting on the pillar array surface with no liquid penetration into the pillar structure. As described earlier, we have both experimental and modeling data to indicate that Figure 3-8a does not represent the true picture. Our overall results suggest that liquid droplets do penetrate into the void space between pillars. The actual geometry of the composite interface is better represented by Figure 3-8b, where some liquid penetration and sagging occur at the liquid-solid interface.



**Figure 3-8** Ideal and actual Cassie-Baxter state.

With that composite interface picture in mind, the large sliding angle observed for the pillar array FOTS surface at solid area fraction 0.28 relative to the smooth FOTS wafer surface can attribute to surface friction created by surface roughness as the liquid drop is sliding. For instance, since the liquid droplet does penetrate (sag) into the void space between pillars, it has to be de-pinned (or recede from the void) before sliding on the top of the pillar surface. Thus for pillar array surfaces with higher pitches (larger solid area fraction), the surface friction would increase. The gradual increase in sliding angle as the solid area fraction increases (Figure 3-7) can then be attributed to the increase in surface friction as the pitch is decreasing. In 2007, Nosonovsky<sup>15</sup> modeled the sliding friction of water droplet on similar pillar array surfaces and showed that surface adhesion and roughness are the two contributors to the sliding friction. The fact, that (1) the sliding angles for water and hexadecane are very similar and are linearly dependent of the solid area fraction, and (2) the surface adhesion of all the pillar array surfaces are actually very small, suggest that the sliding friction is dominated by the roughness of the pillar array surfaces. Indeed, in a recent study of sliding water droplet on ZnO nanorod, Sakai and co-workers<sup>16</sup> reported that the measured resistance for water sliding is linearly dependent on the solid area fraction. The surface adhesion term is insignificant. Sliding of the water droplets on microtextured (pillar) surfaces has also been studied by several other groups and they all pointed to need of de-pinning the contact line and then recede before drop sliding.<sup>17-19</sup> The solid

area fraction effect on the sliding angle observed in this thesis is therefore consistent with all earlier investigations.

Using the same mental model, the solid area fraction effect on the receding contact angle and contact angle hysteresis in Figures 3-5 and 6 can also be rationalized. For instance, as the solid area fraction increases, the density of contact line de-pinning per unit area would increase as the liquid recedes. This will result in a decrease in the receding contact angle and an increase in the contact angle hysteresis.

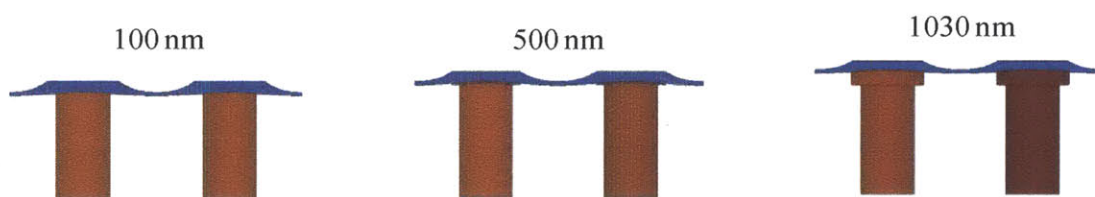


**Figure 3-9** Surface Evolver modeling of the water/FOTS pillar array interface as a function of the thickness of the overhang structure (red: pillar, blue: water)

It is also important to note that the hysteresis observed for hexadecane is about twice of that of water. As shown by Surface Evolver modeling, due to the high water contact angle on the FOTS surface ( $107^\circ$ ), water droplet actually pins on the pillar surface (see result in Figure 3-9). As for hexadecane, it wets the pillar surface and penetrates into the side wall with the contact line pinning underneath the re-entrant structure due to its low contact angle on FOTS ( $73^\circ$ ) and low surface tension (see Appendix B as well as Figure 3-10). The relatively low contact angle hysteresis observed for water is thus rationalized.

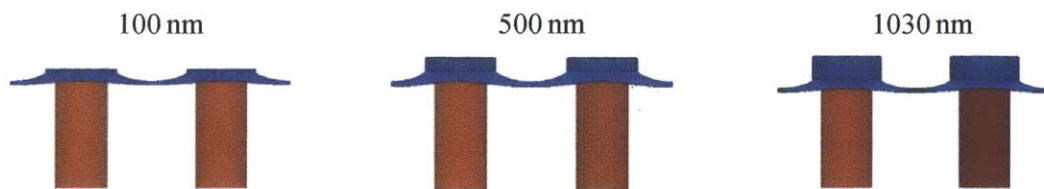


**Figure 3-10** Surface Evolver modeling of the hexadecane/FOTS pillar array interface as a function of the thickness of the overhang structure (red: pillar, blue: hexadecane)

### 3.3.2 Effect of Pillar Diameter

The effect of pillar diameter on the surface properties was studied with  $\sim 1\ \mu\text{m}$  and  $\sim 5\ \mu\text{m}$  pillar array FOTS surfaces with pillar height at  $\sim 3\ \mu\text{m}$ . As shown later, pillar height has no effect on the surface properties in this range. Figure 3-11 shows the SEM micrographs of the two pillar array surfaces. The center-to-center spacing for the  $1\ \mu\text{m}$  pillar array is  $3\ \mu\text{m}$  and that of the  $5\ \mu\text{m}$  array is  $15\ \mu\text{m}$ . Our intention here is to keep the solid area fraction of these two textured surfaces comparable to the  $3\ \mu\text{m}$  pillar array surfaces so that the diameter effect can be compared. The static and dynamic contact angles for these surfaces are measured and the data are included in Table 3-2. Despite their difference in pillar size, both pillar array surfaces are superhydrophobic and superoleophobic with similar water and hexadecane contact angles ( $\sim 150^\circ$ ) and sliding angles ( $\leq 10^\circ$ ). The sessile drop data are included in Figure 3-11.

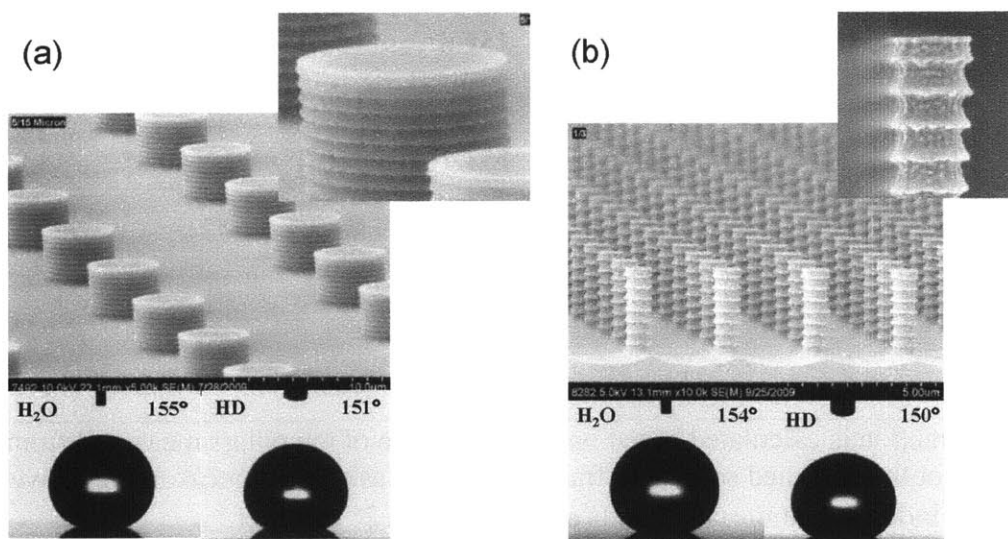


**Figure 3-11** SEM micrographs and water & hexadecane sessile drop data for (a)  $\sim 5\ \mu\text{m}$  ( $15\ \mu\text{m}$  pitch) and (b)  $\sim 1\ \mu\text{m}$  ( $3\ \mu\text{m}$  pitch) pillar array surfaces

**Table 3-2** Effect of the pillar size and pillar height on the surface properties of various pillar array FOTS surfaces.

<b>Pillar variables</b> diameter/pitch/height	Solid area fraction <sup>a</sup>	Testing liquids	Static contact angle <sup>b</sup>	Advancing contact angle <sup>b</sup>	Receding contact angle <sup>b</sup>	Sliding angle <sup>b</sup>
<b>Pillar size effect</b>						
5/ 15/ 3 $\mu\text{m}$	0.08	water	154.5°	160.4°	149.9°	5.2°
		Hexadecane	150.9°	161.0°	132.2°	7.6°
1/ 3/ 3 $\mu\text{m}$	0.08	water	154.1°	160.2°	148.5°	6.0°
		Hexadecane	150.3°	160.2°	132.6°	6.7°
<b>Pillar height effect</b>						
3/ 12/ 7 $\mu\text{m}$	0.04	water	156.2°	160.8°	151.8°	3.4°
		Hexadecane	154.3°	162.3°	144.7°	3.7°
3/ 12/ 3 $\mu\text{m}$	0.04	water	153.7°	160.9°	151.3°	4.0°
		Hexadecane	153.4°	160.5°	140.1°	4.3°
3/ 12/ 1.5 $\mu\text{m}$	0.04	water	154.3°	162.0°	151.0°	3.6°
		Hexadecane	152.6°	162.1°	142.4°	4.5°
3/ 12/ 1.1 $\mu\text{m}$	0.04	water	154.7°	160.1°	152.5°	3.8°
		Hexadecane	153.1°	160.4°	140.3°	4.8°
3/ 12/ 0.8 $\mu\text{m}$	0.04	water	154.9° to 107.7°	-	-	-
		Hexadecane	154.3°	160.7°	140.2°	5.0°

(a) Solid area fraction is calculated based on the actual size of the pillars measured from the SEM images, not the designed solid area fraction on the mask, (b) all measurements were averaged of >5 independent measurements and the error is 2° or better.

In addition, we also studied their advancing and receding contact angle and contact angle hysteresis. The data for these two surfaces are incorporated into the plots in Figures 3-5 and 6 (X



for the 1  $\mu\text{m}$  pillar array and O for the 5  $\mu\text{m}$  pillar array). The data for the 1  $\mu\text{m}$  and 5  $\mu\text{m}$  pillar array surfaces are found to be compatible with the data from the 3  $\mu\text{m}$  pillar array surfaces. The results suggest that the dynamic contact angle behavior of the liquid drops studied in this thesis is mainly controlled by the solid area fraction. Both sliding angle and contact angle hysteresis decrease, independent of the pillar size, as the solid area fraction is lowered. This finding confirms that solid area from the pillars, which generate surface friction due to pinning in the rough surface, is the key contributor in determining the surface's dynamic contact angle behavior.<sup>16</sup>.

### 3.3.3 Effect of Pillar Height

The effect of pillar height on the surface properties were studied using 3  $\mu\text{m}$  pillar array surfaces with a center-to-center pillar spacing of 12  $\mu\text{m}$ . We choose solid area fraction 0.04 because it represents a stress case for liquid sagging. In this experiment, we vary the pillar height from  $\sim 7.8$   $\mu\text{m}$  to  $\sim 0.8$   $\mu\text{m}$ . Pillar array surfaces with varying heights can be fabricated by changing the number of Bosch etching cycles. The static and dynamic contact angle data are given in the bottom half of Table 3-2. Figure 3-16 (Appendix A) depicts typical SEM micrographs of some of the pillar array surfaces. The overall results indicate that these pillar array surfaces can maintain both their superhydrophobic and superoleophobic states as the pillar height is reduced. Within experimental error, the advancing and receding contact angles as well as the sliding angles are found to be insensitive to the height of the pillars down to 1.1  $\mu\text{m}$  (Figure 3-16). We earlier reported that molten polyethylene wax does penetrate and pin underneath the re-entrant structure in the side wall of the pillar.<sup>6</sup> Surface Evolver modeling in

this thesis (Figures 3-9 and 10) indicates that the water droplet is pinned on the pillar surface and hexadecane droplet is pinned underneath the re-entrant structure. Therefore, both experimental and modeling results indicate that liquid droplets are in the Cassie-Baxter state for pillar array surfaces with heights  $\geq 1 \mu\text{m}$ . The overall results merely confirm that the liquid droplets do sag but not “touching” the bottom of the pillar structure when the pillar height is  $\geq 1 \mu\text{m}$ .

For the surface with the pillar height at  $\sim 0.8 \mu\text{m}$ , we found that the static water contact angle is unstable. The water droplet transitions from  $154.9^\circ$  to  $107.7^\circ$  during the contact angle measurement. Although the hexadecane droplet is more stable and the contact angle is measured at  $154.3^\circ$ , we believe that its stability is marginal. The instability of the water and hexadecane droplets on the pillar array surface with  $0.8 \mu\text{m}$  height is attributable to sagging of the liquid-air interface. As soon as the liquid “touches” the bottom of the pillar structure, the entire pillar array surface is wetted and transitioned to the Wenzel state with a lower static contact angle. The observed difference in instability between the water and hexadecane drop is small and remains to be a subject of further investigation. In any event, our results indicate that stable superhydrophobic and superoleophobic surfaces can be obtained for  $3 \mu\text{m}$  pillar array with a  $12 \mu\text{m}$  pitch, when the pillar height is  $> 1 \mu\text{m}$ .

### 3.3.4 Effect of Pillar Overhang Thickness

To further examine the impact of contact line pinning on the dynamic contact angle behavior, particularly the contact angle hysteresis and sliding angle, we fabricate several straight wall pillar structures with varying overhang thickness. The surface of these textured surfaces is again modified with FOTS. Figure 3-12 depicts the SEM micrographs of the representative

pillar array surfaces with overhang thickness varying from 95 to 1030 nm. The height of these pillars is  $\sim 3 \mu\text{m}$  and the center-to-center spacing is  $\sim 6 \mu\text{m}$ . The static, advancing and receding contact angles and sliding angles for these surfaces were determined with water, hexadecane and octane. Octane is added to probe the response of the surface against liquid with a lower surface tension. Representative sessile drop data for these liquids are provided in Figure 3-12. Basically all the pillar array surfaces are superhydrophobic with static water contact angles at  $\sim 150^\circ$  and sliding angles around  $10^\circ$ , independent of the thickness of the overhang structure. On the other hand, the static, advancing and receding contact angles and sliding angles for hexadecane and octane are found to be sensitive to the thickness of the overhang. Figures 3-13a and b plot the effect of overhang thickness on the advancing and receding contact angle and sliding angle, respectively, for the three probing liquids. The plot on the effect of overhang thickness on the static contact angle is provided in Appendix B (Figure 3-17). The overall results indicate that the thickness of the overhang structure has very little effect on the water contact angles and sliding angle, whereas the effect is observable for hexadecane and is increased for octane.

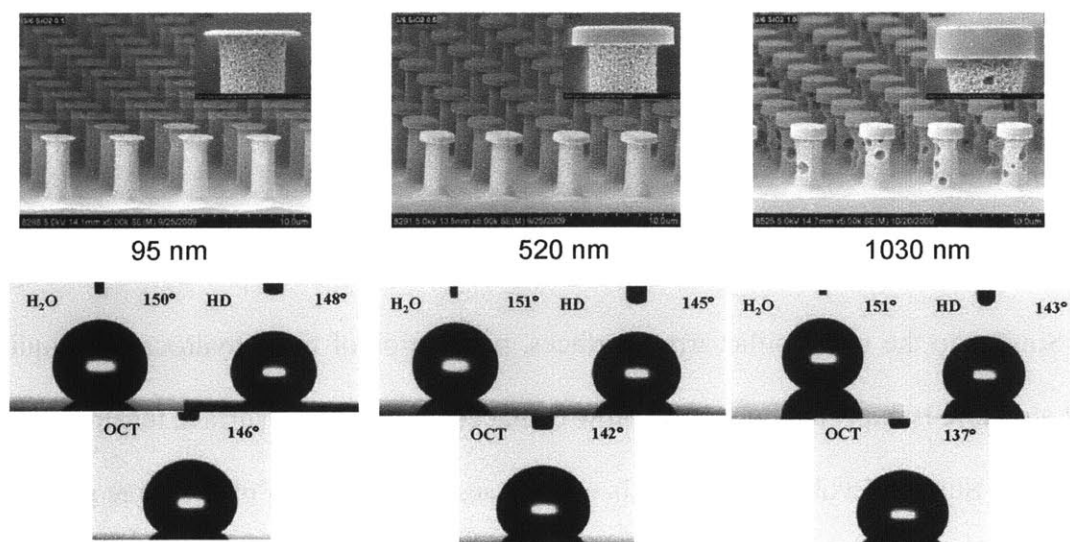


**Figure 3-12** SEM micrographs and sessile drop data for straight wall pillar arrays with overhang thickness varying from 95 nm to 520 nm to 1030 nm.

The static contact angles for water, hexadecane and octane on FOTS modified Si-wafer are  $107^\circ$ ,  $73^\circ$  and  $60^\circ$ , respectively and their surface tensions are 72.3, 27.5 and 21.6 mN/m, respectively. Using the contact angle and surface tension data and the geometry of the overhang pillar array structure, the location of the three-phase contact line was studied by Surface Evolver modeling (Figure 3-9). The results suggest that water droplet is pinned on the pillar surface (around the edge). This is clearly seen with the thick overhang (1030 nm) pillar array surface where wetting of the pillar surface and sagging of the liquid at the air-liquid interface are clearly discernible. Since there is little penetration of water into the pillar structure, the lack of any overhang thickness effect on the contact angle and sliding angle is not unexpected.

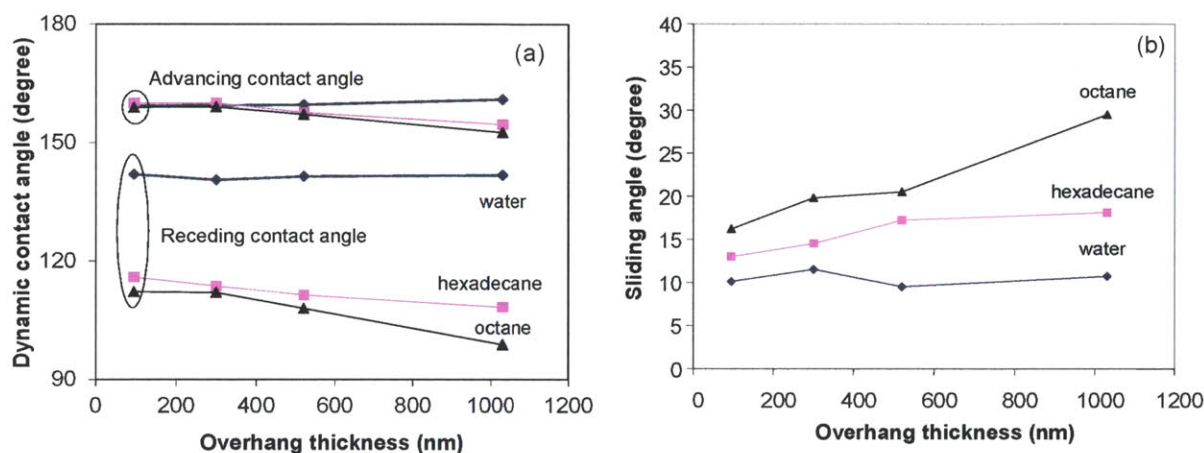


**Figure 3-13** Plots of (a) advancing and receding contact angle and (b) sliding angle as a function of the thickness of the overhang for straight wall pillar array FOTS surfaces with different overhang thickness.

The overhang thickness effect is observable for hexadecane and becomes largest for octane. Similar to the wavy pillar array surfaces, penetration of these hydrocarbon liquids into the pillar structure is expected due to their low contact angles and low surface tensions relative to water. Again, Surface Evolver modeling is used to study the location of the three phase contact line and the results for hexadecane are presented in Figure 3-10. Indeed, hexadecane is found to

wet the pillar surface and the side wall of the overhang. The result also shows that hexadecane is pinned at the lower edge of the overhang structure. The observation of the overhang thickness effect on all the contact angles and sliding angle with hexadecane can be attributable to the penetration of the hydrocarbon liquid into the pillar structures. As a result, the thicker the overhang thickness, the deeper the penetration of the hexadecane drop into the pillar structure and this will result in a decrease in contact angles and an increase in the sliding angle. Very similar composite interface geometry is expected for octane. In the case of octane, more sagging is anticipated due to the lower surface tension. The effect on the contact angles and sliding angle will be larger and indeed this is what we observe in Figures 3-13a and b.

### 3.3.5 Surface Robustness

While the demonstration of surface superoleophobicity is certainly significant, it is imperative that the surface has to be “robust” against wetting and mechanical stress under pressure for any practical application. In this thesis, we define robustness as the ability of the surface to maintain its superoleophobicity under pressure and mechanical stress, such as abrasion. The fundamental question is: what are the design parameters for a “robust” superoleophobic surface?

*Wetting Robustness against Pressure.* We study the effects of surface chemistry (contact angle) and pillar size & spacing on the wettability against the breakthrough pressure using the Surface Evolver modeling methodology developed by Tuteja and co-workers.<sup>11</sup> The result of the modeling study is given in Figure 3-14, which shows the wetting of the overhang pillar array FOTS surface (static contact angle  $\sim 70^\circ$  was used in the calculation) by hexadecane as a function

of external pressure. The simulation shows that hexadecane first wets the pillar surface and the overhang, and then pins underneath the re-entrant structure as the external pressure increases from 0 to 1 to 3 kPa. Concurrently, sagging of the hexadecane drop increases. There are two wetting failure modes associated with the external pressure. For example, if the pillar height ( $h$ ) is short, pressure can induce excessive sagging of the hexadecane drop at the liquid-air interface which may lead to wetting of the bottom of the pillar structure, resulting in transition from the superoleophobic Cassie-Baxter state to the fully wetted Wenzel state (Figure 3-3a). This is designated as  $H^*$  failure.<sup>11</sup> For 3 mm diameter pillar array surface with a 12 mm pitch, the results in Table 3-2 and Figure 3-16 suggest that the critical pillar height ( $H_c$ ) to avoid  $H^*$  failure is  $>1$  mm.  $H_c$  is expected to decrease as the pitch size decreases. On the other hand, as the external pressure applied to the composite interface is increased, an increase in capillary pressure may lead to advancing of the liquid at the contact line, resulting in wetting of the entire pillar structure (Figure 3-3b). This is designated as  $T^*$  failure by Tuteja and co-workers.<sup>11</sup> Since most of the pillar array surfaces were designed with pillar height exceeds  $H_c$ ,  $T^*$  will become the major wetting failure when the breakthrough pressure is reached.

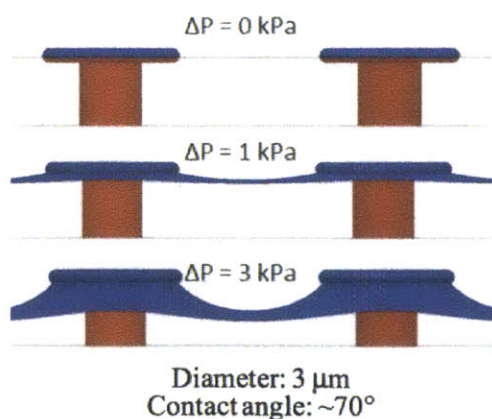


**Figure 3-14** Surface Evolver simulation: wetting of a pillar array FOTS surface with an overhang re-entrant structure by hexadecane

Figure 3-15a summarizes the results from Surface Evolver simulation of hexadecane on the four textured surfaces shown in Figure 3-1. Basically, the simulation allows us to examine the effect of surface texturing (spacing) on the breakthrough pressure. The structural parameter used in the plot is  $D^*$ .  $D^*$  is defined as  $(W + D)^2/W^2$  where  $2W$  is the diameter of the pillar and  $2D$  is the separation distance between two pillars (see Figure 3-4). The result indicates that, for the 3 mm pillar array surfaces, the breakthrough pressure increases from  $\sim 1.3$  to  $\sim 12.4$  kPa, when the separation between pillars decreases from 9 to 1.5 mm. Breakthrough pressure can increase further if  $D^*$  continues to decrease.

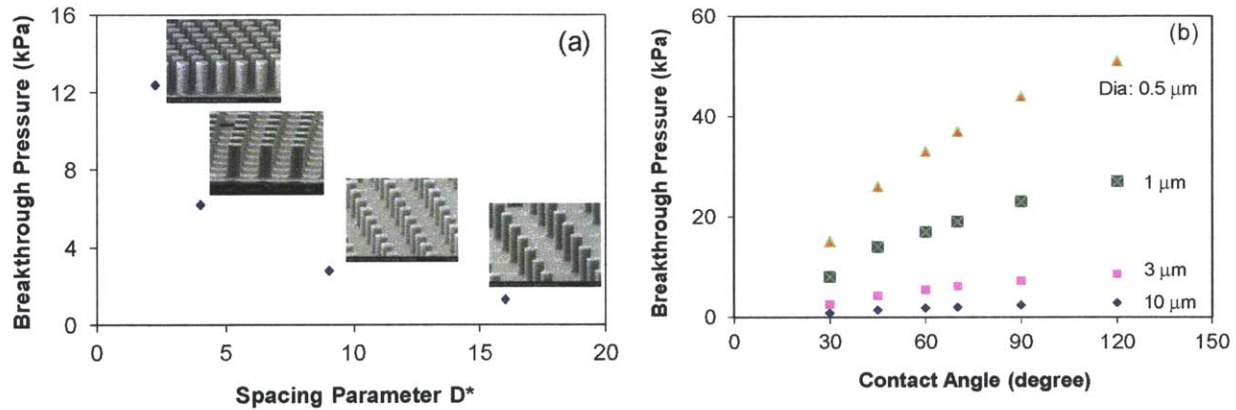


**Figure 3-15** Plot of breakthrough pressure as a function of (a) spacing parameter  $D^*$  and (b) static contact angle for pillar array surfaces with different pillar diameters at  $D^* = 4$ .

Figure 3-15b plots the breakthrough pressure of the hexadecane drop from the Surface Evolver simulation as a function of the surface contact angle for pillar arrays of different diameters. The  $D^*$  value is kept at 4 ( $W = D$ ) in the plot. Expectedly, breakthrough pressure increases as the surface contact angle increases. More importantly, the results also show that there is a strong pillar size effect on the breakthrough pressure. For a given  $D^*$ , the smaller the

pillar diameter, the higher the breakthrough pressure against wetting. Therefore, the key design parameters for robustness against wetting breakthrough pressure are: surface contact angle, pillar diameter and pillar spacing when the height is greater than  $H_c$ . The overall results in Figures 3-15a and 12b suggest that superoleophobic surface with wetting breakthrough pressure at  $\sim 70$  kPa is attainable with a 0.5 mm pillar array surface at a pillar separation of 0.25 mm. Since the pillar separation is so small, the  $H_c$  value of such as surface is likely less than 0.5 mm.

*Robustness against Mechanical Abrasion.* Another aspect of surface robustness is mechanical stability under pressure. The key mechanical failures would be pillar bending and buckling. Figure 3-4 shows the mechanical model used to assess the robustness of the pillar array surface.

As discussed in section 3.1.3, by applying all the related properties of silicon and the geometrical parameters of the pillar array surface (*e.g.*, for the surface in Figure 3-1b,  $2W = 3 \mu\text{m}$ ,  $2D = 3 \mu\text{m}$ ,  $D^* = 4$  and  $H = 7.8 \mu\text{m}$ ) into Eq. 3-1,  $F_{s,global}/A$  is calculated to be  $\sim 1.7 \times 10^5$  kPa. Similarly,  $F_{n,global}/A$  is found to be  $\sim 8.5 \times 10^5$  kPa according to Eq. 3-2 when  $N^* = 1$ . Since a smaller  $F_{s,global}/A$  value is obtained from Eq. 3-1, the comparison suggests that the likely mechanical failure for the of pillar array surface is pillar bending. Indeed, bending failure has been reported for analogous PDMS pillar array surface.<sup>20,21</sup>

Experimentally, we have assessed the mechanical strength of the pillar array surface in Figure 3-1b against bending using a Nano indenter. Scratches of 500  $\mu\text{m}$  in length with increasing load were performed on the pillar array surface to find out the critical load when pillars start to break. The corresponding frictional force on a single pillar was found to be  $\sim 20$  mN and this number is used to calculate the breaking stress where  $F_{s,global}/A$  is found to be



$\sim 2.2 \times 10^6$  kPa. The  $F_{s,global}/A$  value estimated for bending is  $1.7 \times 10^5$  kPa from Eq. 3-1 and is in rough agreement with the classic mechanical model. From Eq. 3-1, the major driver for mechanical robustness is the aspect ratio ( $H/W$ ), the higher the aspect ratio, the weaker the mechanical property. From the robust surface design viewpoint,  $H$  should be just exceeds  $H_c$ . While pillar array surface with large diameter pillar would be beneficial to mechanical abrasion, one may have to consider its potential negative effect on contact angle hysteresis (Figures 3-5 and 6). The choice of the pillar diameter will depend on the application and the tradeoff between mechanical and wetting robustness.

### 3.4 Conclusion

Early investigation on 3  $\mu\text{m}$  pillar array (6  $\mu\text{m}$  pitch) FOTS surface showed that the surface is both superhydrophobic and superoleophobic with water and hexadecane contact angles at  $\sim 150^\circ$  and sliding angles at  $10^\circ$ . Evidence was provided that drops of both water and hexadecane are in the Cassie-Baxter state. Structure-property relationship study revealed that surface fluorination and the re-entrant structure in the side wall of the pillar are contributors to superoleophobicity. We investigate the effect of surface texturing on wettability, drop mobility and contact angle hysteresis. In addition, we also examine the key parameters for the design of a robust superoleophobic surface against wetting breakthrough pressure and mechanical abrasion.

Systematic investigation reveals that both pillar diameter and pillar spacing have little effect on the super (water and oil) repellency where the static and advancing contact angles of these surfaces remain unchanged at  $\sim 150^\circ$  and  $\sim 160^\circ$  for both water and hexadecane, respectively. On the other hand, the sliding angle, receding contact angle and contact angle

hysteresis are all found to be sensitive to surface texturing. Specifically, the receding contact angle is shown to decrease and sliding angle and hysteresis increase as the solid area fraction increases. The surface texturing effect is stronger for hexadecane as compared to water. The overall effect can be attributed to where the contact line is pinned in the pillar structure. For instance, droplet of hexadecane is shown to pin underneath the re-entrant structure, whereas droplet of water only pins on the pillar surface.

Surface Evolver modeling is applied to understand the effect of surface texturing on the robustness of the drop against external wetting breakthrough pressure. Our results show that the key design parameters for high breakthrough pressure are the surface contact angle, pillar diameter and pillar spacing. Robustness against wetting breakthrough pressure increases as the contact angle increases and as  $D^*$  decreases. It is estimated from the results in Figure 3-15 that the breakthrough pressure for the hexadecane drop can reach  $\sim 70$  kPa with a  $0.5 \mu\text{m}$  diameter pillar array FOTS surface.

Simple mechanical analysis suggests that pillar bending is the main failure for the pillar array surface. The key design parameter for high mechanical property is the aspect ratio ( $H/W$ ) of the pillar, the smaller the aspect ratio, the stronger the surface mechanically. While large diameter pillar will enhance mechanical robustness, it will have an effect on  $D^*$  and contact angle hysteresis. Depending on the design target and application, tradeoff between mechanical and wetting may be required. Assuming the superoleophobic surface is used as a printing surface in certain application, for redundancy and good engineering practice, a cleaning blade may still be installed for emergency or occasional gentle maintenance. The surface pressure exerted by a cleaning blade normally ranges between  $\sim 10$  to  $30$  kPa.<sup>22-24</sup> This assumes a loading force of 1 to 3 g/mm with a  $\sim 1$  mm nip width. The normal pressure exerted by the cleaning blade on the

superoleophobic print surface appears to be a factor of 2 lower than the wetting breakthrough pressure estimated for the 1  $\mu\text{m}$  pillar array FOTS surface and is a lot lower than the pressure (order of  $10^6$  kPa) that can cause bending failure. The practical value of the superoleophobic surface for printing and other industrial applications is indicated.

## Appendix A Effect of Pillar Height on the Surface Properties

Figure 3-16 (top) depicts typical SEM micrographs of 12  $\mu\text{m}$  pitch, 3  $\mu\text{m}$  pillar array FOTS surfaces with different pillar heights. A large pillar separation is selected for this experiment to specifically studying the wetting failure related to liquid droplet sagging in the Cassie-Baxter state. Figure 3-16 (bottom) plots the effect of the pillar height on the static, advancing and receding contact angle and the sliding angle with water and hexadecane. The results show that the height of the pillar has little effect on both superhydrophobicity and superoleophobicity for pillar array surfaces when height is  $>1 \mu\text{m}$ . As for the surface with 0.8  $\mu\text{m}$  pillar height, both water and hexadecane droplets are found to be less stable, transitioning to the fully wetted Wenzel state upon vibration or standing for a long time.

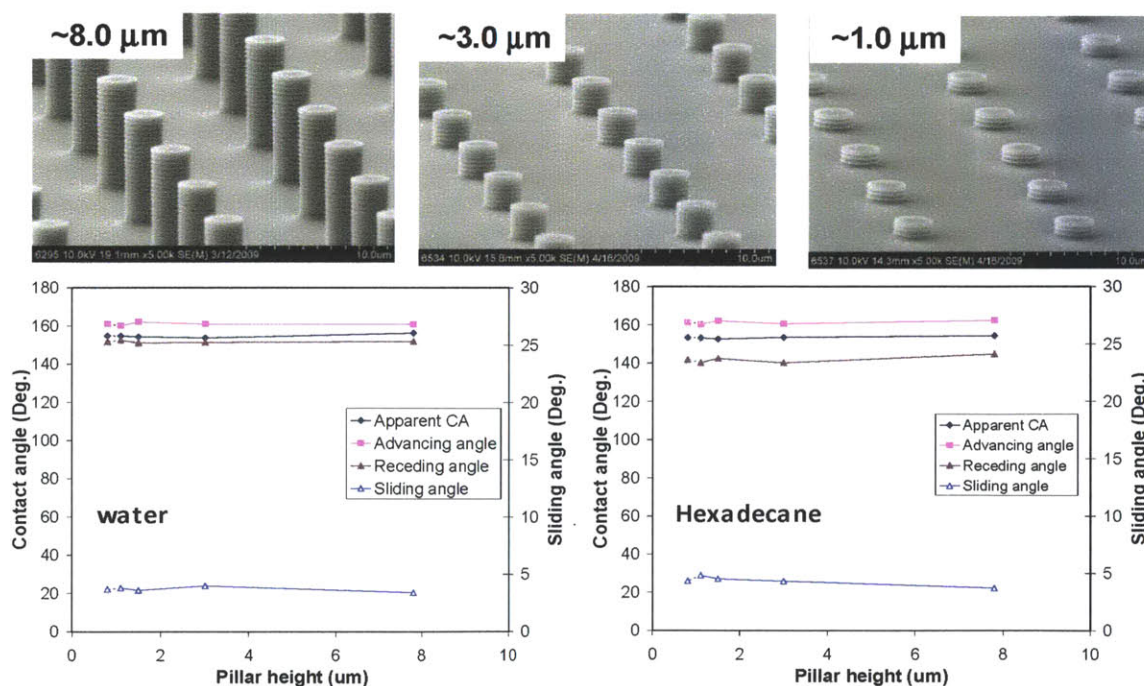


**Figure 3-16** (top) SEM micrographs of 3  $\mu\text{m}$  pillar array surfaces with different height and (bottom) plots of static and dynamic contact angles of the 3  $\mu\text{m}$  pillar array surfaces as a function of pillar height.

## Appendix B Static Contact Angle Data for Pillar Array FOTS Surfaces with Varying Overhang Thickness

In addition to the advancing and receding contact angle data plotted in Figure 3-13a, we also study the effect of overhang thickness on the static contact angle for the overhang pillar array FOTS surfaces (Figure 3-12) with water, hexadecane and octane. Figure 3-17 plots the static contact angles with water, hexadecane and octane as a function of the thickness of the overhang. Similar to the results in Figure 3-13a, practically no overhang thickness effect is observed with water. With hexadecane, the static contact angle decreases as the overhang thickness increases. The overhang thickness effect is larger with octane.

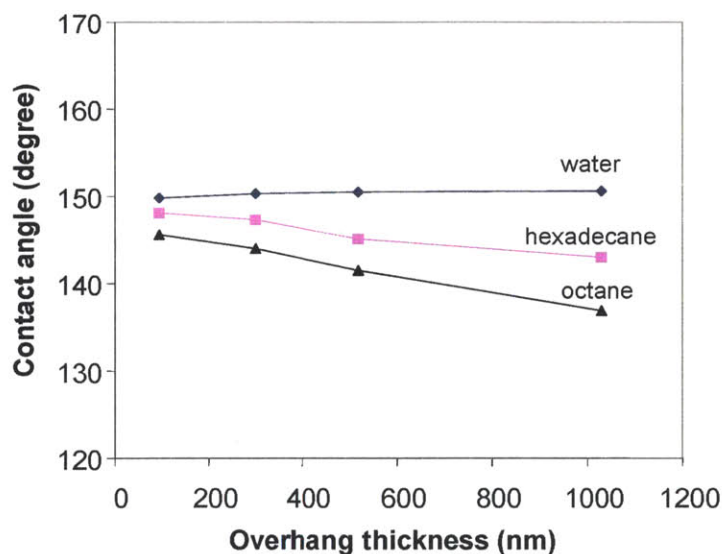


**Figure 3-17** Plots of static contact angle as a function of thickness of the overhang for straight wall pillar array FOTS surfaces with different overhang thickness.

## References

1. Roach, P.; Shirtcliffe, N. J.; Newton, M. I. Progress in Superhydrophobic Surface Development. *Soft Matter* **2008**, *4*, 224-240.
2. Zhang, X.; Shi, F.; Niu, J.; Jiang, Y.; Wang, Z. Superhydrophobic Surfaces from Structural Control to Functional Applications. *J. Mater. Chem.* **2008**, *18*, 621-633.
3. Barthlott, W.; Neinhuis, C. The Purity of Sacred Lotus or Escape from Contamination in Biological Surfaces. *Planta* **1997**, *202*, 1-8.
4. Neinhuis, C.; Barthlott, W. Characterization and Distribution of Water-Repellent, Self-Cleaning Plant Surfaces. *Annals. Botany* **1997**, *79*, 667-677.
5. Tuteja, A.; Choi, W.; McKinley, G. H.; Cohen, R. E.; Rubner, M. F. Design Parameters for Superhydrophobicity and Superoleophobicity. *MRS BULLETIN* **2008**, *33*, 752-757.
6. Zhao, H.; Law, K. Y.; Sambhy, V. Fabrication, Surface Properties, and Origin of Superoleophobicity for a Model Textured Surface. *Langmuir* **2011**, *27*, 5927-5935.
7. Law, K. Y.; Zhao, H. Do We Need Better Materials than Teflon in Marking? *NIP 25 and Digital Fabrication 2009, Technical Program and Proceedings* **2009**, 53-56.
8. Zhao, H.; Law, K. Y. Super Toner and Ink Repellent Superoleophobic Surface. *ACS Applied Mat'ls & Interface* **2012**, *4*, 4288-4295.
9. Brakke, K. A. *The Surface Evolver. Experimental Mathematics* **1992**, *1(2)*, 141-165.
10. L.S. Srinath *Advanced Mechanics of Solids*, 3<sup>rd</sup> ed.; Tata McGraw-Hill Education, **2009**.
11. Tuteja, A.; Choi, W.; Mabry, J. M.; G. C.; McKinley, G. H.; Cohen, R. E. Robust Omniphobic Surfaces. *Proc. Nat. Acad. Sci.* **2008**, *105*, 18200-18205.
12. Woodward, R. P. Contact Angle Measurements Using the Drop Shape Method. [www.firsttenangstroms/pdffdocs/CAPaper.pdf](http://www.firsttenangstroms/pdffdocs/CAPaper.pdf).
13. Choi, W.; Tuteja, A.; Mabry, J. M.; Cohen, R. E.; McKinley, G. H. A Modified Cassie-Baxter Relationship to Explain Contact Angle Hysteresis and Anisotropy on Non-wetting Textured Surfaces. *J. Colloid Interface Sci.* **2009**, *339*, 208-216.
14. Cassie, A. B. D.; Baxter, S. Wetting of Porous Surfaces. *Trans. Faraday Soc.* **1944**, *40*, 546-551.
15. Nosonovsky, M. Model for Solid-Liquid and Solid-Solid Friction of Rough Surfaces with Adhesion Hysteresis. *J. Chem. Phys.* **2007**, *126*, 224701.
16. Sakai, M.; Kono, H.; Nakajima, A.; Zhang, X.; Sakai, H.; Abe, M.; Fujishima, A. Sliding of Water Droplets on the Superhydrophobic Surface with ZnO Nanorods. *Langmuir* **2009**, *25*, 14182-14186.
17. Krumpfer, J. W.; Bian, P.; Zheng, P.; Gao, L.; McCarthy, T.J. Contact Angle Hysteresis on Superhydrophobic Surfaces: An Ionic Liquid Probe Fluid Offers Mechanistic Insight. *Langmuir* **2011**, *27*, 2166-2169.
18. Lv, C.; Yang, C.; Hao, P.; He, F.; Zhang, Q. Sliding of Water Droplets on Microstructured Hydrophobic Surfaces. *Langmuir* **2010**, *26*, 8704-8708.

19. Dorrer, C.; Ruhe, J. Advancing and Receding Motion of Droplets on Ultrahydrophobic Post Surfaces. *Langmuir* **2006**, *22*, 7652-7657.
20. Zhang, Y.; Lo, C. W.; Taylor, A.; Yang, S. Replica Modeling of High-Aspect-Ratio Polymeric Nanopillar Arrays with High Fidelity. *Langmuir*, **2006**, *22*, 8595-8601.
21. Greiner, C.; Campo, A.; Arzt, E. Adhesion of Bioinspired Micropatterned Surfaces: Effect of Pillar Radius, Aspect Ratio, and Preload. *Langmuir* **2007**, *23*, 3495-3502.
22. <http://en.wikipedia.org/wiki/Xerography>
23. Thayer, B. E. High Load Low Load Cleaning Blade Assembly. *US Patent 7,283,781* **2007**.
24. Harpavat, G. L. A Theoretical Study of the Mechanics of a Xerographic Cleaning Blade. *IEEE Trans. Ind. Appl.* **1979**, *IA-15*, 681-687.





## **CHAPTER 4**

### **4. Drop Impact Dynamics of Dilute Polymer Solutions on Textured Hydrophobic Surfaces**

## 4.1 Introduction and Theory

### 4.1.1 Deposition of Impacting Droplets and Dilute Polymer Aqueous Solutions

The deposition of liquid droplets onto dry solid surfaces is an important problem for numerous applications ranging from inkjet printing to printing electronic circuits, to delivering DNA- or protein- bioassays, to spraying pesticides onto plant leaves.<sup>1-4</sup> However, a significant portion of impacting aqueous droplets has been rebounded and lost because of hydrophobicity of natural leaf surfaces that possess either micrometric or nanometric surface textures.<sup>5</sup> To maximize deposition rate of aqueous solutions onto the target textured hydrophobic surfaces, non-Newtonian fluids such as dilute polymer solutions have been highlighted as a solution for this deposition problem.<sup>5-8</sup> Previous studies have shown complete suppression of the droplet rebound on smooth hydrophobic surfaces by adding a small amount of high molecular weight polymer such as polyethylene oxide (PEO) into water, even though this dilute polymer aqueous solution possesses nearly the same surface tension and shear viscosity as water.<sup>5-8</sup> Prior to our discussion on the drop impact dynamics of complex fluids on the hydrophobic textured surfaces, (i) water droplet impact on superhydrophobic surfaces, (ii) shear and extensional rheology of PEO solutions, and (iii) drop impact of dilute polymer solutions on smooth hydrophobic surfaces will be first introduced in the following sections.

### 4.1.2 Drop Impact Dynamics of Water on Superhydrophobic Surfaces

Visualization of drop impact on dry, solid surfaces reveals gradual shape change of impacting droplets and their interaction with solid surfaces.<sup>9, 10</sup> When a typical millimetric raindrop impacts a flat solid surface at a velocity of  $U = 0.1-10$  m/s, initially spherical droplet experiences extreme changes in dynamic pressure due to the generation and propagation of weak shock waves inside the droplet, deforms into nearly a pancake shape and spread in the radial direction in the expansion stage.<sup>9-13</sup> After reaching the maximum diameter  $D_{\max}$  of the pancake shape, a retraction stage follows, which finally ends with droplet rebound or deposition.<sup>9-12</sup> During the expansion stage, the initial kinetic energy before the impact,  $E_{k0} \approx \rho U^2$  of a droplet is partly transformed into surface energy  $E_s \approx \sigma/D^3$  and in the retraction stage this surface energy is converted back into kinetic energy with a different level of energy dissipation depending on the interaction between the impacting droplet and the solid surface.<sup>10</sup>

The dynamics of Newtonian fluid drops impacting on smooth and textured surfaces during the expansion and retraction stages can be described by important parameters summarized in Table 4-1.<sup>10</sup> Depending upon wettability of solid surfaces, physico-chemical properties of fluids and impact conditions (*e.g.*, air pressure), partial rebound, trapping of air bubbles, vibrating water bells, formation of a vertical jet, fingering without splash as well as corona splash can also be observed.<sup>9-12</sup> The important dimensionless groups associated with drop impact dynamics are also summarized in Table 4-1.

**Table 4-1** List of physico-chemical properties of fluids and important dimensionless numbers associated with drop impact dynamics

Notation	Definition
$U$	impacting velocity
$D_o$	initial drop diameter before impact
$D_{\max}$	maximum diameter on the liquid-solid interface
$\eta$	viscosity
$\sigma$	surface tension of fluids
$\rho$	density of fluids
$E_{k0} \approx \rho U^2$	initial kinetic energy before impact
$E_s \approx \sigma/D$	surface energy
$We = \rho U^2 D_o / \sigma$	Weber number, ratio of $E_{k0}$ to $E_{s0}$ (initial surface energy)
$Ca = \eta U / \sigma$	Capillary number, viscous effect relative to capillary effect
$Re = \rho U D_o / \eta$	Reynolds number, inertial effect relative to viscous effect
$Oh = \eta / \sqrt{\rho \sigma D_o}$	Ohnesorge number, viscous effect relative to inertio-capillary effect

Low viscosity drops, *i.e.*  $Oh < 1$ , like the fluids used in this thesis, oscillate on creation with an inertio-capillary timescale given by  $t_R = (\rho D_o^3 / \sigma)^{1/2}$ . Surface tension,  $\sigma$  acts like a spring constant and mass  $\rho D^3$  provides the inertia. Rayleigh time is independent of impact velocity, and estimates the contact time during an impact.

Recent studies have shown that when water droplets impact on textured superhydrophobic surfaces that exhibit an apparent contact angle ( $\theta^*$ ) higher than  $150^\circ$  and contact angle hysteresis (CAH, see Section 1.3 and Figure 1-5 for definition) smaller than  $5^\circ$  for water complete rebound (*i.e.* complete separation of an impacting droplet and the target textured surface, without leaving water on it) can be observed.<sup>10,14-16</sup> Two wetting states of water droplets on rough surfaces that influence drop impact dynamics on superhydrophobic surfaces can be described by two canonical models.<sup>10,17,18</sup> The Cassie-Baxter model (Eq. 1-3)<sup>17</sup> describes droplets sitting partially on solid bumps and partially on air pockets entrapped between the

surface asperities, whereas the Wenzel model (Eq. 1-2)<sup>18</sup> describes droplets that fully wet the textured surfaces. When impacted droplets maintain the Cassie-Baxter state because of high robustness of superhydrophobicity of textured surfaces, insufficient viscous energy dissipation on solid-liquid interface by a small solid area fraction ( $f_s$ ) can lead to the complete rebound of impacted droplets.<sup>10,14-16</sup>

However, if the breakthrough pressure of the textured surface that characterizes the critical pressure difference to maintain the Cassie-Baxter state is not high enough to resist dynamic pressure generated by sudden velocity change of impacting droplets, then the wetting transition from the Cassie-Baxter state to the Wenzel state occurs and complete rebound can be suppressed due to the pinned droplets in the fully wetted Wenzel state.<sup>10,14,15</sup> In this case, more initial kinetic energy before the impact is used to replace initial solid-air interface with solid-liquid interface.<sup>10,14,15</sup> In summary, for water droplet impacts on superhydrophobic surfaces, both physico-chemical properties of water (*e.g.* impact velocity) and surface characteristics (*e.g.*, robustness of superhydrophobicity) can influence the drop impact dynamics.

#### 4.1.3 Shear and Extensional Rheology of Dilute PEO Solutions

A polymer solution exhibits viscoelasticity when the solution is under deformation.<sup>19</sup> This unique property of a polymer solution stems from the morphological transformation of polymer coils in the solution.<sup>19</sup> The intrinsic elasticity of polymer solutions can be characterized by Deborah number,  $De = \lambda / t_R$  that compares the fluid relaxation time,  $\lambda$  to Rayleigh time,  $t_R$ .<sup>19</sup> The hydrodynamic interaction between polymer coils and surrounding solvent is strongly

influenced by the concentration of solution relative to the critical overlap concentration ( $c^*$ ) at which nearby polymer coils start to overlap.<sup>19</sup> In the case of  $c \sim c^*$ , polymer coils start to influence each other's hydrodynamics and the interaction between polymer coils cannot be considered as independent.<sup>19</sup> If the concentration is much less than the critical concentration ( $c \ll c^*$ ), the polymer solution is categorized as a dilute polymer solution and is considered that the interaction between polymer coils is negligible.<sup>19</sup>

In a dilute PEO aqueous solution ( $c \ll c^*$ ) with relatively high molecular weight, small amount of PEO coils in the solution can show low viscosity and significant elasticity.<sup>19,20</sup> The measured intrinsic viscosity ( $[\eta]$ ) of PEO solutions shows sole dependence on the molecular weight and is given by a composite Mark-Houwink-Sakurada (MHS) equation  $[\eta] = 0.072M_w^{0.65}$ .<sup>20</sup> The shear viscosity ( $\eta$ ) of a PEO solution is similar to that of water and can be approximated by the simple formula  $\eta = \eta_s \{1 + [\eta]c + O(c^2)\}$  where  $\eta_s$  is shear viscosity of solvent, that shows linear dependence on the intrinsic viscosity and concentration.<sup>21</sup>

In addition to the shear rheology of dilute PEO solutions, the elasticity of PEO solutions is associated with polymer coils that can be stretched in the sufficient extensional flow and this can be a major contribution of energy dissipation of impacting viscoelastic complex fluids droplets in the retraction stage.<sup>5-8</sup> The stretched polymer solution can be also relaxed to the original morphology.<sup>19</sup> This time-dependent behavior of polymer solution is captured by relaxation time.<sup>19</sup> The Zimm-Rouse theory can provide the meaningful insight and order of magnitude estimate of relaxation time associated with elastic characteristic of dilute polymer solution.<sup>19,21</sup> However, recent study reported that the measured relaxation time is significantly greater than the estimated Rouse-Zimm relaxation time in the dilute PEO solution concentration

region.<sup>21</sup> The relaxation time is thus measured using capillary breakup extensional rheometer (CaBER).<sup>22</sup> The intrinsic elasticity of polymer solutions can be characterized by Deborah number,  $De = \lambda / t_R$  that compares the fluid relaxation time,  $\lambda$  to Rayleigh time,  $t_R$ .<sup>19</sup>

#### 4.1.4 Drop Impact of Dilute Polymer Solutions on Smooth Hydrophobic Surfaces

Previous studies on drop impact of dilute polymer solutions on smooth hydrophobic surfaces have shown that retraction stage exhibits the most dramatic effect of a small amount (~200 ppm) of polymers added into water droplets.<sup>5-8</sup> Bergeron *et al.*<sup>5</sup> argued that higher transient extensional viscosity of polymeric solutions leads to a greater dissipation of energy during retraction stage. While the extensional viscosity of a Newtonian fluid is three times greater than its shear viscosity,<sup>23</sup> complex fluids containing macromolecules can exhibit up to a thousand times greater extensional viscosity.<sup>5</sup> However, the high extensional viscosity argument was contested later primarily on two grounds: (a) It was argued that even though the global extension rate (defined by Bergeron *et al.*<sup>5</sup> as ratio of rim velocity to the height of deformed drop) is larger in the expansion stage, experimentally observed  $D_{\max}$  seems to be unaffected by addition of polymer. (b) No effect of added polymer was observed in drop impact dynamics on small cylindrical targets<sup>24</sup> or on heated surfaces<sup>25</sup>.

Thereafter Bartolo *et al.*<sup>6</sup> suggested that the surface-tension driven retraction in polymer solutions is countered by elastic normal stresses induced in shear flow near the contact line. Smith and Bertola<sup>7,8</sup> tracked micrometric fluorescent particles and fluorescently labeled DNA chains inside impacting drops, and showed that while the velocity within the drop is unaffected, the retraction velocity of the rim is reduced considerably, and the DNA chains get stretched near

the rim. They argued that (a) entropic resistance to stretching and hydrodynamic drag associated with polymer chains creates 'effective friction' at the contact line suppresses rebound and (b) extensional viscosity plays no role.

Other recent studies show that a very thin layer of air remains trapped between the impacting drop and the surface<sup>26-28</sup> during the expansion stage, and the underlying fluid flow is similar to rolling out of a carpet (*i.e.*, drop is merely settling on the wall).<sup>29</sup> Thus the added polymers are not deformed by the large apparent extension rates estimated by ratio of rim velocity and dimension of deforming drop. Since extensional effects are relevant only during the late stage of expansion stage, the initial dynamics during expansion shows self-similar behavior for different surfaces and dilute polymer solutions.<sup>10</sup> On the other hand, throughout the retraction stage, the fluid is in intimate contact with the underlying substrate, and a radial extensional flow component must exist between the moving contact line and stagnation point near the center of drop.<sup>10</sup>

Thus the physics underlying the suppression of rebound on a smooth hydrophobic surface by added polymers still remains elusive and subject of vigorous debate<sup>6-8</sup> and is a motivation for this chapter. Furthermore, the dynamics and outcome from drop impact of viscoelastic complex fluids on textured, superhydrophobic surfaces is nearly unexplored.<sup>6-8</sup> In this thesis, we aim to understand the underlying mechanism, and further explore how viscoelasticity influences drop impact dynamics on textured hydrophobic surfaces. We present drop impact experiments of well-characterized viscoelastic fluids on micro- and nano-textured superhydrophobic surfaces in addition to smooth hydrophobic surfaces. We show that the impact of viscoelastic drops on textured surfaces can result in complete rebound. By adopting a stick-slip flow model<sup>30</sup> on



textured surfaces with various topographic length scales and solid area fractions, we rationalize the dynamics leading to complete rebound following drop impact even for viscoelastic fluids.

## 4.2 Experimental Methods

### 4.2.1 Preparation of Hydrophobic Surfaces

The micropost structure is fabricated utilizing the conventional negative epoxy photoresist photolithography. On a 4 inch single-side-polished test graded silicon wafer (thickness = 550  $\mu\text{m}$ , cleaned by 1:3 volume ratio 30%  $\text{H}_2\text{O}_2$  - 96%  $\text{H}_2\text{SO}_4$  piranha solution for 10 minutes, rinsed by deionized water for 10 minutes, and dehydrated on a hotplate at 180°C for 3 min prior to use), MicroChem SU-8 2015 (40  $\mu\text{m}$ ) was spun uniformly using a spincoater (1000 rpm). The silicon wafer with the SU-8 photoresist was prebaked for 5 minutes at 95°C and then exposed to a UV light source (Electronic Visions, Model EV620 mask aligner, expose dose = 160  $\text{mJ}/\text{cm}^2$ ) through a transparency mask composed of a square array of hole pattern. I baked the silicon wafer on a hotplate for 6 minutes at 95°C again and then immersed into the developer (MicroChem SU-8 developer) and agitated manually for 5 minutes at the room temperature. The developed silicon wafer was cleaned by isopropyl alcohol and then dried by compressed nitrogen. Before introducing the vapor-phase hydrophobic coating (see Section 2.2.2 for details), the developed silicon wafer was immersed into 1M  $\text{H}_2\text{SO}_4$  aqueous solution for 15 minutes.<sup>31</sup> The acid-treated SU-8 structure was rinsed in deionized water for 15 minutes to remove the  $\text{H}_2\text{SO}_4$  and then was dried at the room temperature, followed by silanization process (Section 2.2.2). The nanocone surface was fabricated as described in Sections 2.2.1 and 2.2.2. Glass slides

were treated using the same vapor-phase silanization process to make hydrophobic smooth glass surfaces.

#### 4.2.2 Preparation of Dilute PEO Solutions

Aqueous solutions of PEO of  $M_w = 4 \times 10^6$  Daltons (denoted PEO 4.0M) with the concentrations  $c = 100$  and  $200$  ppm were rationally picked to match with the viscoelastic fluids reported in literature by Smith and Bertola<sup>7,8</sup> and Bonn and coworkers<sup>5,6</sup>. We verified that the aqueous PEO solutions show suppression of rebound on both smooth silanized (SS) glass and on lotus leaf (LL) surface in agreement with the published results<sup>5-8</sup>

The PEO 4.0M, 100 and 200 ppm solutions are dilute solutions, as their concentration  $c < c^*$  where overlap concentration  $c^*$ , defined on the basis of intrinsic viscosity  $c^*[\eta] \approx 1$ , is 400 ppm.<sup>20</sup> Thus these two solutions have concentrations such that  $c/c^* = 0.25$  and  $0.5$  respectively. Shear viscosity,  $\eta$  of dilute polymer solutions increases linearly with concentration  $c$  and at overlap concentration,  $c^*$ , the solution viscosity is nearly double of solvent viscosity. To unravel the effect of added polymer, we additionally use an aqueous solution of PEO 4.0M with 500 ppm ( $c/c^* = 1.25$ ) and three solutions of lower molecular weight polymer, PEO 0.3M ( $M_w = 0.3 \times 10^6$  Daltons). The  $c/c^*$  ratios (and shear viscosity) of three samples are respectively matched with the PEO 4.0M samples. All the PEO solutions were mixed by gently rolling for 48 hours before use.

### 4.2.3 Characterization of Wetting Properties of Textured Surfaces

The apparent contact angle,  $\theta^*$  of water and aqueous PEO solutions on superhydrophobic surfaces is determined by the surface chemistry and solid area fraction  $f_s$  defined in Eq. 1-3. The apparent contact angle  $\theta^*$  increases as the  $f_s$  decreases. The surface characteristics and contact angle values obtained for three surfaces are listed in Table 4-2. Advancing contact angle measurements were performed using a Ramé-hart model 590 goniometer, by dispensing liquid droplets of volume  $V \approx 5 \mu\ell$  and adding volume to the droplets at the flow rate of  $1 \mu\ell / s$ .

**Table 4-2** Geometrical dimensions and wetting properties of different textured surfaces.

Notation	Definition	Width ( $W$ ) [ $\mu\text{m}$ ]	Period ( $L$ ) [ $\mu\text{m}$ ]	Solid Area Fraction ( $f_s = (W/L)^2$ )	Height ( $H$ ) [ $\mu\text{m}$ ]	Water Advancing Contact Angle ( $\theta_{adv}^*$ )	Water Receding Contact Angle ( $\theta_{rec}^*$ )
SS	smooth silanized	N/A	N/A	1	N/A	106±2°	93±2°
MP	micropost	30	60	0.25	40	150±2°	125±5°
NC	nanocone	0.015	0.2	< 0.01	1.1	164±1°	163±1°
LL	lotus leaf	~4	~18	< 0.05	~10	163±1°	156±2°

### 4.2.4 Characterization of Viscoelasticity of PEO Solutions

We used a capillary breakup extensional rheometer (CaBER; Cambridge Polymer Group)<sup>22</sup> to measure the apparent relaxation time  $\lambda$  of each PEO 4.0M solution, and their apparent extensional viscosity. The response of weakly viscoelastic PEO 0.3M solutions is not discernible in CaBER measurements, but estimates based on molecular theories and previously published experiments suggest that their apparent relaxation times and the extensional viscosities are smaller by a factor of  $10^1$  and  $10^2$  respectively at the same  $c/c^*$  ratio as PEO 4.0M.<sup>20</sup> While

the surface tension ( $\sigma = 68 \text{ mN/m}$ ) and shear viscosity of dilute PEO solutions are quite similar, they differ substantially in their elastic properties.<sup>20</sup>

#### 4.2.5 Visual Analysis of Drop Impact Dynamics

The impact velocity  $U$  of the drops was varied by increasing the drop release height. Impact events were imaged using a high-speed camera (Phantom v5.0<sup>TM</sup>) with 12000 frames/s to provide images with 30-40  $\mu\text{m}$  spatial resolution and the contact line dynamics was analyzed using ImageJ and MATLAB.

### 4.3 Results and Discussion

#### 4.3.1 Effect of Textural Length Scale and Solid Area Fraction on Drop Impact Dynamics

For textured hydrophobic surfaces including lotus leaves, the Cassie-Baxter state is essential for droplet rebound and non-wetting behavior under dynamical conditions.<sup>32,33</sup> High dynamic pressures associated with the drop impact greater than breakthrough pressure of textured surfaces can result in impaled drops. A simple critical impact velocity criteria given by Reyssat et al<sup>32</sup> can be rewritten in a dimensionless form as  $We^{0.5} > \sqrt{HD_o/L^2}$ , where  $H$  is height of texture and  $L$  is period (see Table 4-2 for specific values of  $H$  and  $L$  for three representative textured surfaces used in this chapter). From the dimensionless inequality, the robustness of the Cassie-Baxter state increases as height of surface textures increase and period of them decrease.

For the micropost (MP) surface, impalement of impacting water droplets occurs beyond a critical Weber number,  $We_c \approx 25$  whereas water droplets with a lower Weber number ( $We = 14.1$ ) show complete rebound due to enough pressure resistance of the Cassie-Baxter state as shown Figure 4-1a. However, the rebound of PEO droplets is suppressed on the microtextured surface even for  $We = 14.1$  (Figure 4-1b).

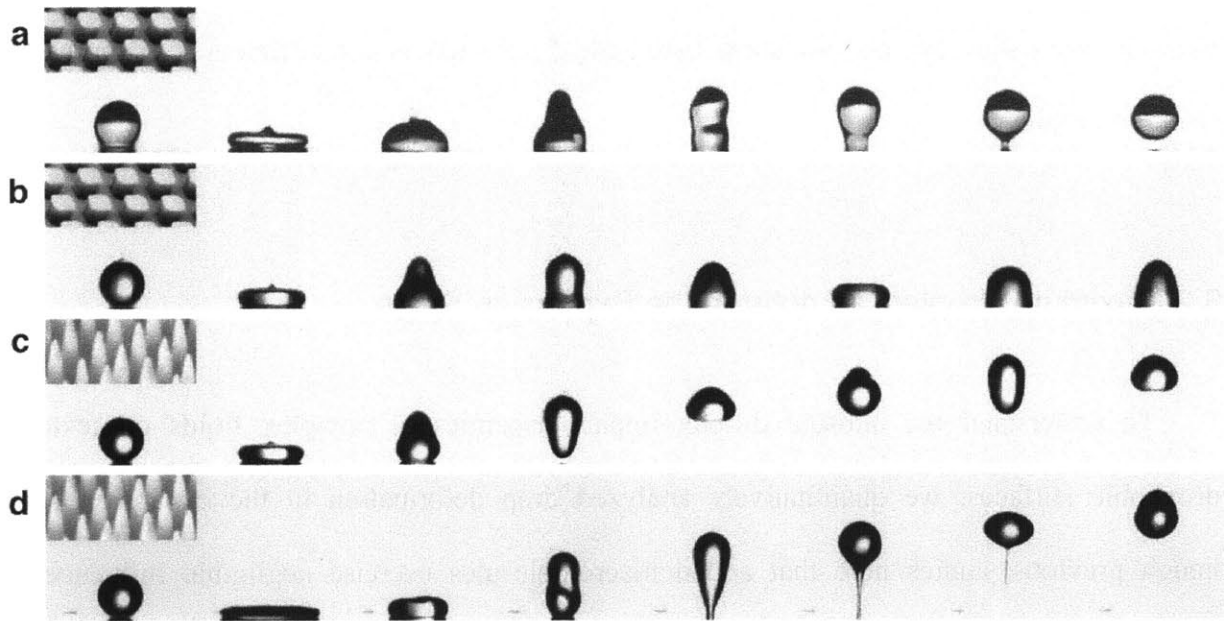


**Figure 4-1** Drop dynamics of water and PEO solution ( $M_w = 4 \times 10^6$  Daltons,  $c = 200$  ppm,  $De = 1.52$ ,  $D_0 = 2.29$  mm), impacting on two different textured hydrophobic surfaces. (a) Water droplet ( $We = 14.1$ ) on the microtextured surface (MP,  $W = 30 \mu\text{m}$ ,  $P = 60 \mu\text{m}$ ,  $H = 40 \mu\text{m}$ ,  $f_s = 0.25$ ) (b) PEO droplet ( $We = 14.1$ ) on the MP surface. (c) PEO droplet ( $We = 14.1$ ) impacting a nanotextured surface (NC,  $W = 8$  nm,  $P = 200$  nm,  $H = 1.1 \mu\text{m}$ ,  $f_s = 0.01$ ). (d) PEO droplet with a higher impact velocity ( $We = 55.6$ ) on the NC surface. Time interval of 2 ms separates successive frames in each row.

The nancone surface remains robustly non-wetting up to higher  $We$  values than micropost surface due to its smaller solid fraction and sub-micron features.<sup>34</sup> The impact of water drops on the nanotextured (NC) surface at the same impact velocity as Figure 4-1a ( $We = 14.1$ ) results in a complete rebound (Figure 4-1c). Interestingly, the high speed video images of impact of 200

ppm PEO 4.0M solution drops also show rebound on a nanocone surfaces at Weber numbers,  $We = 14$  and  $We = 56$ , respectively (Figure 4-1c,d). In fact, for the nanocone surfaces, partial rebound of polymer solution drops is also observed even for impact velocities as high as  $We = 104$ . Our experimental results on textured, superhydrophobic surfaces show that it is possible to induce a complete droplet rebound even for high molecular weight polymer solutions. Thus not only the physics underlying anti-rebound phenomena requires further investigation on the surface characteristics, but also we show here adding polymers is not sufficient for suppressing rebound of droplets.

#### 4.3.2 Maximum Droplet Diameter in the Expansion Stage

To understand the unusual droplet impact dynamics of complex fluids on textured hydrophobic surfaces, we quantitatively analyzed drop deformation in the expansion stage although previous studies note that added macromolecules exercise negligible influence on dynamics during the expansion stage, but dramatically affect the retraction stage.<sup>5-8</sup> For the impact of PEO solution drops on all three artificial surfaces (Table 4-2), the spread factor, defined as non-dimensionalized contact line diameter  $D(t)/D_o$  is self-similar (see Figure 4-2a) and displays an initial  $D(t)/D_o \sim (t/t_R)^{1/2}$  dependence in the expansion stage as is observed for Newtonian fluids. During the expansion stage, the effect of changing impact velocity (captured by  $We$ ), intrinsic elasticity (captured by  $De$ ) and surface wettability is observed in the maximum diameter,  $D_{\max}$  as shown in Figure 4-2b.

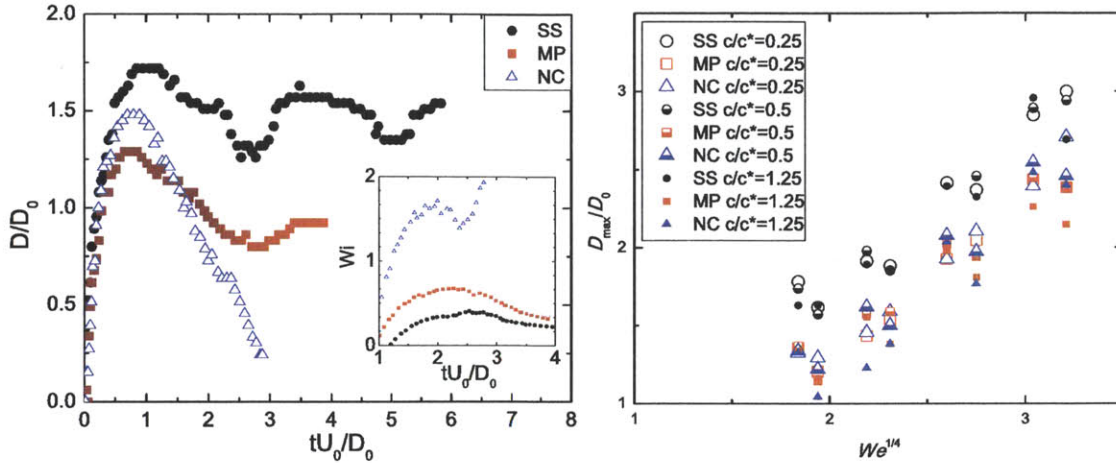


**Figure 4-2** (a). Time evolution of dimensionless drop diameter at the contact line and Weissenberg number ( $Wi$ , retraction stage only, shown in the inset) of impacting PEO solution ( $M_W = 4 \times 10^6$  Daltons,  $c = 200$  ppm,  $De = 1.52$ ,  $D_0 = 2.29$  mm), on three representative surfaces at  $We = 14.1$ . The retraction velocity and apparent  $Wi$  are highest for the nanotextured surface (NC), where complete rebound is observed. (b) Maximum spread factor (ratio of the maximum diameter to initial drop diameter before the impact) as a function of  $We^{1/4}$ . The silanized smooth (SS), micropost (MP) and nanocone (NC) are respectively shown as black circles, red squares and blue triangles, and for PEO 4.0M, three different concentrations are represented using different size symbols.

Furthermore, we find that the drops of aqueous solutions of PEO 4.0M exhibit  $D_{max} \sim D_0 We^{1/4}$  scaling on all the three artificial hydrophobic surfaces. Newtonian fluid drops also exhibit this scaling<sup>29</sup> in the limit of low viscosity ( $Oh < 1$ ). However, as shown in Figure 4-2b, for dilute polymer solution, the results for  $D_{max}$  display  $D_{max,SS} > D_{max,NC} > D_{max,MP}$  although according to a previous study on the maximum diameter of a static drop,  $D_{max}$  is expected on basis of receding contact angle  $\theta_{rec}$  computed using  $D_{max,rec} = 2D_0 \sin \theta_{rec} [2(1 - \cos \theta_{rec})(2 - \cos \theta_{rec} - \cos^2 \theta_{rec})]^{-1/3}$ , which should decrease with increasing hydrophobicity ( $D_{max,SS} > D_{max,MP} > D_{max,NC}$ ).<sup>10</sup> A lower viscous energy dissipation on nanocone surfaces must be responsible for an apparently larger  $D_{max}$ . Unlike previous studies<sup>5-8,35</sup>, we find that the absolute value of  $D_{max}$  on smooth hydrophobic surface is also affected by

both polymer concentration and molecular weight: higher concentration and higher molecular weight lead to a lower  $D_{\max}$ . Similar results are observed on textured surfaces, implying elastic effects do play a role during expansion stage as well.

### 4.3.3 Stress Growth by Stretch and Relaxation of Polymer Coils

The representative dynamics of weakly viscoelastic solutions in response to imposed deformation can be described by use of Oldroyd-B model, where polymeric contribution to fluid stress  $\tau_p$  is given by  $\tau_p + \lambda \tau_{p(1)} = \eta_p \dot{\gamma}$ .<sup>36</sup> Here  $\tau_{p(1)}$  is upper-convected derivative and  $\eta_p$  is polymeric contribution to solution viscosity. An analytical solution of Oldroyd-B model under constant extensional rate  $\dot{\epsilon}$  can be written down to show that the magnitude of  $\tau_p$  depends upon Weissenberg number,  $Wi = \dot{\epsilon} \lambda$  (compares deformation rate,  $\dot{\epsilon}$  to relaxation rate,  $1/\lambda$ ).<sup>36</sup>

According to this model, the value of  $\tau_p$  increases rapidly for  $Wi > 0.5$  beyond which coil stretch transition becomes possible.<sup>20</sup>  $D_{\max}$  values for PEO 4.0M solutions with higher molecular weight (and higher  $De$ ) are consistently smaller than the corresponding values for PEO 0.3M and water drops, implying that polymer solutions with larger relaxation time dissipate more energy (have higher  $Wi$ ) even in the expansion stage.



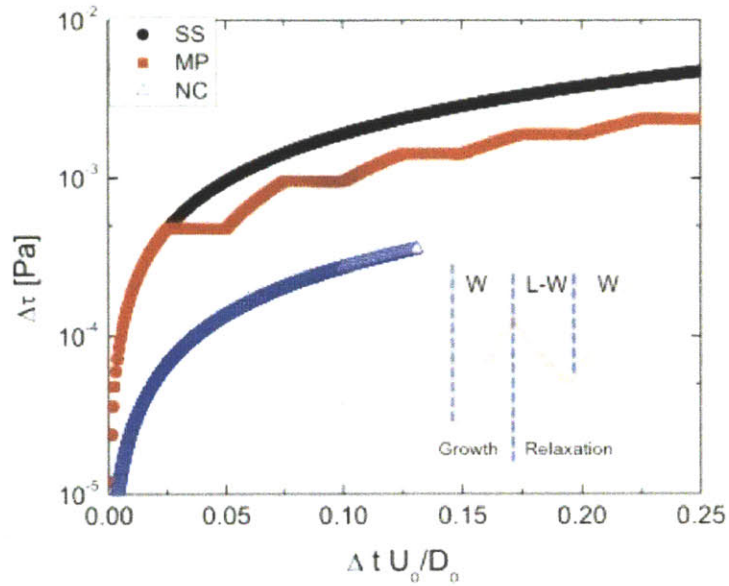


**Figure 4-3** Time evolution of normal stress difference ( $\Delta\tau$ ) of PEO solution ( $M_w = 4 \times 10^6$  Daltons,  $c = 200$  ppm,  $We = 14.1$ ) is shown for the three different surfaces. For the same time duration and extensional rate, the nanotextured surface (NC) displays higher retraction velocity and higher apparent extension rate than the microtextured surface (MP). And it shows a smaller normal stress difference, implying a lower energy dissipation level by polymer stretching due to extensional flow, which rationalize the observed complete rebound of PEO solution. Inset: The schematic drawing of stress growth and stress relaxation associated with stick-slip fluid motion over a textured surface.

We can define an apparent extension rate in terms of retraction velocity  $V_R(t)$  and radius of the drop  $R(t)$ , as  $\dot{\epsilon} = 2V_R/R$ . Using  $\dot{\epsilon} = 2V_R/R$ , a simplest estimate (lower bound) can be found for  $Wi = \dot{\epsilon}\lambda$ .<sup>19</sup> Macromolecules can reach a high degree of extension in flow when two conditions are satisfied: 1) critical rate condition and 2) accumulated strain condition are satisfied.<sup>19</sup> The first condition requires or strain rate,  $\dot{\epsilon}$ , to exceed the relaxation rate  $1/\lambda$ , or require a high  $Wi > 0.5$ .<sup>19</sup> The accumulated strain condition requires the strain rate to be maintained for long enough to accumulate in the molecule.<sup>19</sup> We find that the  $Wi$  values during retraction are reasonably high (close to 0.5) implying that the extensional effects are significant enough to drive a coil-stretch transition observed by Smith and Bertola<sup>7</sup>. Complete stretching of coils occurs only in strong, sustained extensional flow fields, whereas strong shear flow only

deforms polymer coils.<sup>19</sup> Under similar drop impact conditions, since the extensional viscosity of polymer solutions with a higher polymer concentration or molecular weight is higher, these polymer solutions can display an increased energy dissipation near the contact line, resulting in a lower retraction velocity.

The physical picture of fluid motion over superhydrophobic surfaces is more complex.<sup>30</sup> Fluid elements moving over a textured surface experience a succession of no slip and slip boundary condition.<sup>30</sup> In this case, the local flow field is periodically extensional, and the time scales for the successive extensional stress growth and stress relaxation resulting from the local flow field can be influenced by the impact velocity, feature size and the solid area fraction.<sup>30</sup> Although the local flow field over textured surfaces may not be purely extensional, *i.e.* vorticity is non-zero, we use Oldroyd-B model as a simple model to capture the essential physics since we are interested in extra dissipation contributed by polymers due to extensional effects. In Figure 4-3, we illustrate numerically computed stress accumulation in a polymer solution on three different surfaces, showing the highest extensional stress accumulated for smooth surfaces, and the lowest for the nanocone surface. In the limit of high  $Wi$  number, for a given constant extensional rate, asymptotic limit can be deduced as follows. The stress growth per cycle is proportional to  $\exp(2\hat{e}t_1)$ , where the growth occurs for a time proportional to  $t_1 = W/V_R = \sqrt{f_s}L/V_R$ , whereas the relaxation per cycle is proportional to  $\exp(-t_2/\lambda)$  where a representative time for relaxation is  $t_2 = (L-W)/V_R$ . And the total number of stick-slip cycles are set by  $L/D_o$ . Thus effectively accumulated stress is proportional to  $\exp[2\sqrt{f_s} - (1-W/L)Wi^{-1}]$ . Because the solid area fraction and period on the nanocone surface is the smallest, the fluid elements travel almost 300 periods of alternating stress growth and

relaxation to make for a period equal to the micropost surface. Due to an accumulation of strain over multiple cycles, the polymer coils near the surface are stretched out. However, in comparison to a smooth surface, where polymer coils are in state of constant stretch, the textured surfaces can afford a lower overall stretching due to periodic relaxation afforded by stick-slip flow.

#### 4.3.4 Drop Impact Dynamics Diagram

As we discussed in the previous section, the Oldroyd-B model can show that the accumulated stress growth in viscoelastic drops is critically dependent on the texture ( $\sqrt{f_s}$ ) as well as on flow strength and fluid elasticity ( $Wi$ ). In other words, rebound can be suppressed when either  $Wi$  or  $\sqrt{f_s}$  is large. We can identify a drop impact dynamics diagram bound by topographical factor  $\sqrt{f_s(L-W)/D_o}$  and by  $Wi$  to represent distinct regions for rebound and deposition, as shown in Figure 4-4. The two regions are separated by a transition region, where partial rebounds are often observed. In addition to the accumulated stress growth discussion, to understand aqueous drop rebound and deposition on textured hydrophobic surfaces, we also need to consider that for textured surfaces the Cassie-Baxter state is not stable (impalement occurs) for  $We^{0.5} \sqrt{L^2/HD_o} > 1$ . Recalling  $Wi = We^{0.5} De$ , and by combining the impalement criteria with extensional stress criteria based on the Oldroyd-B model, we can also demonstrate that magnitude of  $Wi f_s^{1/2} (L^2/HD_o)^{1/2}$  demarcates drop impact outcomes where both impalement and viscoelastic effects are at play.

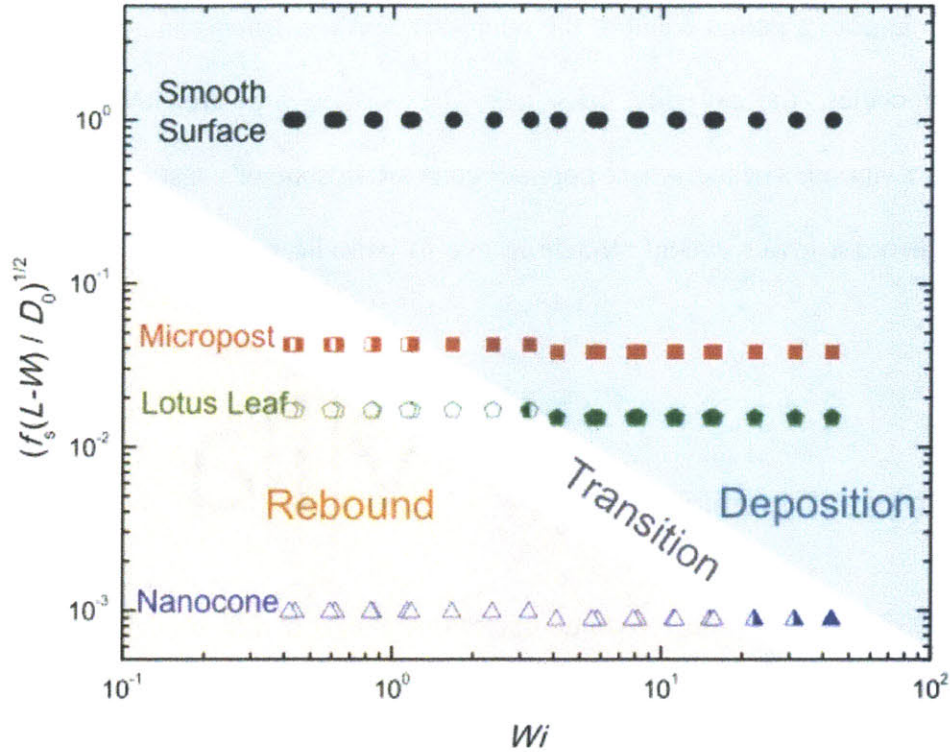


**Figure 4-4** A drop impact dynamics diagram that shows bouncing and deposition. This diagram is constructed based on two essential dimensionless parameters: (1) elasticity ( $Wi$ ) and (2) surface characteristics (determined by details of the texture). Deposition, full rebound and partial rebound are shown using filled, open and half-filled symbols, respectively. The diagram includes a hydrophobic surface smooth silanized glass (SS) and three canonical examples of superhydrophobic textured surfaces: micropost (MP), nanocone (NC) and lotus leaf (LL).

Based on the rationalization, we selected  $\sqrt{f_s(L-W)/D_o}$  similar to  $\sqrt{f_s(L^2/HD_o)}$  for the dimensionless topographical parameter, as (a) the former provides the simplest estimate of surface characteristics and (b) for agricultural sprays, changing the crop type, for example, would be captured by a change in this parameter. Using the drop impact dynamics diagram (Figure 4-4), the formulation used for spraying insecticides can be then designed to maximize deposition by the use of minimal chemicals. Conversely, if the chemical composition and distribution in

drop size and velocities of drops in the sprays are known, protective clothing or coatings that resist toxic aqueous complex liquids could be designed.

#### 4.4 Conclusion

In conclusion, we showed that the drop impact of complex fluids on natural and artificial surfaces could lead to a complete rebound. We developed a useful drop impact dynamics diagram to identify the drop impact outcomes for complex fluids impacting textured superhydrophobic surfaces. We showed that increasing solid area fraction and increasing elasticity both move us from a region of complete rebound to complete deposition. Most importantly, the answer "to bounce or not to bounce" for drops impacting textured surface thus depends upon topological features of a superhydrophobic surface, as well as flow strength (set by impact velocity and relaxation time). While the drop impact dynamics diagram provides a simple way of designing agricultural sprays depending upon the plant type, we expect our results will enable better control over drop deposition in a broad range of applications including inkjet printing and spray coating.

## References

1. Calvert, P. Inkjet Printing for Materials and Devices. *Chemistry of Materials* **2001**, *13*, 3299-3305.
2. Derby, B. Inkjet Printing of Functional and Structural Materials: Fluid Property Requirements, Feature Stability, and Resolution. *Annu. Rev. Mater. Res.* **2010**, *40*, 395-414.
3. Perelaer, J. *et al.* The Spreading of Inkjet-Printed Droplets with Varying Polymer Molar Mass on a Dry Solid Substrate. *Macromolecular Chemistry and Physics* **2009**, *210*, 495-502.
4. Wirth, W.; Storp, S.; Jacobsen, W. Mechanism Controlling Leaf Retention of Agricultural Spray Solutions. *Pestic. Sci.* **1991**, *33*, 411-420.
5. Bergeron, V., Bonn, D., Martin, J. Y. & Vovelle, L. Controlling Droplet Deposition with Polymer Additives. *Nature* **2000**, *405*, 772-775.
6. Bartolo, D.; Boudaoud, A.; Narcy, G.; Bonn, D. Dynamics of Non-Newtonian Droplets. *Phys. Rev. Lett.* **2007**, *99*, 174502.
7. Smith, M. I.; Bertola, V. Effect of Polymer Additives on the Wetting of Impacting Droplets. *Phys. Rev. Lett.* **2010**, *104*, 154502.
8. Smith, M. I.; Bertola, V. Particle Velocimetry inside Newtonian and Non-Newtonian Droplets Impacting a Hydrophobic Surface. *Experiments in Fluids* **2011**, *50*, 1385-1391.
9. Worthington, A. M. *A Study of Splashes*. (Longmans, Green, and Co., 1908).
10. Yarin, A. L. Drop Impact Dynamics: Splashing, Spreading, Receding, Bouncing. *Annual Rev. of Fluid Mech.* **2006**, *38*, 159-192.
11. Marengo, M.; Antonini, C.; Roisman, I. V.; Tropea, C. Drop Collisions with Simple and Complex Surfaces. *Current Opinion in Colloid & Interface Science* **2011**, *16*, 292-302.
12. Rein, M. Phenomena of Liquid Drop Impact on Solid and Liquid Surfaces. *Fluid Dynamics Research* **1993**, *12*, 61-93.
13. Lesser, M. Analytic Solutions of Liquid-Drop Impact Problems. *Proc. R. Soc. A* **1981**, *377*, 289-308.
14. Deng, T.; Varanasi, K. K.; Hsu, M.; Bhate, N.; Keimel, C.; Stein, J.; Blohm, M. Nonwetting of Impinging Droplets on Textured Surfaces, *Appl. Phys. Lett.* **2009**, *94*, 133109.

15. Bhushan, B.; Jung, Y. C.; Koch, K. Micro-, Nano- and Hierarchical Structures for Superhydrophobicity, Self Cleaning, and Low Adhesion. *Philos. Trans. R. Soc., A* **2009**, *367*, 1631-1672.
16. Reyssat, M.; Richard, D.; Clanet, C.; Quéré, D. Dynamical superhydrophobicity. *Faraday Discuss.* **2010**, *146*, 19-33.
17. Cassie, A. B. D.; Baxter, S. Wettability of Porous Surfaces. *Trans. Faraday Soc.* **1944**, *40*, 0546-0550.
18. Wenzel, R. N. Resistance of Solid Surfaces to Wetting by Water. *Ind. Eng. Chem.* **1936**, *28*, 988-994.
19. Larson, R. G. *The Structure and Rheology of Complex Fluids*. (Oxford University Press, 1999).
20. Tirtaatmadja, V.; McKinley, G. H.; Cooper-White, J. J. Drop Formation and Breakup of Low Viscosity Elastic Fluids: Effects of Molecular Weight and Concentration. *Phys. Fluids* **2006**, *18*, 043101.
21. Scott, T. P. Contraction/Expansion Flow of Dilute Elastic Solutions in Microchannels. *Massachusetts Institute of Technology, MS Thesis*, 2004.
22. McKinley, G. H.; Tripathi, A. How to Extract the Newtonian Viscosity from Capillary Breakup Measurements in a Filament Rheometer. *J. Rheol.* **2000**, *44*, 653-670.
23. Petrie, C. J. S. *Elongational Flows*. (Pitman, 1979).
24. Rozhkov, A., Prunet-Foch, B.; Vignes-Adler, M. Impact of Drops of Polymer Solutions on Small Targets. *Physics of Fluids* **2003**, *15*, 2006.
25. Bertola, V. An Experimental Study of Bouncing Leidenfrost Drops: Comparison between Newtonian and Viscoelastic Liquids. *International Journal of Heat and Mass Transfer* **2009**, *52*, 1786-1793.
26. Mani, M.; Mandre, S.; Brenner, M. P. Events before Droplet Splashing on a Solid Surface. *J. Fluid Mech.* **2010**, *647*, 163.
27. Driscoll, M. M.; Nagel, S. R. Ultrafast Interference Imaging of Air in Splashing Dynamics. *Phys. Rev. Lett.* **2011**, *107*, 154502.
28. Kolinski, J. M. *et al.* Skating on a Film of Air: Drops Impacting on a Surface. *Phys. Rev. Lett.* **2012**, *108*, 74503.
29. Clanet, C.; Béguin, C.; Richard, D.; Quéré, D. Maximal Deformation of an Impacting Drop. *J. Fluid Mech.* **2004**, *517*, 199-208.

30. Ybert, C.; Barentin, C.; Cottin-Bizonne, C.; Joseph, P.; Bocquet, L. Achieving Large Slip with Superhydrophobic Surfaces: Scaling :Laws for Generic Geometries. *Phys. Fluids* **2007**, *19*, 123601.
31. Tao, S. L.; Popat, K.; Desai, T. A. Off-Wafer Fabrication and Surface Modification of Asymmetric 3D SU-8 Microparticles. *Nat. Protoc.* **2006**, *1*, 3153-3158.
32. Reyssat, M.; Pepin, A.; Marty, F.; Chen, Y.; Quéré, D. Bouncing Transitions on Microtextured Materials. *Europhys. Lett.* **2006**, *74*, 306.
33. Jung, Y. C.; Bhushan, B. Dynamic Effects of Bouncing Water Droplets on Superhydrophobic Surfaces. *Langmuir* **2008**, *24*, 6262-6269.
34. Park, K.-C. *et al.* Nanotextured Silica Surfaces with Robust Superhydrophobicity and Omnidirectional Broadband Supertransmissivity. *ACS nano* **2012**, *6*, 3789-3799.
35. Jung, S.; Hoath, S. D.; Hutchings, I. M. The Role of Viscoelasticity in Drop Impact and Spreading for Inkjet Printing of Polymer Solution on a Wettable Surface. *Microfluidics and Nanofluidics* **2013**, *14*, 163-169.
36. Oldroyd, J. G. On the Formation of Rheological Equations of State. *Proc. Roy. Soc. A* **1950**, *200*, 523-541.



# **CHAPTER 5**

## **5. Fog Harvesting Mesh Surfaces**

## 5.1 Introduction and Theory

### 5.1.1 Fog as a promising water source in arid and mountainous regions

According to a recent UN water crisis report by the Food and Agriculture Organization<sup>1</sup> “fog collection technology appears to be an extremely promising and low-cost water harvesting system for drinking water, crop irrigation, livestock beverage and forest restoration in dryland mountains.” The UN authors go on to note that the growing global water crisis is a major issue threatening more than 2 billion people in arid regions. To recognize the significance of the water crisis, the UN declared the period 2005-2015 as International Decade for Action “Water for Life” and UNESCO recently launched the International Year for Water Cooperation 2013. As one part of the solution to the water crisis, fog harvesting has already been successfully demonstrated in the field in more than 17 countries over recent decades.<sup>2-8</sup>

Fog is an untapped resource for water, and water produced from fog has the potential to alleviate water scarcity in dry but foggy parts of the world. Fog harvesting provides an opportunity to collect water locally for rural communities, which will reduce the stress on groundwater. Consider a country like Chile, due to its long and mountainous coastline, a persistent advection fog is observed. Many research groups have assessed the potential to harvest fog in different parts of the world and many pilot projects to capture fog have been carried out.<sup>2-8</sup> A woven mesh surface of 1m<sup>2</sup> area, called a Standard Fog Collector (SFC) was typically used to quantify fog collection in these areas.<sup>6</sup> Water collection rates from as low as 0.1 L/m<sup>2</sup>/day to as high as 70 L/m<sup>2</sup>/day have been reported at various locations in these studies.<sup>3</sup>

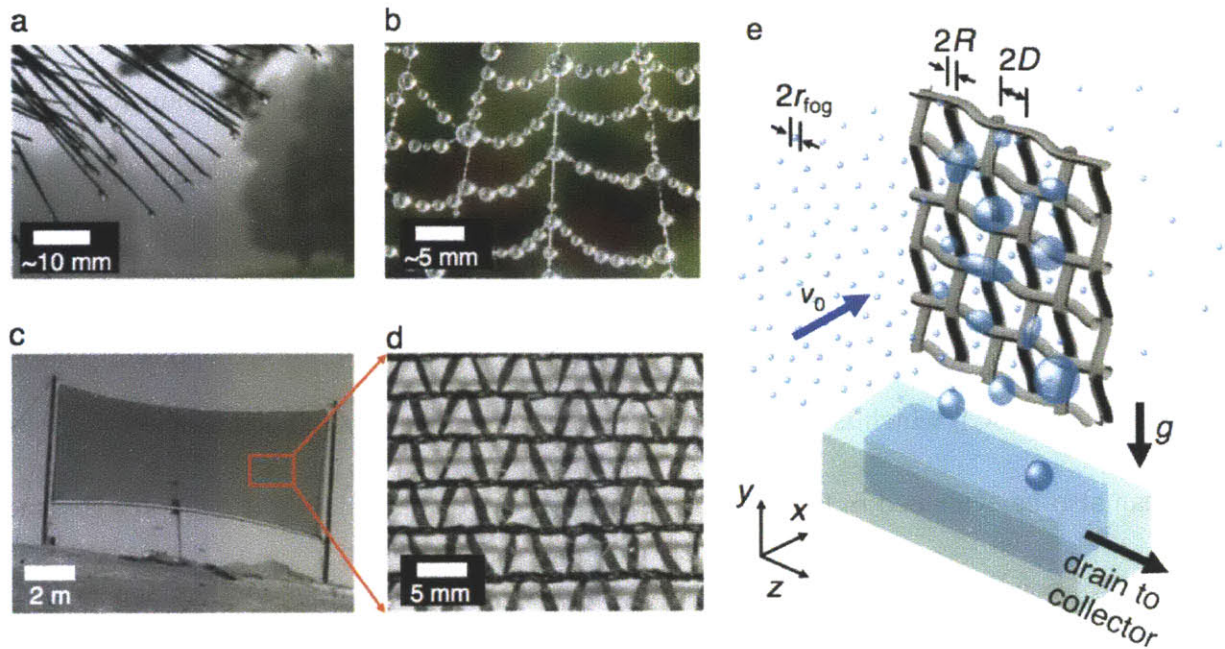


**Figure 5-1** Natural and artificial examples of fog harvesting surfaces. (a) Slender leaves of trees (Image courtesy Robert Holmes). (b) A spider web decorated with droplets of water collected from fog (Image courtesy William Lee). (c) A large area man-made fog collector deployed in the Atacama Desert of Chile (4) and (d) triangular weave of the Raschel Mesh used in Large Fog Collector. (e) The basic mechanism of fog collection by physical impaction of droplets on the mesh, collection of larger coalesced droplets, and subsequent drainage.

The fog harvesting capability of plants and animals have been studied extensively (Figure 5-1a, b).<sup>9-17</sup> The Namib desert beetle (*Stenocara gracilipes*) survives by drinking fog water that it collects on its wing case.<sup>10, 15</sup> A grass (*Stipagrostis sabulicola*) in the same region employs an anisotropic microstructure on its thin long leaves to direct water droplets towards its roots.<sup>16</sup> Tree canopies with slender leaves also harvest water from fog.<sup>11-13</sup> Sticky spider webs<sup>17, 18</sup> decorated with tiny water droplets collected from morning fog are a common sight (Figure 5-1b).<sup>19</sup>

### 5.1.2 Aerodynamic Efficiency and Deposition Efficiency

We introduce two dimensionless geometric groups to facilitate the mechanistic analysis of fog harvesting behavior: i) the ratio of the radius of fog droplets ( $r_{fog}$ ) to the radius of the mesh wire ( $R$ ); denoted  $R^* = r_{fog}/R$  and ii) a spacing ratio denoted  $D^* = (R + D)/R$  (see Figure 5-1e, 2a, b), which measures the relative openness of the weave. The more commonly reported shade coefficient ( $SC$ ), which is the fraction of projected area that is occluded by the solid mesh fibers, can also be evaluated in terms of  $D^*$  as  $SC = 2/D^*(1 - 1/2D^*)$ . We use the design space (Figure 5-2c) constructed from these two parameters to identify various meshes and evaluate their fog collection efficiencies  $\eta(R^*, D^*)$  using droplet impact models proposed by Langmuir and Blodgett,<sup>28</sup> and more recently by Rivera.<sup>4</sup>

As shown in Figure 5-1e and Figure 5-2a, when fog droplets convected with a uniform velocity  $v_0$  approach the vertical mesh surface, some of the droplets collide with the mesh fibers and are subsequently deposited, whereas others pass through the void spaces between the wires (Figure 5-2b). Repeated collisions lead to continued deposition, followed by droplet coalescence and growth. When the volume of a pinned water droplet reaches a critical value sufficient for the gravitational force to overcome the integrated line forces at the liquid-solid interface, the water droplet flows down along the mesh and is ultimately collected in a container. The void spaces do not collect any droplets, but they decrease the overall wind resistance and therefore help to maintain a high droplet flux towards the mesh.

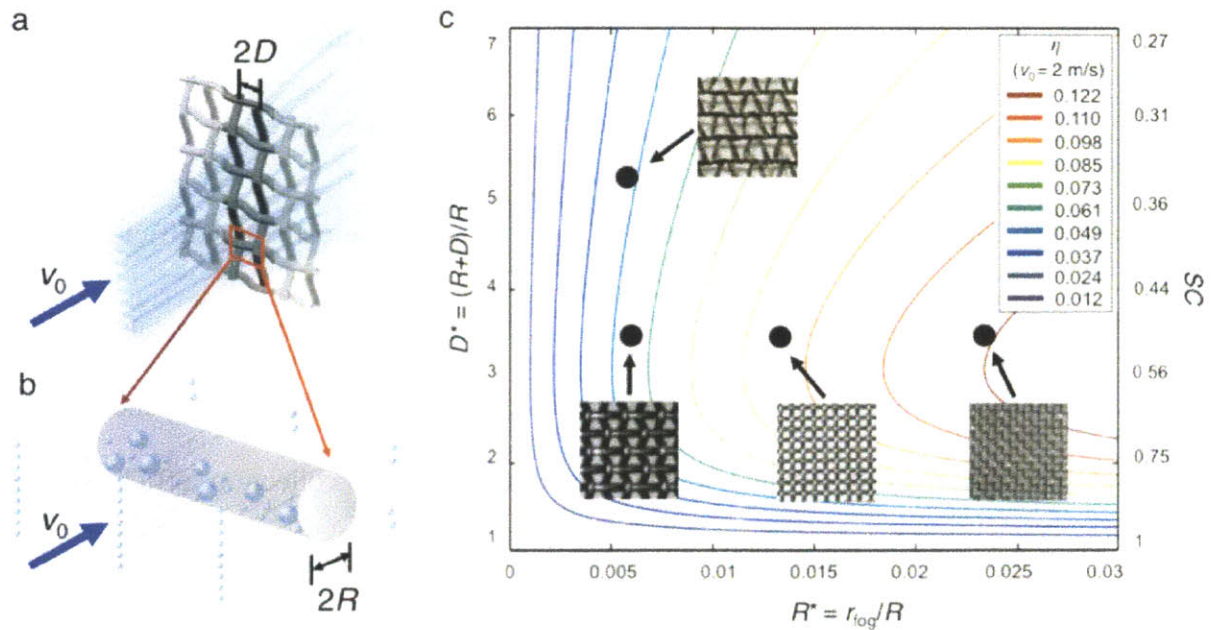


**Figure 5-2** Fog flow through a woven mesh surface, and a contour plot of the fog harvesting efficiency. (a) Illustration indicating the stream surfaces of fog laden wind and their divergence after passing through a woven mesh surface. (b) An enlarged picture focusing on the interaction between incoming fog droplets and a horizontal mesh element. Droplets that are closer to the central axis are trapped on the cylindrical wire, whereas droplets closer to the periphery follow the streamline around the wire. Droplets on the wire coalesce, and once they grow past a threshold size, they drain under gravity. (c) A contour plot of the fog harvesting efficiency ( $\eta$ ) as a function of the ratio of radius of the fog droplets to the radius of the wire ( $R^* = r_{fog}/R$ ) and the spacing ratio of the woven mesh ( $D^* = (R+D)/R$ ). The location of various mesh surfaces and corresponding predicted efficiencies are highlighted on the design chart.

The overall collection efficiency is a product of i) the aerodynamic collection efficiency ( $\eta_a$ ) and ii) the subsequent deposition efficiency ( $\eta_d$ ).<sup>4</sup> Rivera argued that the aerodynamic collection efficiency accounts for the fraction of fog flow that is directed towards the solid portion of the mesh. The high Reynolds number ( $Re \gg 1$ ) flow of moist air around the porous mesh (Figure 5-2a) is modeled as a linear combination of the flow around an impermeable rigid solid (*i.e.*  $D^* = 1$ ), and an unobstructed uniform flow.<sup>4</sup> Due to the no slip and no penetration boundary conditions at the solid surface, the wind speed is locally reduced in the vicinity of the

individual mesh elements. This momentum deficit is modeled in terms of an appropriate drag coefficient for the overall structure ( $C_D \approx 1.18$ )<sup>4</sup> and the aerodynamic collection efficiency is ultimately expressed as  $\eta_a = SC / (1 + \sqrt{C_0/C_D})$ , where  $C_0$  is the pressure drop coefficient for a cylindrical mesh<sup>4</sup> given as  $C_0 = 1.44 \left[ 1.3SC + (SC/(1-SC))^2 \right]$ . The collection efficiency is not simply equal to the shade coefficient of the mesh, but changes nonmonotonically with the openness of the mesh and the aerodynamic characteristics of the flow through the mesh. As  $D^*$  increases from unity (an impermeable plate), the aerodynamic collection efficiency ( $\eta_a$ ) increases from zero as the lateral deflection of the air stream is diminished. There is a local maximum in the aerodynamic efficiency at  $D_{crit}^* \approx 3.1$  (or equivalently,  $SC \approx 0.55$ ), and beyond this point most fog droplets pass through the void area between wires without being deflected, consequently  $\eta_a$  decreases for large values of  $D^* \gg 1$ .<sup>4</sup>

The deposition efficiency ( $\eta_d$ ) quantifies the fraction of fog droplets that are actually deposited from the population initially headed towards the solid wires. In their seminal work, Langmuir and Blodgett used numerical calculations to develop an empirical correlation for the deposition of small particles on an infinitely long cylinder.<sup>28</sup> They found that the deposition efficiency could be described well by an empirical expression ( $\eta_d \approx St / (St + \pi/2)$ ), where  $St$  is the Stokes number. This expression monotonically increases as the dimensionless radius ratio  $R^*$  increases, *i.e.* cylinders with progressively smaller radii are more efficient collectors.

The resultant overall collection efficiency from the two contributions can therefore be expressed in the following expression.

$$\eta = \eta_a(D^*)\eta_d(R^*) = \left[ \frac{SC}{1 + \sqrt{C_0/C_D}} \right] \left[ \frac{St}{St + \pi/2} \right] \quad (5-1)$$

This function is plotted in Figure 5-2c as a contour map in  $R^*, D^*$  parameter space, assuming a wind velocity of 2 m/s and uniform droplet size  $r_{fog} \approx 3 \mu\text{m}$ , (corresponding to  $0 \leq St \leq 4$ ). The contours indicate that the collection efficiency of a conventional Raschel mesh (with coordinates corresponding to  $D^* \approx 5.1$ ,  $R^* \approx 0.005$ , and an efficiency  $\eta \approx 4.8\%$ ) is much lower than that of a thinner and denser wire mesh (corresponding to  $D^* \approx 3.5$ ,  $R^* \approx 0.024$ ,  $\eta \approx 12\%$ ). The contour map can also be used as a design chart for selecting an optimal mesh by selecting a specified value of  $D^*$  (or  $SC$ ) and then maximizing  $R^*$ . Our chart can be employed to estimate the maximum fog collection efficiency and evaluate the amount of collected water expected for a specific mesh surface, if the characteristic wind speed of the fog ( $v_0$ ), liquid water content, total mesh area, and collection time are known.

It is clear from Figure 5-2c that Raschel mesh is far from the optimal mesh design for high fog collection rates. The efficiency of a square planar mesh can be increased to about 5.5%, by optimizing the effective mesh opening  $D^*$  using multiple overlapping layers of meshes for example. However, for a given value of  $r_{fog}$ , further gains in efficiency are possible only by using meshes with smaller wire radii  $R$  (to achieve higher values of  $R^*$ ).

## 5.2 Materials and Methods

### 5.2.1 Preparation of Mesh Surfaces

Raschel mesh samples with 35% shade coefficient were procured from Fogquest volunteers in Chile and were cut into 30 mm by 30 mm pieces. To keep the Raschel mesh flat and to ensure that the meshes are normal to the direction of fog stream, the three edges of square planar mesh were supported by a metal wire frame with diameter of 127  $\mu\text{m}$ . Sample wire mesh surfaces were prepared by cutting commercially available wire meshes (McMaster-Carr, Corrosion-Resistant Type 304 Stainless Steel Woven Wire Cloth) into the same square planar shape with 30 mm side.

### 5.2.2 Coating Materials

Polyolefin emulant coating (denoted by PO)

When comparing the performance of the Raschel and wire meshes, it is important to note that both the surface chemistry and the physical geometry are different. To enable us to investigate the effect of each variable independently it is thus desirable to develop a coating for the mesh that can emulate the properties of a polyolefin surface. We have previously shown that by tuning the relative concentration of the FluoroPOSS species and a compatible polymer binder (*e.g.* PEMA) we can tune the wettability characteristics of a dip-coated surface over a wide



range.<sup>23</sup> In order to generate a coated wire mesh that closely mimics the surface properties of the polyolefin Raschel mesh, the as-received wire mesh was dip-coated using a 1.7 wt.% 1H,1H,2H,2H-heptadecafluorodecyl polyhedral oligomeric silsesquioxane (fluorodecyl POSS) 98.3 wt.% poly(ethyl methacrylate) (PEMA,  $M_w = 515$  kDa, Sigma Aldrich) solution in a volatile hydrochlorofluorocarbon solvent (Asahiklin AK-225, Asahi Glass Company) at a concentration of 10 mg/mL. The meshes were dipped for 5 minutes, and then air-dried to evaporate the solvent. Uniformity of the coating was checked by scanning electron microscope (SEM) and by contact angle measurements at multiple locations on the surface.

#### POSS-PEMA dipcoating (denoted by PPD)

Mesh samples were dip-coated using a 50 wt.% fluorodecyl POSS / 50 wt.% PEMA solution in Asahiklin at a concentration of 10 mg/mL. The meshes were dipped for 5 minutes, and then air-dried to evaporate the solvent, resulting in a smooth hydrophobic coating.

#### POSS-PEMA spraycoating (denoted by PPS)

A 50 wt.% fluorodecyl POSS 50 wt.% PEMA solution was prepared in Asahiklin at a concentration of 50 mg/mL. The superhydrophobic spray-coated meshes were prepared by spray deposition of the polymer solution using an air spray-brush (McMaster-Carr) using a pressurized nitrogen stream to produce a re-entrant microtexture with very low contact angle hysteresis.<sup>24</sup> A representative micrograph of the spray-coated mesh is shown in Figure 5-8 (Appendix A).

Liquid Impregnated surfaces (denoted by KO)

The spray-coated meshes were immersed into nonvolatile Krytox oil ( $\gamma_{LV} = 17$  mN/m at 25°C,  $\mu \approx 113$  mPa·s at 20°C, DuPont) using a DCAT 11 (DataPhysics Instruments) tensiometer at a rate of 0.5 mm/min and then retracted at the same speed. A thin film of fluorinated Krytox oil remains imbibed into the porous spraycoated texture after the mesh is completely withdrawn from the oil bath, resulting in a “SLIPS” surface with very low contact angle hysteresis.<sup>25-27</sup>

### 5.2.3 Experimental Setup in a Humidity Control Chamber

All fog collection experiments were performed at a relative humidity of  $RH = 100\%$  and temperature of  $26.4 \pm 0.5^\circ\text{C}$  in a controlled-humidity glove box (environmental chamber, Electro-Tech Systems, Inc.) to eliminate complications resulting from evaporation and condensation. Each sample was positioned 10 mm in front of the end of two plastic concentric cylinders with different diameters of 100 mm and 30 mm, respectively. As shown in Figure 5-9 (Appendix B), fog droplets ( $r_{fog} = 3 \mu\text{m}$ ) created from a nebulizer (Omron Compair XLT Nebulizer Compressor Kit NE-C25,  $\dot{Q} = 16$  mL/hr) were convected towards the mesh sample by a wind stream of velocity  $v_0 \approx 2$  m/s, generated by a speed-tunable fan (Thermaltake Mobile Fan II External USB Cooling Fan). The concentric axis of the two cylinders and axes of symmetry of meshes and container were aligned to be on the same vertical plane. The mass of water collected in the container with dimension of 50 mm by 50 mm that was located 50 mm under the mesh

samples was measured every hour for Raschel meshes and every 30 minutes for wire woven meshes to quantify the time evolution of the collection efficiency. Once the efficiency reached a steady asymptotic value, the readings from at least three consecutive experiments were averaged to calculate the fog collection efficiency.

## 5.3 Results and Discussion

### 5.3.1 Two Major Practical Problems of Fog-collection

The theoretical collection efficiency anticipated from this design framework for meshes can be adversely affected in actual performance due to two issues that depend on the surface wettability; i) convective loss of deposited droplets (or *re-entrainment*); as shown schematically in Figure 5-3a) and ii) clogging of the mesh with pinned droplets that modifies the local aerodynamics (Figure 5-3b).

Re-entrainment arises from aerodynamically-induced detachment of deposited water droplets back into the air stream before they can reach the critical volume at which gravitational drainage dominates. As the small deposited water droplets coalesce, the growing droplets are influenced by the competition between aerodynamic drag forces and surface adhesion forces.<sup>29,30</sup> When  $F_{drag} > F_{adhesion}$ , the droplets are re-entrained in the fog flow, leading to a decrease in the fog collection efficiency (Figure 5-3a).

In Figure 5-3b we identify a second problem that occurs on a mesh when the deposited liquid volume becomes large. In the clogging region, the hysteretic wetting force pinning a

droplet in the interstices of the mesh exceeds the gravitational draining force when the deposited water droplet size is less than a critical volume. The void area between mesh elements could become occluded by these pinned (non-draining) drops, depending on the half spacing of the mesh as discussed below. Such clogged parts of the mesh are impermeable and obstruct the local wind, significantly hampering the overall fog-harvesting ability of the grid. The effective void fraction approaches zero (or  $D_{effective}^* \rightarrow 1$ ) as the mesh clogs and the aerodynamic collection becomes zero.

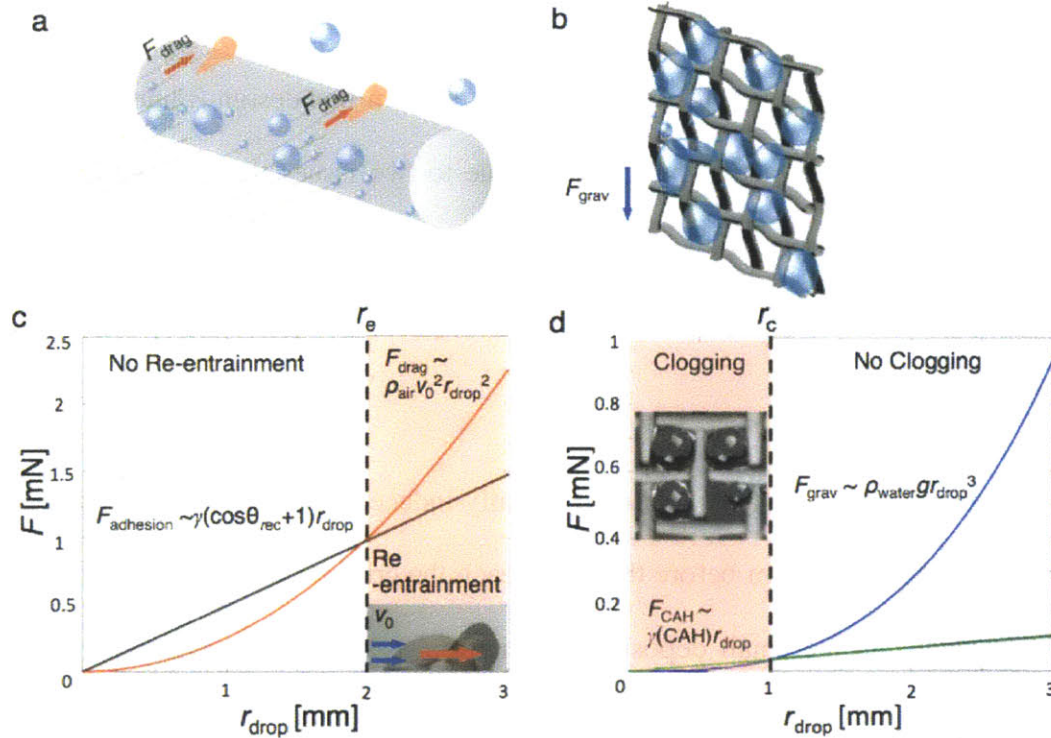


**Figure 5-3** Two factors that reduce collection efficiency, and the surface modification design space that depicts the relative resistance to re-entrainment and drainage. Two factors that inhibit fog harvesting and reduce collection efficiency are (a) re-entrainment of collected droplets in the wind and (b) blockage of the mesh. (c) The plot identifies the range of droplet sizes where the forces of adhesion dominate the drag forces, and establishes a criterion for a threshold droplet size for re-entrainment. (d) A second constraint arises from comparing the weight of the droplet with the surface pinning force arising from contact angle hysteresis. The threshold size where gravity dominates hysteretic pinning can be decreased by minimizing  $CAH = \cos\theta_{rec} - \cos\theta_{adv}$ .

To overcome these two challenges and to design fog collection mesh surfaces with high efficiency in practice, we consider the two critical water drop radii - denoted  $r_e$  and  $r_c$  in Figure 5-3c, d - that are sensitive to the physico-chemical surface properties of the meshes. In Figure 5-3c, the right-most shaded region represents the range of parameter space where the aerodynamic drag force (which grows as  $F_{drag} \approx \rho_{air} v_0^2 r_{drop}^2$  exceeds the adhesion force (which grows as  $F_{adhesion} \approx \gamma_{LV} (1 + \cos \theta_{rec}) r_{drop}$  ; droplet re-entrainment is expected in this region where  $F_{drag} > F_{adhesion}$  . A detailed force balance on a spherical cap gives a critical droplet radius at which these two forces balance each other:

$$r_e = 4\pi\gamma_{LV} \sin^2 \theta (1 + \cos \theta_{rec}) / \rho_{air} v_0^2 C_D (\theta - \sin \theta \cos \theta) \quad (5-2)$$

where  $\gamma_{LV}$  is the surface tension of water,  $\theta = (\theta_{adv} + \theta_{rec})/2$  is the mean contact angle of the droplet on the surface, and  $\theta_{adv}$ ,  $\theta_{rec}$  are the advancing contact angle and receding contact angle, respectively, (see Supporting Information for details). A droplet with radius  $r_{drop} > r_e$  is susceptible to re-entrainment. To reduce re-entrainment, the slope of the adhesion force curve, which is proportional to the work of adhesion  $\gamma_{LV} (1 + \cos \theta_{rec})$ , must be increased. This can be achieved in practice by lowering the receding contact angle  $\theta_{rec}$  .

As the droplets grow on the mesh, gravity has to overcome the surface pinning force in order to shed these collected droplets into the collecting gutter at the base of the mesh. Balancing the gravitational body force  $F_{grav} \approx \rho_{water} g r_{drop}^3$  with the hysteretic force  $F_{CAH} \approx \gamma_{LV} (CAH) r_{drop}$  , where  $CAH = \cos \theta_{rec} - \cos \theta_{adv}$  , that characterizes depinning of a liquid droplet in the interstitial

gap of a woven mesh with a simple square weave. Setting  $F_{grav} = F_{CAH}$  gives a second critical radius for “choking” or clogging of the mesh

$$r_c = \sqrt{12\gamma_{LV}(\cos\theta_{rec} - \cos\theta_{adv}) / [\pi\rho_{water}gB(3 + B^2)]} \quad (5-3)$$

where  $B = (1 - \cos\theta) / \sin\theta$  (see Supporting Information for additional details). Figure 5-3d shows that the impact of mesh-clogging as a result of contact line pinning can be reduced (*i.e.* the minimum droplet size  $r_c$  that will freely drain off the mesh) by developing surface coatings with smaller values of the contact angle hysteresis  $CAH$ .

For an ideal fog-collecting surface, liquid droplets convected towards the mesh and deposited on the surface will be drained quickly by gravity into the collecting gutter without loss by re-entrainment to the airflow, thus refreshing the base mesh surface for capture of new fog droplets. Design of an improved mesh to maximize fog collection efficiency thus involves: I) minimizing  $r_c$  to avoid clogging, II) maximizing  $r_e$  to reduce re-entrainment, while also III) selecting a mesh opening near the optimal aerodynamic value of  $D^* \approx 3.1$  and IV) maximizing  $R^*$  to the extent possible.

### 5.3.2 Role of Surface Wettability

The surface forces controlling adhesion and hysteresis depend upon the physico-chemical surface characteristics of the mesh,<sup>31</sup> and therefore smart engineering of suitable coatings can enable woven meshes to collect fog with improved efficiency. If we can make  $r_e \gg r_c$  by surface modifications, then the performance degradation associated with both shaded

regions in Figure 5-3c,d can be minimized. Such a mesh surface would have both low contact angle hysteresis ( $CAH \ll 1$ ) and a low receding contact angle ( $\theta_{rec} \rightarrow 0$ ). This material challenge can be summarized in the surface modification design space shown in Figure 5-4. The two important design parameters are contact angle hysteresis ( $CAH$ ) and a scaled work of adhesion ( $W_a/\gamma_{LV} = 1 + \cos\theta_{rec}$ ) that can be exploited to rank the wetting properties of various materials for preventing clogging and re-entrainment problems. From the expression for mesh clogging ( $r_c$ ) given in Eq. 5-3, it is clear that a coating with extremely low hysteresis ( $CAH \rightarrow 0$ ) will lead to a small value of the critical mesh half spacing (denoted  $D_{crit}$ ) above which the clogging problem does not occur.

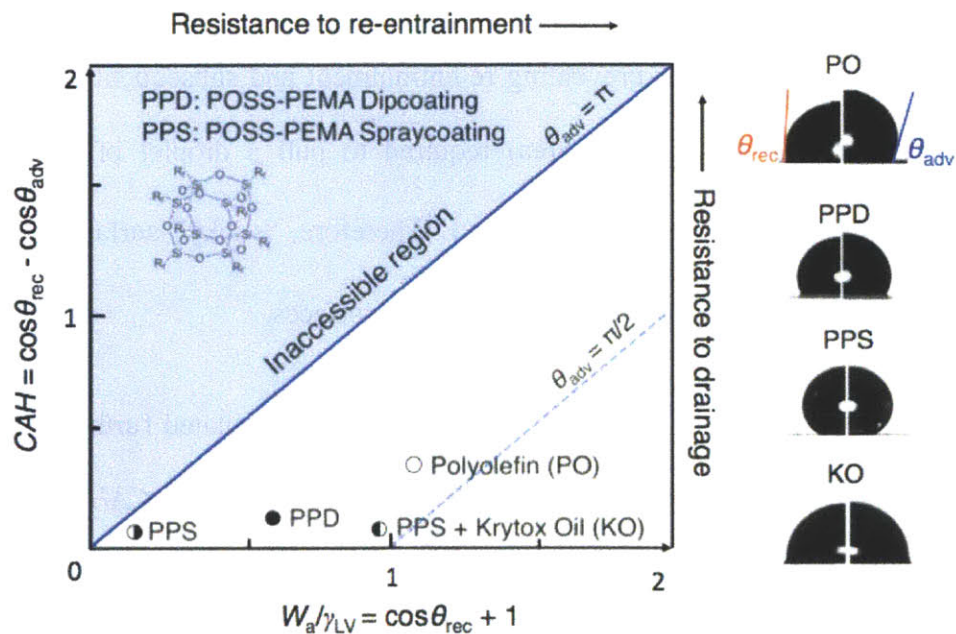


**Figure 5-4** The design space constructed from two dimensionless parameters related to work of adhesion (abscissa) and contact angle hysteresis (ordinate) depicts the relative resistance to re-entrainment and drainage. Measured values for droplets of water ( $V \approx 10 \mu\text{L}$ ) deposited on several different coatings are shown in the plot. Wetting characteristics corresponding to a higher work of adhesion and lower contact angle hysteresis are ideal for the maximum fog collection efficiency.

Previously deployed fog harvesting setups used a double-layered Raschel mesh made of polyolefin (denoted PO) which we measure to have  $CAH^{(PO)} = \cos\theta_{rec}^{(PO)} - \cos\theta_{adv}^{(PO)} \approx 0.40$  (see Table 5-1 in Appendix A). By contrast, a topographically smooth surface dipcoated with a blend of 50% POSS - 50% PEMA (denoted PPD) has one of the lowest values of contact angle hysteresis reported to date;  $CAH^{(PPD)} = \cos\theta_{rec}^{(PPD)} - \cos\theta_{adv}^{(PPD)} \approx 0.06$ .<sup>23</sup> The critical opening size for a PPD coated mesh  $D_{crit}^{(PPD)} \approx 0.41$  mm is significantly smaller than  $D_{crit}^{(PO)} \approx 1.5$  mm, and therefore finer meshes, if dipcoated with POSS-PEMA, will drain more readily and be less susceptible to clogging.

This hysteretic drainage criterion involves differences in the surface energies for wetting/dewetting; however, from Eq. 5-2 it is clear that the absolute magnitude of the receding contact angle is also important for preventing re-entrainment and subsequent loss of deposited droplets. The adhesive work (per unit area) required to pull a droplet off the surface (by aerodynamic drag) scales as  $W_a = \gamma_{LV}(1 + \cos\theta_{rec})$ . Therefore, “sticky” surfaces with low  $\theta_{rec}$  (and high  $W_a$ ) promote the adhesion of droplets on solid surfaces.

The surface properties of our POSS coating can be manipulated further by altering the deposition technique (Figure 5-4). The  $CAH$  can be further decreased to  $CAH \approx 0.01$  by spray-coating the mesh to create a re-entrant roughened topography using POSS-PEMA<sup>24</sup> but the receding contact angle increases to  $\theta_{rec} \approx 159^\circ$ . Therefore, such spray coated meshes (denoted PPS in Figure 5-4) are extremely clogging-resistant, but the higher  $\theta_{rec}$  value reduces drop adhesion which leads to greater re-entrainment and a lower overall collection efficiency. A liquid impregnated textured surface or “SLIPS surface”<sup>25-27</sup> with low  $CAH$  and low  $\theta_{rec}$  can be



obtained by imbining a nonvolatile oil (*e.g.*, Krytox oil) into the pores of the spray-coated surface.<sup>27</sup> This liquid-impregnated surface (denoted KO in Figure 5-4) has  $CAH \approx 0.03$  and  $\theta_{rec} \approx 100^\circ$ , and therefore it is expected to harvest fog better than dip-coated or spray-coated meshes.

### 5.3.3 Combined Design Space and its Application as a Design Chart

Guided by this framework relating surface wettability and fog harvesting performance, we performed a set of parametric experiments using a family of simple woven meshes with a range of surface coatings (see Materials and Methods for details). We benchmarked our results against the canonical Raschel mesh, using an artificially generated laboratory fog. Our results are summarized in Figure 5-4 and Table 5-1 in Appendix. As shown in Table 5-1, for most coating materials ( $\cos\theta_{rec} \neq -1$ ),  $r_e \gg r_c$ , and  $r_e$  does not impact the fog collection efficiency. For a given fog condition (*i.e.*, fixed  $r_{fog}$ ) the critical mesh half spacing with a given coating to prevent the clogging and re-entrainment problems ( $r_c = D_{crit} < D < r_e$ ) can be represented as a line ( $D^* = (D/r_{fog})R^* + 1$ ) through the origin with positive slope  $D/r_{fog}$ . Therefore the high efficiency regions to the right of these lines are inaccessible due to clogging (*i.e.* in this region of Figure 5-5a the mesh openings are too small  $D < r_c$  and the clogged mesh grids become impermeable).

We first consider the polyolefin Raschel mesh (with large  $CAH$ , and a critical opening size  $D_{crit}^{(PO)} \approx 1.5$  mm). Because of the clogging constraint, large portions of the design space with

the highest efficiency cannot be accessed and, at best, a theoretical efficiency of 5% efficiency can be obtained. As shown in Figure 5-5b, the measured fog-harvesting efficiency of a Raschel mesh ( $D^* = 5.1$ ) was  $\eta \approx 2\%$ , under simulated fog conditions.

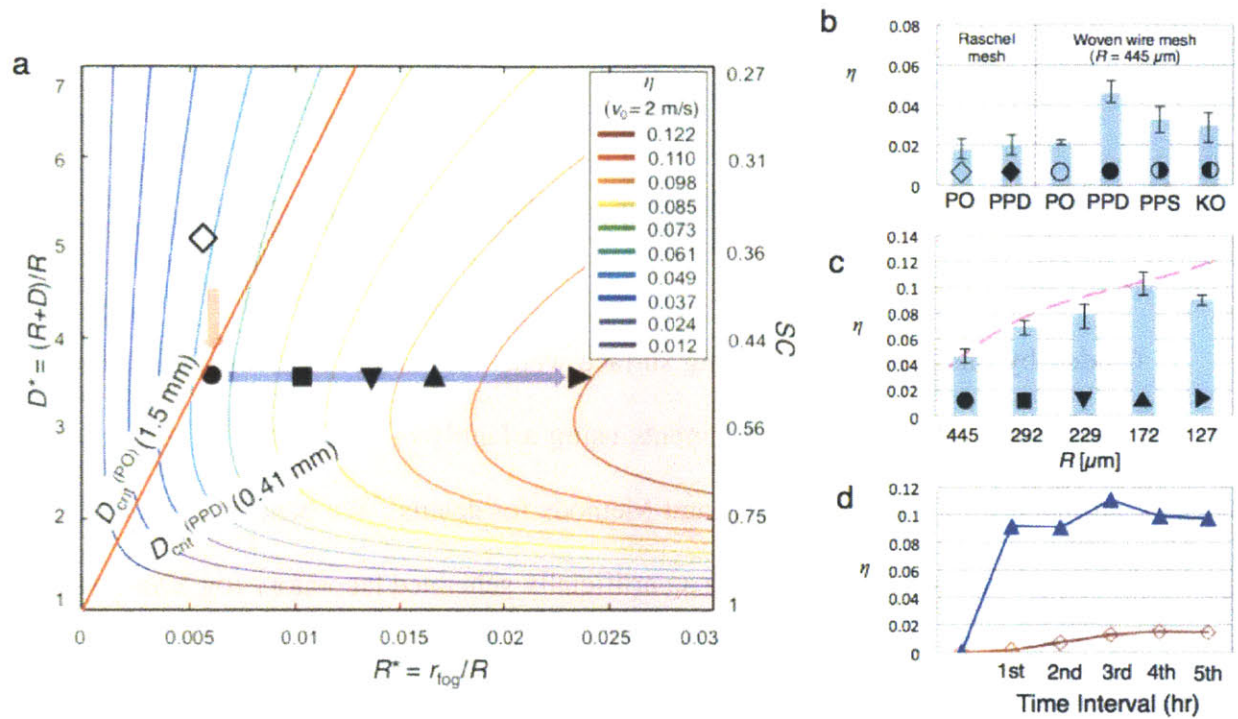


**Figure 5-5** Measured fog collection efficiency. The coordinates of various mesh surfaces tested in the laboratory are depicted on the design space in (a) and the measured fog-collecting efficiencies ( $N = 3$ ) are plotted in (b) and (c). At any point to the right of the critical lines shown for the polyolefin and POSS-PEMA coating in Figure 5-5a (*i.e.* any point in the shaded region with  $D < D_{crit}$ ), the mesh openings clog with liquid droplets and the fog harvesting efficiency deteriorates. (b) and (c) explore the role of the mesh coating and structure (*i.e.*, the individual fiber size  $R$  and the spacing  $D$ ). In (c) the theoretical efficiency is shown by a broken line. The measured fog collection efficiency increases monotonically as the radius of the wire mesh decreases from  $R \approx 445 \mu m$  ( $\bullet$ ) to  $R \approx 172 \mu m$  ( $\blacktriangle$ ), but decreases in the case of  $R \approx 127 \mu m$  ( $\blacktriangleright$ ) as we enter the drainage-limited zone on the design chart. The time evolution of the fog harvesting performance of the optimal wire mesh ( $\blacktriangle$ ) and the Raschel mesh is compared over many hours in (d). The optimal wire mesh ( $\blacktriangle$ ) collects more water and reaches a steady state faster than the Raschel mesh ( $\diamond$ ).

The locus of the conventional polyolefin Raschel mesh in the design space of Fig 5a is shown by the open diamond. Because it lies above the critical clogging line (*i.e.*,  $D_{Raschel} > D_{crit}^{(PO)} \approx 1.5 \text{ mm}$ ) it is not prone to clogging. Additional dipcoating of the Raschel mesh with a POSS-PEMA coating therefore does not appreciably enhance its fog collection performance (sample  $\blacklozenge$  shown in Fig 5b with  $\eta \approx 2 \pm 0.5\%$ ). To access the regions of higher efficiency, it is clear that meshes with higher  $R^*$  are required. Surfaces that are dipcoated in POSS-PEMA (to achieve smaller  $CAH$ ) have a lower critical opening size  $D_{crit}^{(PPD)} \approx 0.41 \text{ mm}$ , and therefore, a significantly higher fraction of the design space is free of clogging and drainage limitations. As a result, meshes that were previously unusable with thinner fibers (higher  $R^*$ ) and higher shade coefficients closer to the optimal value can now be employed for fog harvesting. These finer meshes are predicted to have much higher fog collection efficiencies ( $\eta \approx 12\%$ ), provided a suitable low hysteresis coating is applied.

In Figure 5-5b, we first explore the role of surface coating alone for a particular mesh geometry. The measured efficiency increases from  $\eta \approx 2\%$  (for a woven mesh that is dip-coated to achieve the same surface wettability characteristics as the polyolefin Raschel mesh) to  $\eta \approx 5\%$  for a POSS-PEMA dipcoated woven mesh (PPD,  $\bullet$ ) with the same radius  $R \approx 445 \mu\text{m}$  and the same shade coefficient  $SC \approx 0.5$  ( $D^* \approx 3.5$ ). However, the fog-collecting efficiency of a sprayed texture (PPS,  $\circ$ ) and liquid-impregnated surface (KO,  $\circ$ ) woven mesh (again with the same  $R \approx 445 \mu\text{m}$ ) do not perform as well as the dip-coated mesh due to the predominance of re-entrainment and clogging. Interaction with water droplets impacting and sliding along the Krytox-impregnated “SLIPS surface” results in a progressive loss of the nonvolatile impregnating liquid (see Figure 5-9 in Appendix B for details). This leads to increasing contact

angle hysteresis and the mesh openings start to clog. We therefore focus our optimization studies on the dip-coated surfaces as they tend to be stable over much longer timescales.

In Figure 5-5c, the fog-collecting efficiency is plotted against the wire radius, keeping the weave constant ( $D^* \approx 3.5$ ) with the same surface coating (dip-coated with POSS-PEMA). The theoretical fog collecting efficiency  $\eta(R^*, D^*)$  given by our analysis in Eq. 5-1 above (broken line) provides a good estimate of the observed trends. The measured efficiency increases monotonically from 5% to 10% as the fiber radius decreases from  $R = 445 \mu\text{m}$  to  $R = 172 \mu\text{m}$  for the first 4 meshes (●, ■, ▼, and ▲) that lie in the region of the design chart where clogging is not a limiting factor. However, the finest mesh ( $R \approx 172 \mu\text{m}$ , ►) is located inside the hysteresis-limited region (with mesh spacing  $D < D_{\text{crit}} = r_c$ ), and clogging once again prohibits any further increase in the efficiency. A mesh located in the clogging-prone region of the design space still collects an appreciable amount of fog, but its efficiency could be improved still further by reducing the clogging constraint imposed by Eq. 5-3 (*i.e.*, lowering the slope of the bounding line for  $D_{\text{crit}}$ , via lower values of  $CAH$ ).

The maximum fog harvesting efficiency observed in our experiments is  $\eta \approx 9.9 \pm 0.5\%$  (N=3) for a fine POSS-PEMA dipcoated mesh with close to optimal weave ( $R \approx 172 \mu\text{m}$ ,  $D^* \approx 3.5$ ,  $CAH \approx 0.06$ , ▲). In Figure 5-5d, the time evolution of the fog harvesting performance for the optimal mesh and the Raschel mesh is compared over many hours. The optimized wire mesh collects water at a faster rate and also reaches steady state faster than the Raschel mesh. Thus, by an appropriate choice of the surface texture and coating chemistry, the fog harvesting efficiency for representative fog conditions ( $v_0 = 2 \text{ m/s}$ ,  $r_{\text{fog}} \approx 3 \mu\text{m}$ ) has been enhanced approximately five-fold.

## 5.4 Conclusion

A comparison of theoretical fog collection efficiency across many fog conditions (see Supporting Information) indicates that the fog harvesting efficiency for the POSS-PEMA dipcoated wire mesh ( $R \approx 172 \mu\text{m}$ , ▲) is also more robust than the conventional Raschel mesh to changes in fog conditions ( $1 \leq r_{fog} \leq 40 \mu\text{m}$ ,  $1 \leq v_0 \leq 10 \text{ m/s}$ ). As a result, fog harvesting technology based on POSS-PEMA dipcoated woven meshes may be deployable in many regions of the world where the size and velocity of fog droplets are not suitable for traditional Raschel meshes to work well. The performance of these rapidly-draining woven meshes are less susceptible to daily or seasonal changes of wind speed and direction, or temperature. Optimally-engineered surfaces can work effectively in foggy conditions for longer periods of time, and subsequently produce much more water; even in a mild fog with droplet radius of  $3 \mu\text{m}$ , wind speed of  $2 \text{ m/s}$  and liquid water content of  $0.1 \text{ g/m}^3$ , the optimal mesh surface ( $R \approx 172 \mu\text{m}$ , ▲) can collect approximately two liters of water through an area of  $1 \text{ m}^2$  per day. Using literature values for conditions in a typical Chilean fog environment<sup>7</sup> and our new design framework, we can estimate the amount of water that can be collected using the optimal fog harvesting mesh. Typical Chilean fog conditions are characterized by a larger droplet size and higher wind velocity ( $r_{fog} \approx 13 \mu\text{m}$ ,  $v_0 \approx 6 \text{ m/s}$ ) and in such inertial conditions, the collection rate is predicted to be as large as twelve liters of water through an area of  $1 \text{ m}^2$  per day, assuming a liquid water content of  $0.7 \text{ g/m}^3$ . From such calculations it is clear that understanding the enabling roles of surface wettability in conjunction with the physical characteristics of the woven mesh geometry (*i.e.* fiber radius and shade coefficient) expands the accessible fog harvesting design space as well as future geographic opportunities for deploying fog harvesting technology.

## Appendix A Derivation of critical droplet radii $r_e$ and $r_c$

In this section, we derive two criteria for the critical radius of a droplet by equating the drag force acting on a drop to the adhesion force and secondly by equating gravitational force and pinning force based on contact angle hysteresis.

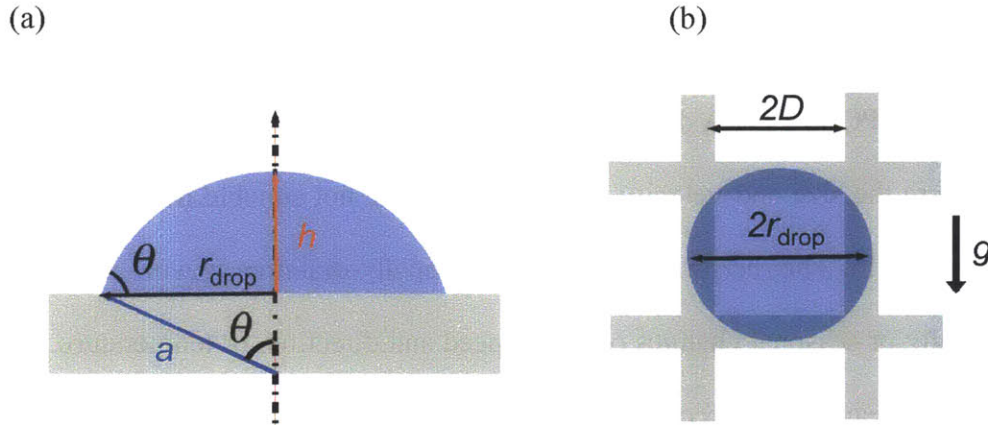


**Figure 5-6** Schematic diagram of water droplets on a cylindrical mesh filament (cross-sectional view) and on one grid element of a woven mesh (top view). Both droplets are assumed to be spherical caps with the algebraic average of contact angles  $\theta = (\theta_{adv} + \theta_{rec})/2$ .

i) The first critical droplet radius  $r_e$  for re-entrainment of droplets into the airstream is a threshold value of the liquid droplet radius at which the aerodynamic drag force ( $F_{drag}$ ) and the surface adhesion force ( $F_{adhesion}$ ) acting on a water droplet (Figure 5-6a) are balanced.

To calculate the critical droplet radius  $r_e$  we equate the drag force exerted by wind on a fog droplet and the force of adhesion on the droplet exerted by the mesh. First the drag force is obtained from the following equation,

$$F_{drag} = \frac{1}{2} \rho_{air} v_0^2 C_D A_P \quad (5-4)$$

where  $\rho_{air}$  is the density of air,  $v_0$  is the velocity of fog stream,  $C_D$  is the drag coefficient (which typically ranges from 0.4 to 4 for a bluff body such as a droplet at Reynolds numbers of  $Re \sim 10 - 10^3$ ) and  $A_p$  is the projected area normal to the direction of fog flow.

The projected area can be obtained by a simple trigonometric formula.

$$A_p = r_{drop}^2 (\theta - \sin \theta \cos \theta) / \sin^2 \theta, \quad (5-5)$$

where  $\theta$  is the algebraic average of advancing and receding contact angles  $(\theta_{adv} + \theta_{rec})/2$ .

On the other hand, the adhesion force on the liquid droplet is calculated in the following way –

$$F_{adhesion} = L_1 \gamma_{LV} (1 + \cos \theta_{rec}) \quad (5-6)$$

where  $L_1$  is the characteristic length of the droplet ( $2\pi r_{drop}$ ) and  $\gamma_{LV}$  is the surface tension of water. Finally, by equating Eq. 5-4 and Eq. 5-6 and substituting Eq. 5-5 into Eq. 5-4, the following equation for the critical radius  $r_e$  is obtained.

$$r_e = 4\pi \gamma_{LV} \sin^2 \theta (1 + \cos \theta_{rec}) / \rho_{air} v_0^2 C_D (\theta - \sin \theta \cos \theta). \quad (5-7)$$

If the droplet is not a spherical cap or the droplet radius is not significantly smaller than the radius of cylinder, these will only change the precise form of  $f(\theta)$  in Eq. 5-7, but not the fundamental scaling or magnitude of the expression  $r_e \sim (\gamma_{LV} / \rho_{air} v_0^2 C_D) f(\theta)$ . Similar expressions have been developed by Milne and Amirfazli for sheared droplets of water on airfoil surfaces.<sup>24</sup>

ii) The critical droplet radius  $r_c$  for drainage of droplets from the mesh is found by balancing gravitational force ( $F_{grav}$ ) and pinning force ( $F_{CAH}$ ) acting on a water droplet that covers a single grid of the mesh (Figure 5-6b) is calculated here. The gravitational force is expressed as –

$$F_{grav} = \rho_{water} g V \quad (5-8)$$

where  $\rho_{water}$  is the density of water,  $g$  is the constant of gravity, and  $V$  is the volume of the spherical cap shaped water droplet. Using simple trigonometric algebra, we find

$$V = \frac{\pi}{6} h (3r_{drop}^2 + h^2) \quad (5-9)$$

where  $h$  can be also expressed as  $h = r_{drop} (1 - \cos\theta) / \sin\theta$ .

To calculate the critical radius of the water droplet that causes clogging on a mesh surface, we consider the radius of a hemispherical droplet that covers a single square grid of mesh (or  $r_{drop} = D$ ). In this case, the pinning force can be expressed as

$$F_{CAH} = 2r_{drop} \gamma_{LV} (\cos\theta_{rec} - \cos\theta_{adv}) \quad (5-10)$$

If the pinning force is smaller than the gravitational force, the droplet will be drained off the mesh, leading to a fresh unoccupied mesh grid for the next fog deposition cycle. Therefore, by equating Eq. 5-8 and Eq. 5-10, we obtain the critical radius at which clogging occurs.

$$r_c = \sqrt{12\gamma_{LV} (\cos\theta_{rec} - \cos\theta_{adv}) / \pi\rho_{water} g B (3 + B^2)} \quad (5-11)$$

where  $B = (1 - \cos\theta) / \sin\theta$ .

Once again, if the droplet is not a hemispherical cap this will change the precise form of Eq. 5-11 but not the fundamental scaling  $r_c \sim \sqrt{\gamma_{LV} / \rho_{water} g} \sqrt{CAH}$ , where  $CAH = \cos\theta_{rec} - \cos\theta_{adv}$ .

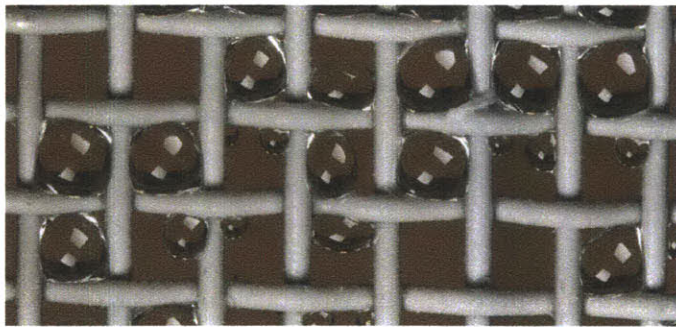


**Figure 5-7** An image of the clogging droplets on a woven mesh.



**Table 5-1** The values of the receding contact angle, contact angle hysteresis, and critical radii  $r_e$  and  $r_c$  for each surface coating, with the laboratory fog condition used in the humidity chamber experiment ( $v_0 \approx 2$  m/s) and a representative value of  $C_D = 0.7$ . For this airstream velocity, all four of the coatings show  $r_c \ll r_e$ . As a result of the large values of  $\theta_{rec}$  (which lead to easy drop roll-off and low adhesion forces), the POSS-PEMA spraycoating (denoted PPS) shows a smaller value of  $r_e$  than the half spacing  $D$  of most of the woven meshes used in the fog collection experiments, which explains the low collection efficiency value we measure experimentally (because of re-entrainment of deposited water droplets back into the convected air stream). The liquid-impregnated surfaces initially exhibit a critical droplet drainage radius ( $r_c$ ) that is similar to the POSS-PEMA dipcoating (denoted PPD), but after a short period of operation this ultimately transitions to a value that is greater than the critical radius of the original polyolefin material (denoted PO). The reason for the increased value of  $r_c$  for the liquid-impregnated coating is described in the next section.

	Polyolefin (PO)	POSS-PEMA dipcoating (PPD)	POSS-PEMA spraycoating (PPS)	Liquid-impregnated coating (KO)
$\theta_{rec}$ (°)	85	117	159	100 → 77
$CAH = \cos\theta_{rec} - \cos\theta_{adv}$	0.396	0.061	0.006	0.034 → 0.632
$r_e$ (mm)	29	7.9	0.041	20 → 29
$r_c$ (mm)	1.5	0.41	0.030	0.42 → 2

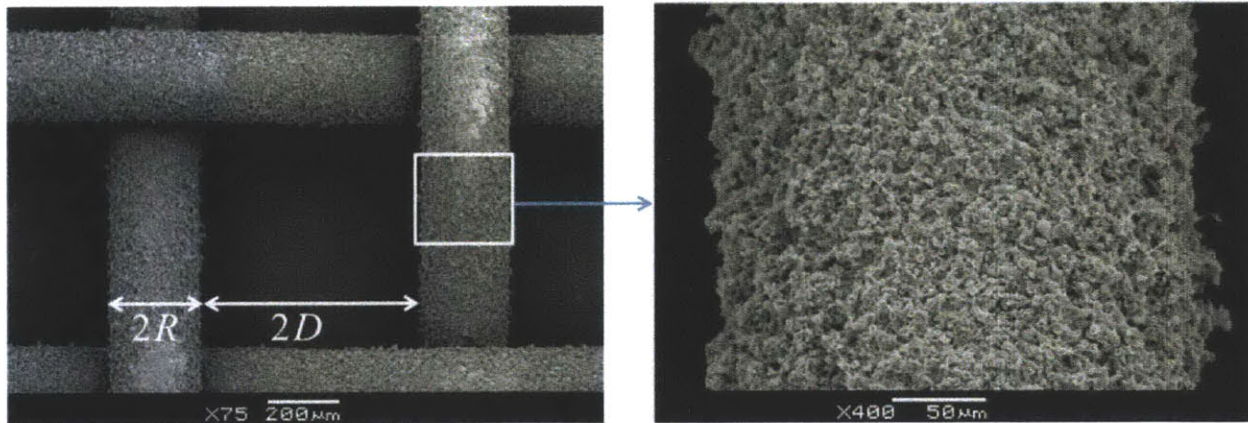


**Figure 5-8** A micrograph of the POSS-PEMA spraycoated mesh.<sup>24</sup>

## Appendix B Time evolution of the performance of liquid-impregnated textured surfaces and schematic diagram of experimental setup for fog collection efficiency measurement

Experimental details of the preparation of these surfaces are described in the Methods section. Repeated interaction with successive water droplets impacting and sliding along the liquid-impregnated textured mesh surface (denoted by the label KO in Figure 5-4, 5b) results in a progressive loss of the nonvolatile low surface tension liquid that is impregnated into the microstructure, as shown in Figure 5-9. This leads to a steady increase in the contact angle hysteresis (*CAH*) over a period of 5 mins and the mesh openings of the KO-impregnated mesh subsequently start to clog.

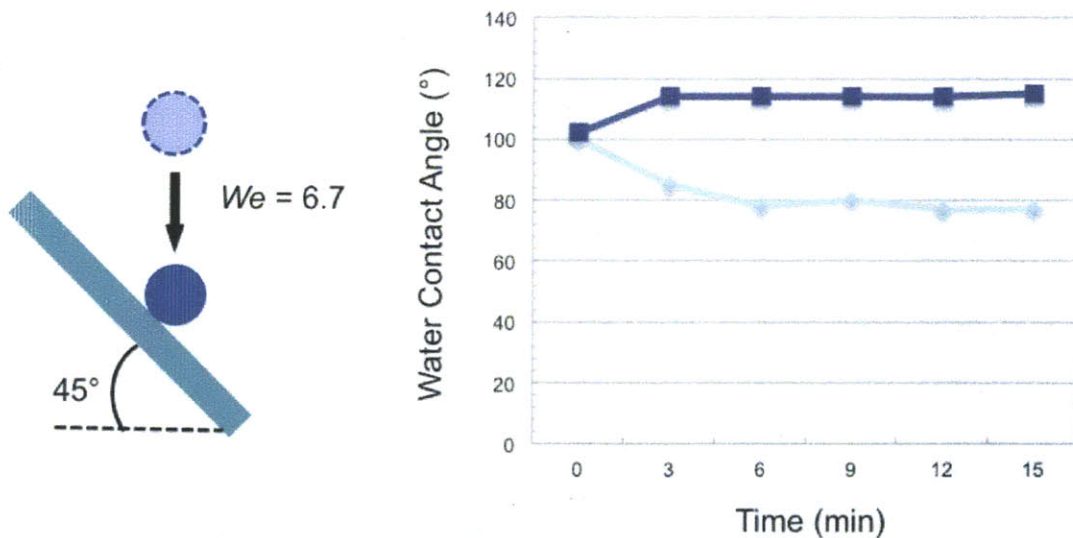


**Figure 5-9** Evolution of the advancing (dark blue) and receding (light blue) contact angles of water droplets on the liquid-impregnated surfaces. The contact angles were measured every three minutes while water droplets were released from a height of 10 mm (corresponding to impact velocity  $v \approx 0.44$  m/s;  $We = 6.7$ ) from the inclined surfaces ( $45^\circ$ ) with the flow rate of  $3.3$  mL/min (corresponding to 70 impacts per minute).

Figure 5-10 shows the experimental test configuration for all fog collection experiments. The apparatus is composed of a controlled-humidity glove box that serves as the environmental

test chamber (Electro-Tech Systems, Inc.), two concentric plastic cylinders with diameters of 100 mm and 30 mm, respectively, a nebulizer (Omron Compair XLT Nebulizer Compressor Kit NE-C25) and a variable speed fan (Thermaltake Mobile Fan II External USB Cooling Fan). See 5.2 Materials and Methods section for detailed alignment of components and measurement procedure.

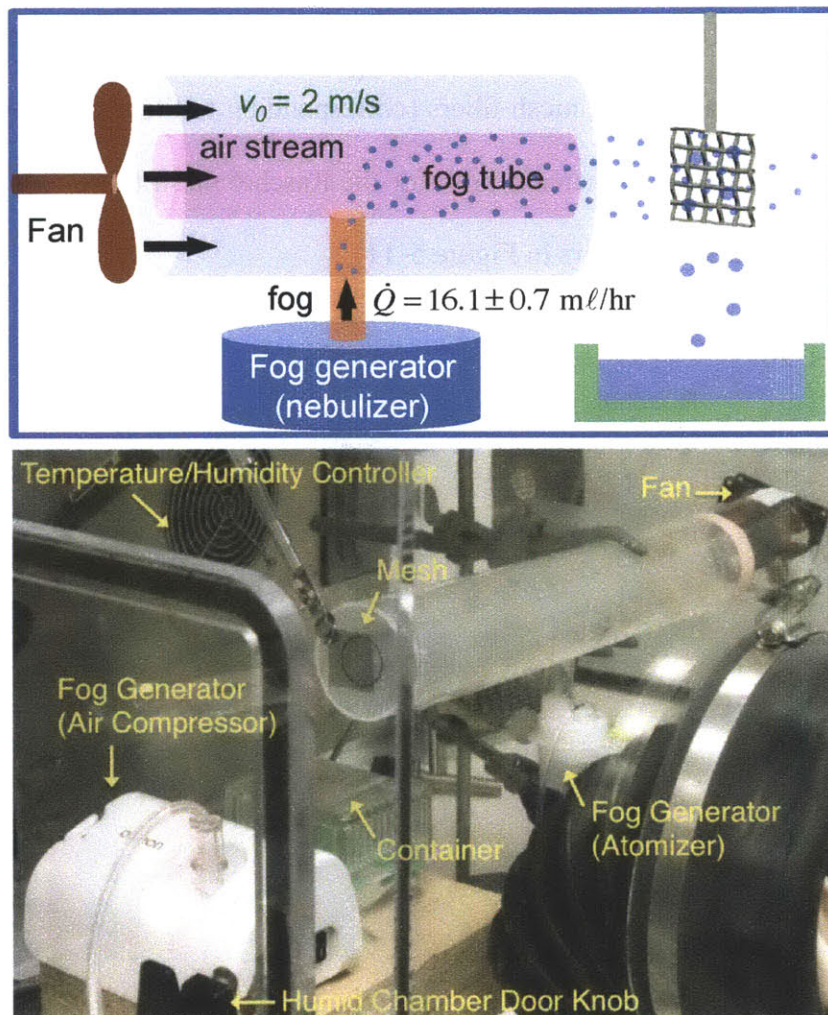


**Figure 5-10** Illustration and actual image of the experimental setup for fog collection efficiency measurement.

## Appendix C Comparison of theoretical fog collection efficiencies for mesh surfaces

The relative merits of this new design framework can be clarified by comparing the theoretical fog harvesting efficiencies of the Raschel mesh with the optimally-chosen woven mesh under a wide range of wind velocities and droplet radii, as plotted in Figure 5-11. As the wind velocity and droplet size increase from condition 1 to condition 6, the fog droplets become increasingly dominated by inertial impact on the mesh fibers (corresponding to Stokes numbers,  $St \gg 1$ ) and theoretical collection efficiencies increase both for the Raschel mesh (blue bars in Figure 5-11) and for the woven wire mesh (red bars in Figure 5-11).

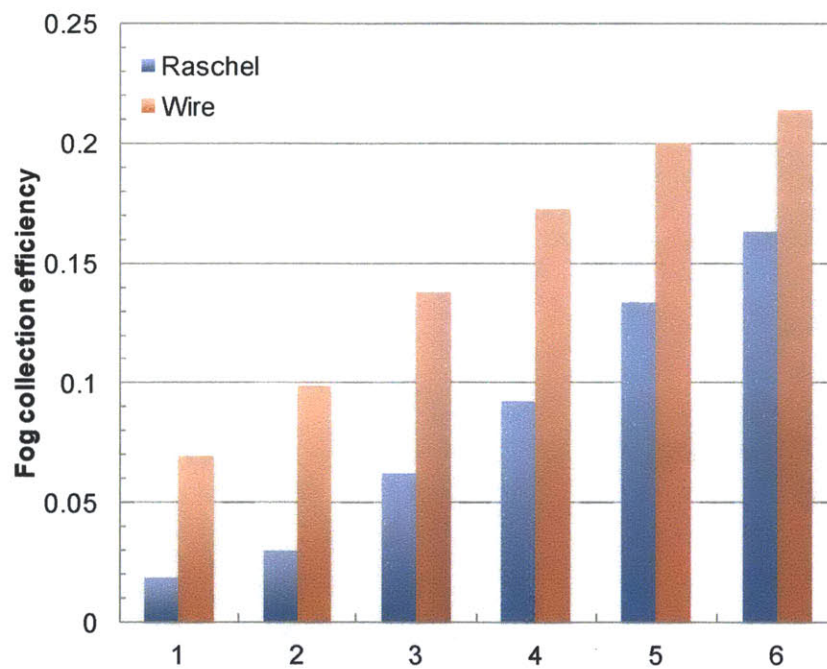


**Figure 5-11** Predicted fog harvesting efficiency  $\eta$  for a double layered Raschel mesh (blue) and for a woven mesh with  $R = 172 \mu\text{m}$ , and  $D^* = 3.5$  (red) are compared for six conditions of fog droplet size and wind velocity. Velocities ( $v_0$ ) in m/s and fog droplet radius ( $r_{\text{fog}}$ ) in  $\mu\text{m}$  are: (1)  $v_0 = 0.5$ ,  $r_{\text{fog}} = 3$ , (2)  $v_0 = 0.5$ ,  $r_{\text{fog}} = 6$ , (3)  $v_0 = 2$ ,  $r_{\text{fog}} = 3$ , (4)  $v_0 = 2$ ,  $r_{\text{fog}} = 6$ , (5)  $v_0 = 8$ ,  $r_{\text{fog}} = 3$ , and (6)  $v_0 = 8$ ,  $r_{\text{fog}} = 6$ , respectively.

Under all six fog conditions considered, the woven mesh is expected to perform significantly better than the Raschel mesh. However, the main advantage of the framework is evident under standing fog conditions and low wind speeds ( $v_0 \rightarrow 0$ ), *i.e.* conditions 1 and 2. The fog harvesting efficiency for the POSS-PEMA dipcoated woven mesh is more robust to changes in fog conditions; it does not deteriorate to the same extent as the Raschel mesh when the wind velocity decreases. As a result of this analysis, we believe that fog-harvesting technology based on appropriately chosen and coated woven meshes could be deployed in wider geographic regions of the world and also utilized over a longer portion of the year in many foggy regions.

## References

1. Food and Agricultural Organization for the United Nations, United Nations Convention to Combat Desertification, Mountain Partnership Secretariat, Swiss Agency for Development and Cooperation, and Centre for Development and Environment. Highlands and drylands - mountains a source of resilience in arid regions, **2011**, Rome.
2. United Nations Educational Scientific and Cultural Organization The United Nations World Water Development Report 4: Managing Water under Uncertainty and Risk, **2012**, Paris.
3. Klemm, O. et al. Fog as a fresh-water source: Overview and perspectives. *Ambio* **2012**, *41*, 221-234.
4. Rivera, J. D. D. Aerodynamic collection efficiency of fog water collectors. *Atmos. Res.* **2011**, *102*, 335-342.
5. Cereceda, P.; Larrain, H.; Osses, P.; Faras, M., Egana, I. The spatial and temporal variability of fog and its relation to fog oases in the Atacama Desert, Chile. *Atmos. Res.* **2008**, *87*, 312-323.
6. Schemenauer, R. S.; Cereceda, P. A proposed standard fog collector for use in high-elevation regions. *J. Appl. Meteorol.* **1994**, *33*, 1313-1322.
7. Schemenauer, R. S.; Joe, P. I. (1989) The collection efficiency of a massive fog collector. *Atmos. Res.* **1989**, *24*, 53-69.
8. Lekouch, I., et al. Dew, fog, and rain as supplementary sources of water in south-western Morocco. *Energy* **2011**, *36*, 2257-2265.
9. Hamilton, W. J.; Seely, M. K. (1976) Fog basking by the Namib desert beetle, *Onymacris unguicularis*. *Nature* **1976**, *262*, 284-285.
10. Parker, A. R.; Lawrence, C. R. Water capture by a desert beetle. *Nature* **2001**, *414*, 33-34.
11. Dawson, T. E. Fog in the California redwood forest: Ecosystem inputs and use by plants. *Oecologia* **1998**, *117*, 476-485.
12. Limm, E. B.; Simonin, K. A.; Bothman, A. G.; Dawson, T. E. Foliar water uptake: A common water acquisition strategy for plants of the redwood forest. *Oecologia* **2009**, *161*, 449-459.
13. Vasey, M. C.; Loik, M. E.; Parker, V. T. (2012) Influence of summer marine fog and low cloud stratus on water relations of evergreen woody shrubs (Arctostaphylos: Ericaceae) in the chparral of central California. *Oecologia* **2012**, *170*, 325-337.

14. Andrews, H. G.; Eccles, E. A.; Schofield, W. C. E.; Badyal, J. P. S. Three-dimensional hierarchical structures for fog harvesting. *Langmuir* **2011**, *27*, 3798-3802.
15. Zhai, L. et al. Patterned superhydrophobic surfaces: Toward a synthetic mimic of the Namib Desert beetle. *Nano Lett.* **2006**, *6*, 1213-1217.
16. Roth-Nebelsick, A. et al. Leaf surface structures enable the endemic Namib desert grass *Stipagrostis sabulicola* to irrigate itself with fog water. *J. R. Soc., Interface* **2012**, *9*, 1965-1974.
17. Sahni, V.; Blackledge, T. A.; Dhinojwala, A. Viscoelastic solids explain spider web stickiness. *Nat. Commun.* **2010**, *1*:19 doi: 10.1038/ncomms1019.
18. Sahni, V.; Harris, J.; Blackledge, T. A.; Dhinojwala, A. Cobweb-weaving spiders produce different attachment discs for locomotion and prey capture. *Nat. Commun.* **2012**, *3*:1106 doi:10.1038/ncomms2099.
19. Zheng, Y. et al. Directional water collection on wetted spider silk. *Nature* **2010**, *463*, 640-643.
20. Garrod, R. P. et al. Mimicking a *Stenocara* beetle's back for microcondensation using plasmachemical patterned superhydrophobic-superhydrophilic surfaces. *Langmuir* **2007**, *23*, 689-693.
21. Yu, T. S.; Park, J.; Lim, H.; Breuer, K. S. Fog deposition and accumulation on smooth and textured hydrophobic surfaces. *Langmuir* **2012**, *28*, 12771-12778.
22. Dorrer, C.; Ruhe, J. Mimicking the *Stenocara* beetle - dewetting of drops from a patterned superhydrophobic surface. *Langmuir* **2008**, *24*, 6154-6158.
23. Meuler, A. J. et al. Examination of wettability and surface energy in fluorodecyl POSS/polymer blends. *Soft Matter* **2011**, *7*, 10122-10134.
24. Srinivasan, S.; Chhatre, S. S.; Mabry, J. M.; Cohen, R. E.; McKinley, G. H. Solution spraying of poly(methyl methacrylate) blends to fabricate microtextured, superoleophobic surfaces. *Polymer* **2011**, *52*, 3209-3218.
25. Quere, D. Non-sticking drops. *Rep. Prog. Phys.* **2005**, *68*, 2495-2532.
26. Wong, T. -S. et al. Bioinspired self-repairing slippery surfaces with pressure-stable omniphobicity. *Nature* **2011**, *477*, 443-447.
27. Smith, J. D. et al. Droplet mobility on lubricant-impregnated surfaces. *Soft Matter* **2013**, *9*, 1772-1780.

28. Langmuir, I.; Blodgett, K. B. A mathematical investigation of water droplet trajectories. Collected works of Irving Langmuir **2004** (Pergamon Press, Oxford).
29. Milne, A. J. B.; Amirfazli, A. (2009) Drop shedding by shear flow for hydrophilic to superhydrophobic surfaces. *Langmuir* **2009**, *25*, 14155-14164.
30. Ledesma-Aguilar, R.; Nistal, R.; Hernández-Machado, A.; Pagonabarraga, I. Controlled drop emission by wetting properties in driven liquid filaments. *Nat. Mater.* **2011**, *10*, 367-371.
31. Quèrè, D. Wetting and roughness. *Annu. Rev. Mater. Res.* **2008**, *38*, 71-99.



# **CHAPTER 6**

## **6. Thesis Summary and Future Work**

## 6.1 Thesis Summary

In this thesis, the fundamental hydrodynamics of droplets on textured surfaces was studied for designing optimal engineered surfaces for various applications including superhydrophobic and superphotophilic surfaces for photovoltaic cells, easy-cleaning printer heads, and fog harvesting permeable structures. We started from super-wetting or super-repellency of slender tapered nanostructures that were selected based on a joint consideration of the design consideration governing extreme wetting properties and high optical transparency together with broadband omnidirectional anti-reflectivity. Inspired by the conical structure of naturally-occurring superhydrophilic or superhydrophobic plant leaves and moth eyes, square arrays of subwavelength slender tapered conical structure were fabricated utilizing the novel fabrication methods described in Chapter 2. With a vapor phase hydrophobic chemical layer coating on the nanocone structure, we could achieve robust superhydrophobicity that can resist both high static Laplace pressure by micrometric water droplets and high dynamic pressure generated by water hammer pressure at the moment of water droplet impact on the textured surface. The fabricated silica nanostructure was also optimized to suppress the reflection of a broad range of incident wavelengths, as well as to maximize the range of incident angles. In addition, we showed both self-cleaning properties of the hydrophobic nanocone structure against three different natural and artificial contaminants and antifogging properties of hydrophilic nanocone structures by measuring time-varying optical transmission through the silica textured surface.

In the next chapter, we delved into the repellency of textured surfaces for oils that possess lower surface tension than water. To investigate the oil-repellency or superoleophobicity of these

surfaces, we fabricated pillar structures with wavy sidewalls to create a re-entrant structure (*i.e.*, a ‘scalped’ topography that bends back to itself). The effect of different re-entrant texture designs on static and dynamic wetting of water and hexadecane droplets was studied. The critical pressure difference across the liquid-air interface for droplets sitting on the re-entrant structures that characterize the resistance of superoleophobic state against external perturbation was discussed with careful consideration of the mechanical durability of nanometer scale slender structures as well. By changing geometrical parameters such as diameter, spacing, period, and height of the cylindrical pillars, we could examine the effect of texturing on the apparent contact angles, advancing and receding contact angles, and sliding or roll-off angles. By extending the discussion of the robustness of the Cassie-Baxter state of low surface tension liquids on textured superoleophobic surfaces, we also explored the mechanical durability and proposed two dimensionless numbers as design parameters for evaluating the mechanical robustness of cylindrical nanopillars.

Because of the robustness of the Cassie-Baxter state for water droplets on natural superhydrophobic leaves, impacting aqueous droplets result in complete drop rebound on liquid-repellent leaves. This can lead to loss of significant amount of sprayed herbicides and pesticides. To circumvent this problem, dilute polymer solutions are widely used to suppress the rebound of impacting aqueous droplets. In Chapter 4, we investigated how to control the drop impact dynamics on superhydrophobic surfaces by studying the physico-chemical hydrodynamics of dilute polyethylene oxide aqueous solutions. Previous studies on the drop impact dynamics of water and dilute PEO solution on flat hydrophobic surfaces that result in drop rebound or deposition were first analyzed. We could identify different drop impact dynamics that can be used to control drop deposition rate, by systematically changing not only the physico-chemical

properties of PEO solutions but also the textural characteristics of hydrophobic textured surfaces. As the length scale of asperities becomes smaller (or the number density of features increases), hydrophobic textured surfaces maintain greater resistance to the high dynamic pressure resulting from drop impact. Furthermore, we also focused on the additional energy dissipation that is observed in the viscoelastic dilute PEO solutions when compared to pure water as a result of the stretch and relaxation of polymer coils near the retracting contact line. We could construct a drop impact dynamics state diagram (Figure 4-4) describing the observed behavior for impacting droplets of non-Newtonian fluids in terms of two important dimensionless numbers that characterize the robustness of the Cassie-Baxter state and the level of energy dissipation by polymer coil stretch and relaxation, as a result of interaction with the texture at the retracting liquid-air-solid composite contact line.

As another surface design problem that an understanding of drop impact dynamics can be applied to, we investigated collection of airborne fog droplets on permeable fibrous structures like woven meshes. We analyzed the known aerodynamic and deposition components of theoretical collection efficiency and constructed a contour map based on the two dimensionless geometry parameters that characterize 1) radii of cylinder of a given woven mesh relative to radius of fog droplet and 2) geometrical permeability. Utilizing a simple experimental setup that can control the humidity and temperature of surrounding environment and that can fix flow rate and average droplet size of fog stream, we emulated a natural convected stream of fog droplets and evaluated the performance of a family of woven mesh surfaces as well as conventional polyolefin Raschel meshes. We could quantitatively analyze the two major problems that significantly reduce the actual fog collection efficiency, by using appropriate force balance to calculate critical radii of deposited water droplets. The analysis of wetting characteristics of

various surface coatings enabled us to find an optimal mesh design, resulting in a five-fold increased actual collection efficiency compared to the conventional Raschel mesh that is presently deployed. A dimensionless contour map (Figure 5-5) provided a framework for designing optimal liquid collecting permeable surfaces in terms of both geometry and surface coating, for a given droplet size and free stream condition.

In summary, to realize optimal textured surfaces with each of the functionalities described in the previous chapters, we have developed novel fabrication methods and have constructed design frameworks that can be used for different design requirements or operating conditions. Our future plans for commercializing some of the functional surfaces in this work and another type of multifunctional surfaces are briefly introduced in the next section.

## 6.2 Future Work

### 6.2.1 Inverted Nanocone Structure for Enhanced Mechanical Durability and Low Cost Fabrication of Multi-functional surfaces

To enhance mechanical strength of multifunctional nanostructure and develop lower cost fabrication methods compared to our previous nanocone work,<sup>1</sup> we propose a new design of nanostructures for anti reflectivity, superhydrophilicity or superhydrophobicity, consisting of perfectly periodic tapered nanohole arrays. This nanostructured surface is essentially the inverse of those discussed in Chapter 2 that can exhibit structural superhydrophilicity or, in combination with a suitable chemical coating, robust superhydrophobicity.<sup>2,3</sup> Enhanced optical transmission compared to flat unstructured silica surfaces and extremely low reflectance also can be achieved

over a broad range of bandwidth due to the gradually varying index of refraction from the tapered feature of this nanotextured geometry.<sup>4</sup>

Enhanced mechanical strength is one of advantages of the proposed inverted nanocone structures. Whereas the aspect ratio of nanocone structure shows a tradeoff between the designed functionalities and mechanical robustness, the inverted nanocone structure can enhance its functionalities by increasing its aspect ratio without negatively affecting the mechanical strength of the nanostructures.<sup>5</sup> The mechanical strength of the proposed inverted nanocone structures will be examined and compared with that of nanostructures using finite element method (FEM). Assuming that the nanotextured surface is touched by a finger with a strong shearing force, the stress can be easily concentrated at the tip of the nanocone structure, whereas the stress of the inverted nanocone array is distributed over the top surface area. As a result, the maximum stress in the nanocone is much larger than that of the inverted nanocone structure, which might cause yield or fracture of the nanocone tip, leading to degradation of its functional performance.<sup>1,5</sup> Also it is clear that the inverted nanocone structures are free from bucking or collapse problems since the inverted nanocone array does not exhibit localized deflection: each structural element is connected to and supported by adjacent structures, similar to a honeycomb structure.<sup>5</sup>

We will use simple and cost-effective mass replication techniques,<sup>6,7</sup> which are suitable for mass manufacturing of the multifunctional surface for portable devices such as displays of mobile phones, tablet computers and portable cameras. In order to start the replication process, a negative mold consisting of high aspect ratio conical structures can be used so that repeated replication at a mass scale by stamping or injection molding into inverted nanocone structures on ultraviolet (UV)-curable polymer material can be performed. After curing the polymer with UV light, the mold has to be cautiously detached from the polymer surface. In the imprint steps, an

anti-adhesion hydrophobic chemical layer will be coated on the mold surface to prevent sticking problem between the mold and polymer layers. Also in order to fill the nanostructures with the polymer during the contacting step, vacuum assisted filling will be used when the mold is pressed into the liquid polymer.

### 6.2.2 Initial Steps for Commercializing Fog Harvesting Surfaces in Chile

The mountainous coastline and a semi-arid climate make the coastal regions in the north of Chile an ideal testing site for the large-scale deployment of fog harvesting devices. In this region water collection from fog harvesting offers a huge untapped potential to locally satisfy the need for a pure and dependable supply of water.<sup>8-11</sup> As initial steps toward commercializing fog harvesting surfaces developed in this thesis, we have started collaboration to apply our fundamental engineering knowledge regarding surface coating technologies and the physico-chemical control of wettability with the Chilean team's (led by Prof. Juan de Dios Rivera, Prof. Pilar Cereceda and other colleagues from PUC, Chile) deep and interdisciplinary understanding of the design of fog harvesting systems.<sup>12-14</sup> Due to their strategic location and previous experience in this area to deploy large area fog harvesting meshes in Chile, Prof. Rivera's team in Chile represent an ideal collaborator in this endeavor.

The present technology for collecting fog water using commercially-available mesh surfaces utilizes a simple structural design and inexpensive local materials, and it is affordable to poor local communities.<sup>8, 12</sup> Our coating technology can be adapted to be used on existing structural installations or in entirely new aerodynamically-optimized designs. We plan on

pursuing both avenues of research in conjunction with our PUC partners. Currently, the mechanical durability of the coated mesh structures has been being tested and we believe that a pilot-scale deployment and monitoring of fog collection systems in Chile will provide valuable feedback to iterate new designs and coating materials.

We would like to also extend the collaboration by deploying large area meshes of different nanostructured coatings and monitoring their performance in the future. We believe that an optimized fog-harvesting mesh would act as a cornerstone for commercialization of the fog harvesting technology in Chile. Further, working with our Chilean partners we would like to engineer a whole system for water collection, purification, and distribution. A parallel effort to create awareness about this technology in the local community will help to create enthusiasm and demand for fog water. Collaboration with local universities with established presence in the region (PUC Santiago and Univ. de los Andes) will help to gain credibility for the venture. Large-scale deployment of such a technology will create employment opportunities for unskilled labor to install and maintain such devices.

### 6.2.3 Dactyloporous Surfaces

Using fingers to handle objects is one of the unique characteristics of human behaviors. In daily life, we use the fingers of our hands to use spoons, forks, cups, pens, to open books, newspapers, to type on computer keyboards, and to control the touch screen of electronic devices. When fingers contact with these surfaces, submillimetric ridges on the epidermis leave a unique pattern referred to generally as a ‘fingerprint’, made of secreted human sweat or sebum, on the contacting surfaces. These fingerprint films are usually unwanted and we seek to remove



these oily films from transparent surfaces such as windows, glasses, goggles, touch screens and displays of electronic devices. Because the micrometric pattern of fingerprint films usually scatters light and results in blurry letters or images behind the optically transparent and distortion free smooth surfaces.

There have been numerous studies on how to prevent the creation of fingerprint film or how to conveniently remove fingerprint oil from surfaces. Two methods have been highlighted for the past decade. The first one is to inhibit the creation of fingerprint films on the surfaces by making sweat- or sebum-repellent surfaces (*i.e.* superoleophobic or omniphobic surfaces) using the combination of low surface energy chemical coating and special textured structures. However, the liquid-solid-air composite state that enables such super-repellency is thermodynamically metastable. Beyond a critical external perturbation pressure (which creates a pressure difference across the liquid-air interface higher than impalement pressure<sup>15-17</sup>), the metastable composite state transitions to a globally stable fully-wetted state and super-repellency is no longer recovered until the liquid is fully removed by wiping, washing, evaporation, etc. For a low surface tension oil such as sebum with vanishingly small vapor pressure the barrier to this metastable transition is very small. According to theoretical analysis,<sup>17</sup> the maximum pressure range of superoleophobic surfaces that can be created by nanoparticles with diameter of 100 nm is only around 30 kPa, which is barely sufficient to resist the typical human touch pressures, in consideration of order of magnitude of typical contact area ( $1 \text{ cm}^2$ ).<sup>18, 19</sup> Therefore, the intrinsic metastability and finite impalement pressure limit the use of superoleophobic or omniphobic microtextured surfaces for preventing the depositing and spreading of fingerprint films under practical conditions.

The second method exploits the photocatalytic oxidization of titanium dioxide to chemically degrade the deposited fingerprint oils. Two decades ago, Honda and Fujishima unveiled the evolutionary photocatalytic effect that can be applied to environmental science, energy science, etc.<sup>20, 21</sup> One of their discoveries is the oxidization of thin organic thin film directly contacting TiO<sub>2</sub> layer by photocatalytic effect.<sup>20</sup> Later, this oxidization of thin film was extended to the concept of self-cleaning by photocatalytic effect and has been highlighted as a way of removal of thin fingerprint film. Recently, TiO<sub>2</sub> nanoparticles (or porous structure) have been investigated as a more efficient photocatalytic structure than flat TiO<sub>2</sub> films.<sup>20, 21</sup>

However, there are few studies on antifingerprint surfaces and they are typically limited to showing microscope images of the surfaces with fingerprint films before and after exposure to light sources.<sup>22</sup> Important issues such as change of optical properties (e.g., transparency or haze) of surfaces coated by the titanium dioxide nanoparticle have not been analyzed quantitatively. Moreover, optimal design (e.g., selection of nanoparticle size and thickness of coating layer) and fabrication methods for both (i) maximizing photocatalytic effect to remove fingerprint film by UV light or equivalent amount of sunlight and (ii) minimizing scattering by the stacked nanoparticles layer have not been investigated from the viewpoint of basic interfacial phenomena and optics.

Based on the analysis, we will develop optimal designs and coating methods for TiO<sub>2</sub> nanoparticle films in which the outermost layer maximizes both (i) photocatalytic oxidation effect, leading to the removal of fingerprint oils after several hours under sunlight or equivalent UV light sources and (ii) optical transmission of the transparent coated surfaces. With suitable doping materials such as platinum and palladium, it is also possible to shift operating wavelength

to visible light (400 – 800 nm), keeping high transmission of light through the transparent surfaces.

## References

1. Park, K.-C.; Choi, H. J.; Chang, C.-H.; Cohen, R. E.; McKinley, G. H.; Barbastathis, G. Nanotextured Silica Surfaces with Robust Superhydrophobicity and Omnidirectional Broadband Supertransmissivity. *ACS Nano* **2012**, *6*, 3789-3799.
2. Lai, Y.; Lin, C.; Wang, H.; Huang, J.; Zhuang, H.; Sun, L. Superhydrophilic–Superhydrophobic Micropattern on TiO<sub>2</sub> Nanotube Films by Photocatalytic Lithography. *Electrochem. Comm.* **2008**, *10*, 387-391.
3. Ressine, A.; Finnskog, D.; Marko-Varga, G.; Laurell, T. Superhydrophobic Properties of Nanostructured– Microstructured Porous Silicon for Improved Surface-Based Bioanalysis. *Nanobiotechnol.* **2008**, *4*, 18-27.
4. Eyderman, S.; John, S.; Deinega, A. Solar Light Trapping in Slanted Conical-Pore Photonic Crystals: Beyond Statistical Ray Trapping. *J. Appl. Phys.* **2013**, *113*, 154315.
5. Gere, J. M. *Mechanics of materials*. Brooks/Cole, 2001.
6. Choi, S.-J.; Kim, H. N.; Bae, W. G.; Suh, K.-Y. Modulus- and Surface Energy-Tunable Ultraviolet-Curable Polyurethane Acrylate: Properties and Applications. *J. Mater. Chem.* **2011**, *21*, 14325-14335.
7. Kwak, M. K.; Ok, J. G.; Lee, J. Y.; Guo, L. J. Continuous Phase-Shift Lithography with a Roll-Type Mask and Application to Transparent Conductor Fabrication. *Nanotechnology* **2012**, *23*, 344008.
8. Schemenauer, R. S.; Cereceda, P. A proposed standard fog collector for use in high-elevation regions. *J. Appl. Meteorol.* **1994**, *33*, 1313-1322.
9. Schemenauer, R.S.; Cereceda, P. The Role of Wind in Rainwater Catchment and Fog Collection. *Water International* **1994**, *19*, 70-76.
10. Schemenauer, R. S.; Joe, P. I. (1989) The collection efficiency of a massive fog collector. *Atmos. Res.* **1989**, *24*, 53-69.
11. Abdul-Wahab, S. A.; Lea, V., Reviewing Fog Water Collection Worldwide and in Oman. *International Journal of Environmental Studies* **2008**, *65*, 485-498.
12. Cereceda, P.; Larrain, H.; Osses, P.; Faras, M., Egana, I. The spatial and temporal variability of fog and its relation to fog oases in the Atacama Desert, Chile. *Atmos. Res.* **2008**, *87*, 312-323.
13. Rivera, J. D. D. Aerodynamic collection efficiency of fog water collectors. *Atmos. Res.* **2011**, *102*, 335-342.
14. Klemm, O. et al. Fog as a fresh-water source: Overview and perspectives. *Ambio* **2012**, *41*,

221-234.

15. Tuteja, A.; Choi, W.; Ma, M.; Mabry, J. M.; Mazzella, S.; Rutledge, G.; McKinley, G. H.; Cohen, R. E. Designing Superoleophobic Surfaces. *Science* **2007**, *318*, 1618-1622.
16. Tuteja, A.; Choi, W.; Mabry, J. M.; McKinley, G. H.; Cohen, R. E. Robust Omniphobic Surfaces. *Proc. Natl. Acad. Sci. U. S. A.* **2008**, *105*, 18200-5.
17. Butt, H.-J.; Semprebon, C.; Papadopoulos, P.; Vollmer, D.; Brinkmann, M.; Ciccotti, M. Design Principles for Superamphiphobic Surfaces. *Soft Matter* **2013**, *9*, 418-428.
18. Mascaro, S. A.; Asada, H. H. Measurement of Finger Posture and Three-Axis Fingertip Touch Force Using Fingernail Sensors. *IEEE Trans. Robot. Autom.* **2004**, *20*, 26-35.
19. Parlitz, D.; Peschel, T.; Altenmüller, E. Assessment of Dynamic Finger Forces in Pianists: Effects of Training and Expertise. *J. Biomech.* **1998**, *31*, 1063-1067.
20. Hashimoto, K.; Irie, H.; Fujishima, A. TiO<sub>2</sub> Photocatalysis: A Historical Overview and Future Prospects. *Jpn. J. Appl. Phys.* **2005**, *44*, 8269-8285.
21. Kozawa, E.; Sakai, H.; Hirano, T.; Kohno, T.; Kakihara, T.; Momozawa, N.; Abe, M. Photocatalytic Activity of TiO<sub>2</sub> Particulate Films Prepared by Depositing TiO<sub>2</sub> Particles with Various Sizes. *J. Microencap.* **2001**, *18*, 29-40.
22. Mori, K. Photo-Functionalized Materials Using Nanoparticles: Photocatalysis. *KONA* **2005**, *23*, 205-214.